Neotectonic and Paleoseismic Onshore-Offshore integrated study of the Carboneras Fault (Eastern Betics, SE Iberia)

Estudio integrado tierra-mar de la Neotectonica y Paleosismología de la Falla de Carboneras (Béticas Orientales, SE Península Ibérica)

Ximena Moreno Mota

RISKNAT
Departament de Geodinàmica i Geofísica
Universitat de Barcelona

Barcelona Center for Subsurface Imaging
Unidad de tecnología Marina
Consejo Superior de Investigaciones Científicas

Neotectonic and Paleoseismic Onshore-Offshore integrated study of the Carboneras Fault (Eastern Betics, SE Iberia)

Estudio integrado tierra-mar de la Neotectonica y Paleosismología de la Falla de Carboneras (Béticas Orientales, SE Península Ibérica)

Memoria presentada por

Ximena Moreno Mota

para optar al grado de Doctora en Geología

Esta memoria se ha realizado dentro del programa de Ciències de la Terra (bienio 2005-2006) de la Universitat de Barcelona bajo la dirección de las Doctoras Eulàlia Masana Closa y Eulàlia Gràcia Mont

Barcelona, Julio de 2010

Part III: The Carboneras Fault offshore

Chapter 6: Seismostratigraphic and neotectonic analysis of the Carboneras Fault offshore

6.1. Introduction

The offshore portion of the Carboneras Fault Zone (CFZ) strikes N045°–N060° and extends for 90 km from the shoreline at Salinas de Cabo de Gata (Fig. 2.3), traversing the slope of the Almería Margin. To study the neotectonics, the paleoseismology and the depth architecture of the CFZ, a multidisciplinary analysis of the submerged part of the fault was carried out during various marine surveys (IMPULS-2006, EVENT-SHELF-2008, EVENT-DEEP-2010), based on swath-bathymetry data, seismic reflection profiling, and the sampling, analysis and dating of marine sediments (see Chapter 3).

The nature of the earthquake hazard along the CFZ has typically been underestimated because the use of high-penetration but low-resolution geophysics (e.g., multi-channel seismic profiles), combined with a lack of reported seismicity in the area, has meant that slowly and moderately moving faults have been erroneously interpreted to be inactive (Bucci et al., 2009). Given that other lines of evidence (e.g., geomorphology) indicate recent seismic activity, higher-resolution data are required to obtain a more realistic understanding of the relevant structures in the area.

High-resolution seismic data can help in identifying slowly to moderately moving active faults, in obtaining their seismic parameters, and in relating faulted horizons to historical earthquakes and those recorded by seismographs. High-resolution seismic reflection profiles (depth penetration of <3 km and vertical resolution of 2.5 m) enable an analysis of the tectonic setting and the pattern of faulting. Very high-resolution seismic data (depth penetration of <100 m and vertical resolution of 15 cm) are necessary to image the uppermost portions of faults, seafloor surface ruptures and the interactions of faults with recent sediments, which would constrain the timing and nature of the most recent fault movements.

This study considers data obtained by four different seismic systems during three cruises in the area of the CFZ (Fig. 6.1). The IMPULS survey (2006) was devoted to imaging the Carboneras Fault using high-resolution multi-channel seismics (HR-MCS) and parametric echo-sounder (TOPAS); most of the survey lines analysed in this thesis were collected during this survey (black and green lines in Fig. 6.1, respectively). The present analysis also considers very high-resolution single-channel Sparker lines of the EVENT-SHELF survey (2008) (blue lines in Fig. 6.1), which cross the fault in the shelf area, thereby extending the imagery of the fault to shallow water depths where the deeper-penetration systems were unable to clearly

image the subsurface architecture due to multiple reflections. Finally, one deep-penetration MCS line (DP-MCS) from the EVENT-DEEP cruise (2010) (yellow line in Fig. 6.1, line EVE2b) was acquired to assess the crustal architecture of the fault, although the processing of these data was incomplete at the time of writing this thesis; consequently, this line is not discussed here.

Sixty parasound (TOPAS), 5 Sparker and 47 HR-MCS profiles (Fig. 6.1) provide a nearly three-dimensional view of the architecture of a 100-km-long section of the offshore CFZ and surrounding structures. These data, together with high-resolution bathymetric data, provide a detailed picture of the morphostructure of the Almería Margin. All of the HR-MCS and Sparker profiles presented in this chapter can be found, in uninterpreted form, in the Annex of this thesis.

Figure 6.1. (next page) Seismic profiles across the Carboneras Fault and surrounding structures acquired during the IMPULS, EVENT-SHELF and EVENT-DEEP cruises.

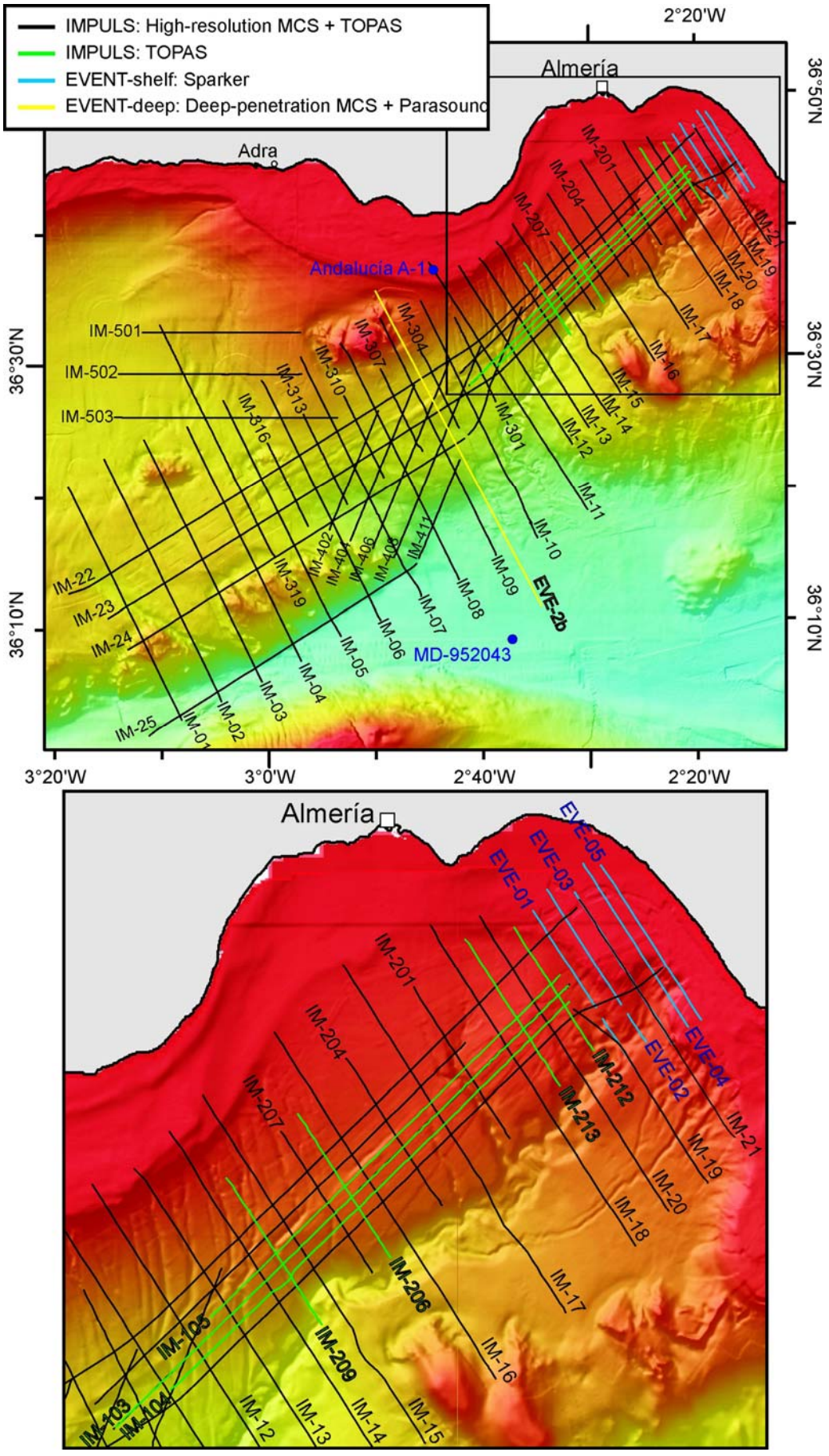
IMPULS: High-resolution MCS + TOPAS
IMPULS: TOPAS
EVENT-shelf: Sparker
EVENT-deep: Deep-penetration MCS + Parasound
2°20'W
Almería
36°50'N
Adra
Andalucía A-1
IM-501
IM-502
IM-503
36°30'N
36°10'N
MD-952043
EVE-2b
3°20'W
3°0'W
2°40'W
2°20'W
EVE-01
EVE-03
EVE-05
EVE-04
EVE-02
IM-212
IM-213
IM-206
IM-209
IM-105
IM-103
IM-104

6.2. Physiography of the Almería Margin

The present study area is located offshore at the Almería Margin, within the northeast Alboran Basin, and extends east–west from Gata Cape (2°20′W) to the Adra margin (3°20′W), and north–south from north of the Alboran Ridge (36°10′N) to the Almería coast (36°60′N) (Fig. 6.2).

Physiographically, the Almería Margin is divided into the shelf, the slope and the base of the slope (Alonso and Maldonado, 1992; Muñoz et al., 2008; Lo Iacono et al., 2008) (Fig. 6.2). The Almería shelf is narrow (4–12 km wide) and reaches depths of 120–180 m (Sanz et al., 2003). The shelf has a generally smooth morphology and is characterised by a gradient of less than 1°. The shelf-edge is characterised by a moderate gradient of 3° at depths of 120–130 m to the west of the study area and 140–180 m to the east (Lo Iacono et al., 2008). At the slope, the topographic gradient shows an abrupt increase to 5.5°. This is the predominant domain at the margin, extending seaward for 40 km until encountering the base of the slope at a depth of around 1400 m. At the base of the slope, to the south of the study area, the Eastern Alboran Basin exceeds 2000 m in depth and is connected to the Western Alboran Basin via the Alboran Channel.

The Almería Margin is characterised by a turbiditic system and several topographic highs (Fig. 6.2). The area contains mass transport deposits and scarps, as well as geological structures such as the Carboneras Fault and NW–SE-trending folds. These features are described in the following sections.

6.2.1. *Morphostructural elements of the Almería Margin*

The Almería Turbidite System crosses the study area and is divided into the Almería Canyon, the Almería Channel and three tributary valley systems (Fig. 6.2 and 6.3) (Alonso and Maldonado, 1992; Estrada et al., 1997; Alonso and Ercilla, 2003; Gràcia et al., 2006; García et al., 2006). The Almería Canyon drains from the shelf edge to deep-sea fan deposits, extending for 33 km and ranging in depth from 470 m in the north to 1200 m in the south. The average gradient of the canyon is approximately 1.3°, with an abrupt decrease in gradient at a depth of 1000 m. The canyon, which cuts through slope deposits (average depth of incision, 250 m), varies in width from 1.6 km (at a depth of 550 m) to 4.8 km (at a depth of 1000 m) (Lo Iacono et al., 2008). The Almería Channel is the downstream continuation of the Almería Canyon and represents a meandering channel-levee aggradational turbidite system, extending for almost 26 km, as far as the edge of the Alboran Trough at depths from 1200 m to about 1700 m (Alonso and Ercilla, 2003). The channel follows a meandering course in a NNE–SSW direction, changing to a N–S direction at a depth of 1350 m, coincident with a 60-m topographic threshold that also marks a decrease in the channel gradient from 2.3° to 1.1° (Lo Iacono et al., 2008).

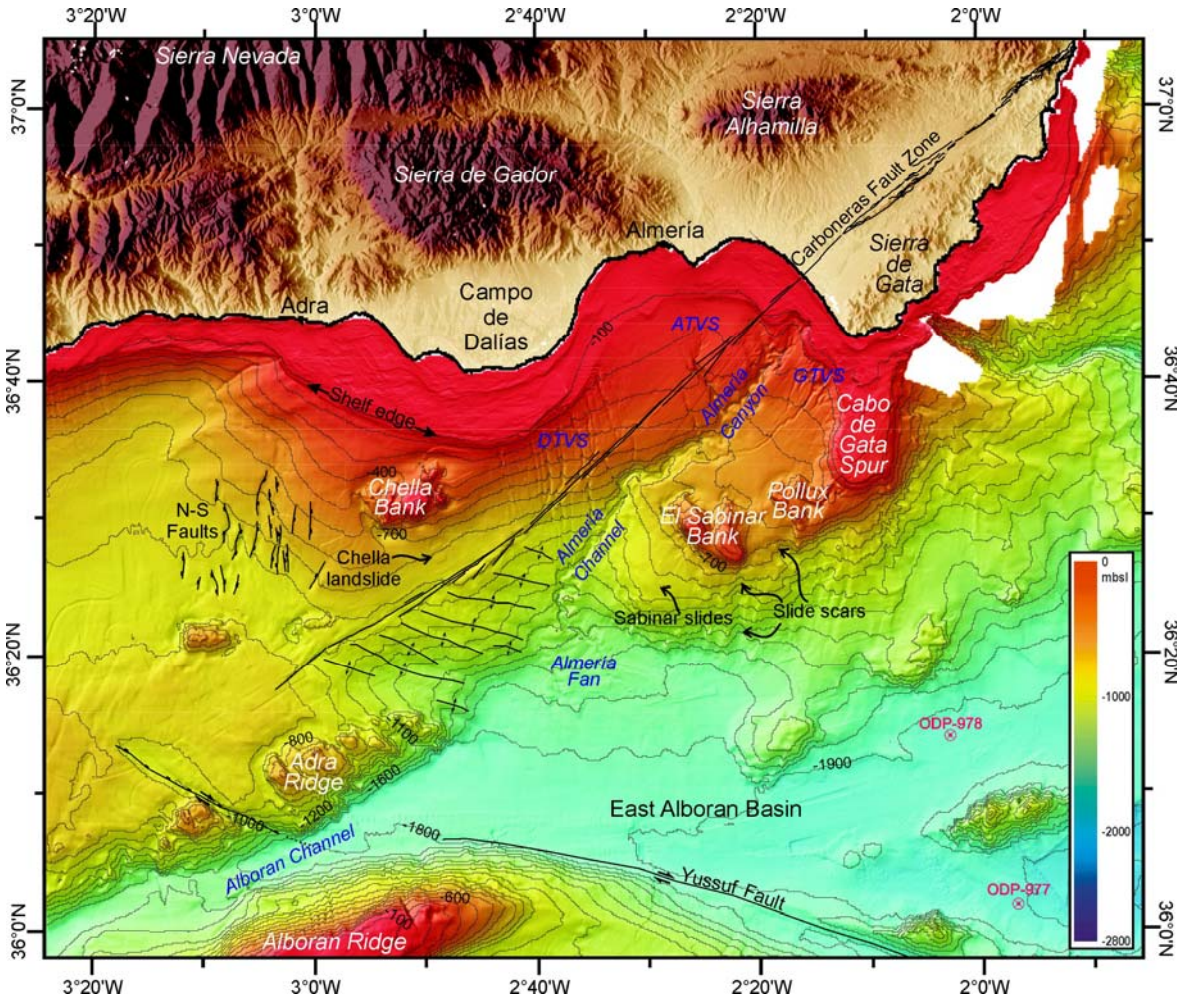

Figure 6.2. Topographic and bathymetric map of the Almería Margin and surrounding areas of the SE Iberian Peninsula and eastern Alboran Sea, showing the main morphostructural features and the locations of two Ocean Drilling Program sites in the East Alboran Basin. Contour interval is 100 m. DTVS: Dalías Tributary Valley System; ATVS: Andarax Tributary Valley System; GTVS: Gata Tributary Valley System.

The three main tributary valley systems of the Almería Canyon are the Gata tributary valley system (GTVS) to the east of the canyon, and the Andarax tributary valley system (ATVS) and Dalías tributary valley system (DTVS) to the west (Gràcia et al., 2006; García et al., 2006). The DTVS cuts the shelf-edge offshore from Campo de Dalías and trends N–S and then NW–SE to depths of 900–1200 m. This system comprises linear to sinuous valleys, recognizable as gullies and channel-levee systems. The amount of incision along the valley axes ranges from a few meters to a maximum of about 60 m. The average gradient of the valleys is initially 2°, but increases to 3° at the intersection with the Carboneras Fault (Lo Iacono et al., 2008). The various sedimentary regimes of the gully and channel-levee systems are related to late Quaternary sea-level oscillations and hyperpycnal flows associated with sediment inputs of the Andarax River (García et al., 2006). The formation of the

Almería Turbidite Systems started during the early Pliocene and was strongly affected by tectonic activity during deposition, as indicated by the orientation of the canyon (sub-parallel to the offshore Carboneras Fault) and by the presence of abrupt flanks and several breaks in slope along its pathway (Alonso and Ercilla, 2003; Gràcia et al., 2006).

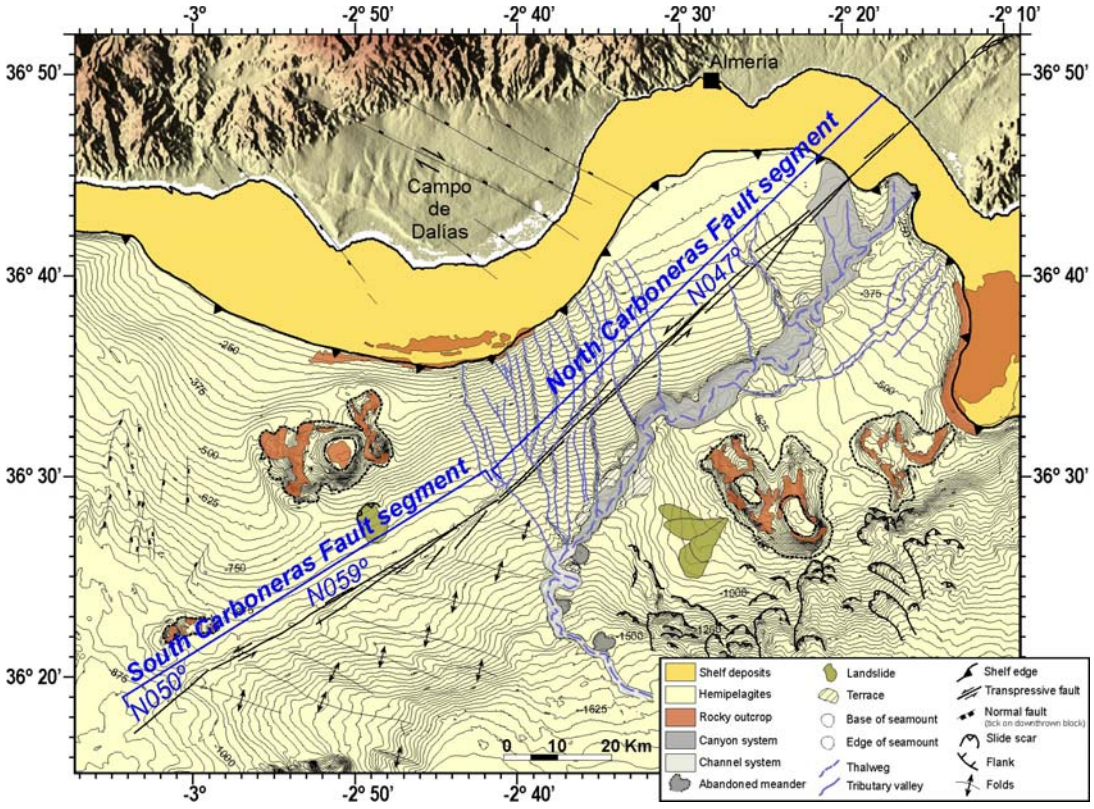

Figure 6.3. Geomorphological map of the Almería Margin based on bathymetric, seismic and sampling data. Modified from Gràcia et al. (2006) and Lo Iacono et al. (2008).

The prominent highs in the slope area are the morphological expression of middle Miocene to Pleistocene calc-alkaline K-rich volcanic rocks (Duggen et al., 2004). In addition to the Cabo de Gata Spur, three volcanic seamounts are observed in the study area: the Chella, Sabinar, and Pollux banks (Fig. 6.2). The Chella and Sabinar banks are partially surrounded by circular moats of erosional origin, probably linked to bottom-current activity (Alonso and Maldonado, 1992; Muñoz et al., 2008). The Chella Bank is located on the western sector of the slope area and comprises a circular high flanked by two NW–SE-trending ridges. The depth of the base of the bank ranges from 370 m on its northern flank to 700 m on its southern side. The 2-km-wide top of the bank ranges in depth from 100 to 200 m and is characterised by patchy mounds of carbonate coral (Lo Iacono et al., 2008).

The Sabinar Bank is located along the eastern part of the slope, 9 km from the DTVS, and comprises two main morphological highs oriented NNW–SSE and separated from each other by a narrow trough (450 m deep). The depth of the base of

the bank ranges from 600 to 700 m, and the minimum depth of the top of the bank is 280 m.

The Pollux Bank, located 6.7 km east of Sabinar Bank, is irregular and is composed of several isolated highs (depths of 240–600 m), mainly oriented NNW–SSE. This bank is smaller than the other banks and is also probably capped by mounds of carbonate coral (Lo Iacono et al., 2008). Slope failures are evident to the south of the Chella Bank and along the western edge of the Sabinar Bank (Figs 6.2 and 6.3) at depths of 820–870 m (Estrada et al., 1997; Gràcia et al., 2006; Lo Iacono et al., 2008). The Chella slide is 3 km long and 2 km wide, whereas the Sabinar slides represent the superposition of several lobes, the largest being 7 km long and 3 km wide (Fig. 6.2). A succession of slide scars is visible to the south of Sabinar Bank, suggesting dismantlement of the margin by retrogressive mass movements (Lo Iacono et al., 2008). This scar system is located at the foot of the slope, in depths of 900–1600 m and with scar widths varying from 750 to 2000 m. The low backscatter observed in sidescan sonar imagery (Fig. 2.6) suggests the landslides and scars are no longer active and are covered by a thin layer of sediment, preserving their original morphologies (Lo Iacono et al., 2008).

The study area contains several fault structures (Fig. 6.2), of which the NE–SW-trending Carboneras Fault is the longest and most prominent (see the following section). Other faults include the Yussuf Fault (Fig. 6.2) and other smaller faults, such as the NW-SE fault system located north of the Carboneras Fault (in the Campo de Dalias area) and the N–S faults observed west of Chella Bank (Fig. 6.3). South of the Carboneras Fault, at a depth of about 1000 m, the sedimentary succession is affected by widely spaced folds (Gràcia et al., 2006) that trend N110° and are 10–23 km long with a wavelength of about 3 km.

Southwest of the Almería Margin, two elongate and prominent NE–SW-trending ridges, the Adra Ridge and the Alboran Ridge, are separated by the Alboran Channel (Fig. 6.2). The Adra Ridge forms the eastern part of the so-called "36°10′N high" (Muñoz et al., 2008) and comprises a 40-km-long horst of metamorphic rocks covered by Neogene volcanics (Maldonado et al., 1992; Comas et al., 1999). This ridge is characterised by a system of NE–SW-trending lineations evident as a succession of ridges and narrow depressions. To the SW, the ridge is right-laterally offset by a NW–SE-trending trough that is 1 km wide and 20 km long, with a maximum depth of 1290 m. The SE margin of the ridge is a 400-m-high NE–SW-trending scarp.

The Alboran Ridge is one of the most distinctive topographic features in the Alboran Basin (Woodside and Maldonado, 1992; Comas et al., 1995) (Fig. 6.2). The ridge is 150 km long, although only the northeastern section of the ridge is shown in Fig. 6.2. The base of the NE Alboran Ridge is defined by the 1200-m depth contour, and its top by the 100-m depth contour (Fig. 6.2). The top is irregular with several highs, one of them emergent (Alboran Island). The Alboran Channel is a narrow

passage between the Adra Ridge and the Alboran Ridge, linking the West and East Alboran basins. The floor of the channel deepens gradually to the northeast from a depth of 1500 m at its western end to 1800 m at its eastern mouth, where the gradient increases from <1° to 3° (Muñoz et al., 2008). The width of the Alboran Channel increases from 2 km in the west to about 20 km in the east.

6.2.2. *The Carboneras Fault Zone offshore*

The offshore CFZ is a NE–SW-trending up-warped zone of deformation defined by *en echelon* and parallel or sub-parallel fault traces, with a length of 90 km and width of 0.5–1.8 km (Figs 6.2 and 6.3). Based on morphology and fault orientation, Gràcia et al. (2006) divided the offshore CFZ into two main segments: the N045° segment, which extends from 36°30′N to the northern link with the emergent fault trace; and the N060° segment, which extends from 36°26′N to the southern end of the fault at 36°18′N. Between the northern and southern segments, the authors describe an intersection zone characterised by an area of complex morphology comprising a narrow (<1 km wide) arcuate ridge interpreted as an underlapping restraining step-over.

Recent, detailed bathymetric data, together with the new sub-seafloor data presented in this thesis, shed light on the surface geometry of the CFZ offshore, as well as on its architecture at depth. The new data enable a revision of the proposed fault segmentation. The segments, herein referred to as the Northern and Southern Carboneras Fault segments (NCF and SCF, respectively) are re-defined (Fig. 6.3). The intersection zone between the northern and southern segments identified by Gràcia et al. (2006) has now been included to the SCF segment based on seismic data which show that the main fault trace of the intersection zone has the same orientation as the SCF segment. The offshore NCF segment is 48.5 km long, trends N047° and continues for 50 km onland in approximately the same orientation (Figs 6.2 and 6.3). It is mainly rectilinear and narrow (usually <500 m wide) with a subdued surface expression and a small NW-facing escarpment. The segment comprises parallel fault traces with the exception of the eastern side of the Andarax Tributary Valley System, where two traces splay to the north and south. Southwards, a change in the orientation of the fault trace at around 36°28′55″N, 2°41′28″W marks the boundary between the NCF and SCF segments. The SCF segment, which is 39 km long, trends N059° for 30 km but shows a changes in orientation (at around 36°20′42″N, 2°58′52″W) to N050° for the last 9 km. The northern part of the SCF is characterised by a relatively wide fault zone with fault splays diverging from the main fault zone towards the SW. Prominent pressure ridges are formed between these fault traces. To the south, there occur 30-m-high smooth SE-facing escarpments with a 5% slope. The southernmost part of the CF is characterised by 45-m-high SE-facing escarpments with a slope of 10%.

6.3. Seismostratigraphic units of the Almería Margin

The tectonic activity of a structure may be reconstructed from the sedimentary record. In offshore areas, the sedimentary sequence is observed in seismic profiles as stacks of seismic reflections with common characteristics (e.g. amplitude and reflector continuity). Since the first seismic surveys in the Alboran Sea, the acoustic facies and main seismostratigraphic units have been widely described and correlated (e.g. Woodside and Maldonado, 1992; Mauffret et al., 1992; Watts et al., 1993; Rodríguez-Fernández and Martín-Penela, 1993; Comas et al., 1995; Estrada et al., 1997; Comas et al., 1999; Alvarez-Marrón, 1999; Booth-Rea et al., 2007). The ages of these seismostratigraphic units have been established from radiometric dating and bio-stratigraphic analyses of sediments and rocks recovered through long cores and drilling wells (e.g. Ocean Drilling Program (ODP) projects).

To study the neotectonic history of the CFZ, a list of previously proposed seismostratigraphic units in the Alboran basin was compiled, and a revised, detailed seismostratigraphy was established from the new high-resolution multi-channel seismic dataset (IMPULS profiles) of the present study. The new seismic units were correlated with those defined previously, and direct correlations were made with units encountered in wells, in order to determine the ages of the units. This new detailed seismostratigraphy is used in the following sections to describe in detail the architecture of the CFZ and variations in structure along its trace. Based on these data, the tectonic evolution of the CFZ is analysed, along with its relation to other structures in the area.

6.3.1. *Previously defined seismostratigraphic units*

Sedimentary units of the Alboran Sea show complex sedimentation patterns linked to tectonic events, sediment supply and variations in global sea-level and climate (Alonso and Maldonado, 1992). Ercilla et al. (1992) differentiated between chaotic and stratified facies, and recognised two subtype facies for each. Chaotic facies occur as 1) wavy and disrupted reflections of medium amplitude that define mounds or lens-shaped bodies, usually bounded by irregular erosional surfaces; or 2) strong, contorted reflections of high acoustic amplitude with hyperbolic and hummocky reflectors, sometimes showing traces of the original bedding. Stratified facies occur as 1) continuous individual reflections of high amplitude and high lateral continuity; or 2) discontinuous individual reflections of low to moderate amplitude with high lateral continuity.

In the Alboran Sea, seismic profiles show an acoustic basement overlain by six seismic units (I–VI in descending stratigraphic order) that infill the Alboran Basin following a layered pattern (Fig. 6.4A). These seismostratigraphic units are bounded by major angular or erosional unconformities that can be correlated across the northern half of the Alboran Basin (Jurado and Comas, 1992). At the Almería

Margin, only the uppermost three units (units I–III, ranging in age from the present-day to the Upper Miocene) are present above the acoustic basement, and unit I has been divided in four Pliocene sequences and one Quaternary sequence (Campillo et al., 1992). Data from commercial wells and ODP sites in the Alboran Basin (e.g. the Andalucía A-1 and ODP Leg 161 sites 977 and 978) enable 1) correlation of the acoustic facies observed in seismic profiles with sedimentation patterns, and 2) determination of the ages of seismic units based on bio-stratigraphic analyses (Alvarez-Marrón, 1999) (Fig. 6.5).

The acoustic basement has been deformed through successive tectonic episodes that controlled the basin evolution generating accommodation space for the sedimentary infill. The seismostratigraphic units show marked lateral variations in thickness and are disrupted by syn- and post-sedimentary faulting. Lateral variations in the thickness and architecture of these units were influenced by the development of horsts and grabens in the basement (Comas et al., 1992). Detailed studies of the top of unit I suggest that the evolution of the Almería Margin was controlled by the interplay between active tectonics, Plio-Quaternary sea-level oscillations and sediment input (Campillo et al., 1992). Data from seismic profiles and sediment cores indicate that Quaternary deposits record a cyclic pattern of deposition comprising alternating hemipelagic and terrigenous inputs into the basin (Alonso and Maldonado, 1992; Estrada et al., 1997).

The following paragraphs describe the main seismostratigraphic units and sedimentary features of the study area, as first reported by Jurado and Comas (1992), Comas et al. (1992), Campillo et al. (1992) and Alonso and Maldonado (1992). These seismostratigraphic descriptions are based on single- and multi-channel seismic data, and the interpretation of geophysical well logs, together with data from commercial wells and observations of sediment cores.

Unit I:

Unit I onlaps most of the basement highs and is relatively thick (>1 sec two way travel time (TWTT)) in the northern Alboran Sea. At the base of this unit, the R1 unconformity (Fig. 6.4A), more widely known as the M (Messinian) unconformity (Ryan and Hsü, 1973; Cita, 1982), is characterised by an irregular high-amplitude reflector that shows marked erosional features and that produces diffraction patterns and coalescing diffraction hyperbolas. Two subunits are distinguished: units Ia and Ib.

Sub-Unit Ia: Pliocene to Recent

Sub-unit Ia is defined by strong parallel reflectors of variable lateral continuity and low amplitude, although occasionally high-amplitude events are observed. Low-amplitude sigmoidal reflections are also recognised within this subunit, downlapping onto the top of the lower subunit (Fig. 6.4A)

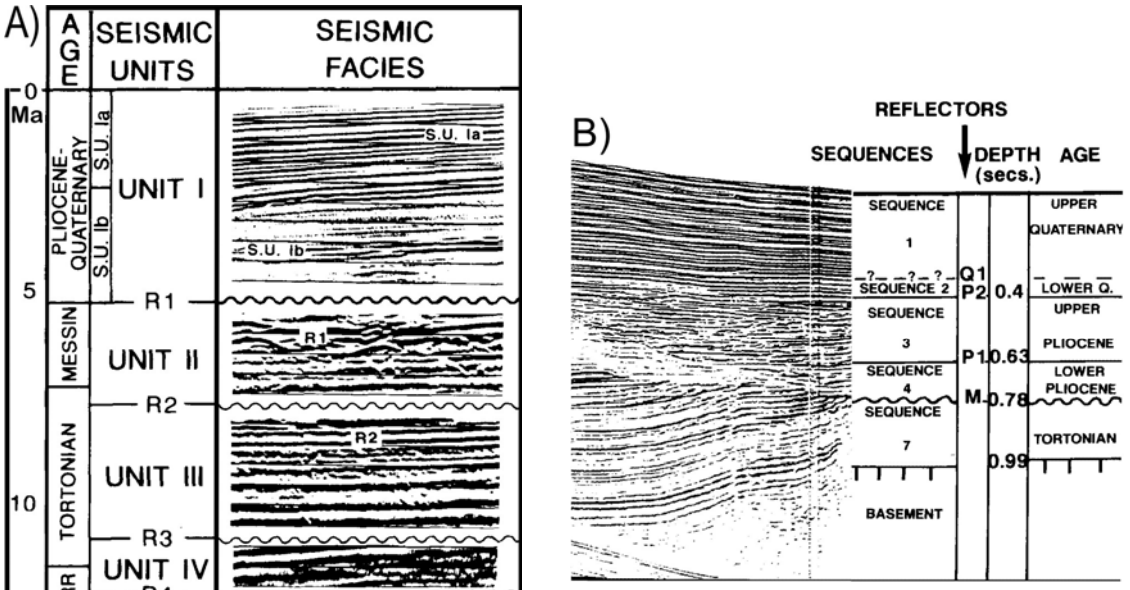

Figure 6.4. A) Representative seismic facies for each seismic unit from the Northern Alboran Sea. The vertical scale is time. The main unconformities that constitute the boundaries of the seismic units are represented by wavy lines. Seismic facies correspond to different profiles from the ALB multi-channel seismic survey (Eniepsa, 1982) (From Jurado and Comas, 1992). B) Seismic stratigraphy based on a representative single-channel seismic line in the Alboran Sea that intersects the DSDP 121 site in the Western Alboran Basin (Modified from Campillo et al., 1992). S.U.: subunit; R: reflector.

(Jurado and Comas, 1992). Based on data from commercial wells, this unit corresponds to clays with sandstone and some pebbly interbeds containing abundant bioclasts. This unit was deposited in a shallow marine environment with a regressive character (a prograding shelf) (Comas et al., 1992).

Based on single-channel seismic data, Campillo et al. (1992) distinguished three sequences in sub-unit Ia. Sequence 1, at the top of the sub-unit, is defined by continuous and parallel reflectors with high acoustic impedance, with the lower boundary being a paraconformity in the basin interior and an unconformity towards the basin margins (Q1 horizon) (Fig. 6.4B). The parallel reflectors locally contain channel and wedge lobe patterns towards the basin margins, indicative of high-energy deposits. The seismic horizons mimic the seafloor morphology, except where incised by canyons. This sequence mainly represents basin ponding by hemipelagic sedimentation, which is locally interrupted at the margins by gravity flows and turbidites.

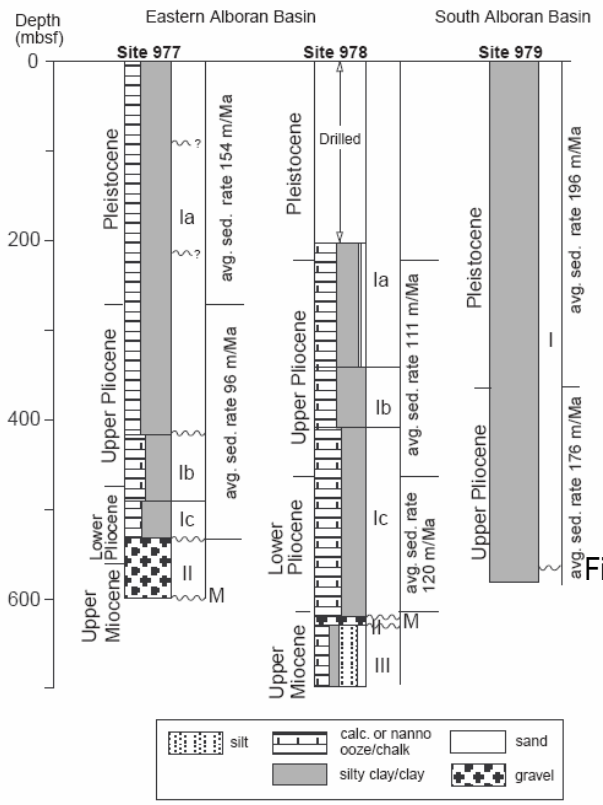

Figure 6.5. Simplified stratigraphy of ODP wells 977, 978 and 979, showing the ages of the main lithologies (from Alvarez-Marrón, 1999) (redrafted from Comas et al., 1996). mbsf: meters below the sea floor.

Sequence 2 is defined by sigmoidal progradational reflections over the basin margins, and continuous, parallel reflectors in the basin interior. The base of this sequence is characterised by onlap terminations at underlying deposits (P2 horizon) (Fig. 6.4B).

Sequence 3 is characterised by channelized facies and short, discontinuous wavy reflectors. Facies with parallel reflectors are also observed, but the reflectors are more widely spaced than in the overlying sequences. The unconformity at the bottom of sequence 3 is locally strongly erosive and is characterised by deeply incised channels. This unit is interpreted to have been deposited as a suite of erosive events, high-energy channelized turbidites and hemipelagic settling processes with significant vertical and lateral variations. Campillo et al. (1992) described this unit as being restricted to the basins and distal sectors of the continental margin, but Alonso and Maldonado (1992) extended the unit up to the slope of the Almería Margin.

Sub-Unit Ib: Pliocene

Sub-unit Ib typically has an overall transparent character, although locally the transparent zones alternate with parallel or divergent reflectors with poor continuity (Fig. 6.4A). Large-scale channel-like features are also identified. Reflectors onlap onto the relief of the Messinian unconformity, which records strong erosion and has an irregular morphology, or onto the acoustic basement (Jurado and Comas, 1992). This sub-unit comprises clays and silty clays with large-scale channel-like

depositional features indicative of a deep-marine environment, representing a distal turbidite system with onlapping features indicating a transgressive period (Comas et al., 1992). This sub-unit, which corresponds to Sequence 4 of Campillo et al. (1992) (Fig. 6.4B), is most well-developed in basins and has a variable thickness. In proximal sectors of the continental margin, it fills depressions that formed between structural blocks.

Unit II: Messinian

Unit II is characterised by chaotic to strong and high-amplitude reflectors with poor lateral continuity, alternating with semi-transparent zones. Pronounced erosional features are evident at its top, with surface irregularities producing diffraction patterns. The base of the unit is marked by the R2 unconformity (Fig. 6.4A), apparent as an angular unconformity characterised by strong, high-amplitude reflections (Jurado and Comas, 1992). The lower part of the unit consists of clays, silts, sandstones and pebbly intervals interbedded with volcanic rocks and volcaniclastic layers, topped by carbonates in the northeastern Alboran Sea (Comas et al., 1992). These deposits were deposited in a distal marine environment along with minor evaporitic and carbonate facies. The absence of a well-developed Messinian evaporite series is remarkable when compared with neighbouring Mediterranean areas.

In a study of higher-resolution profiles, Campillo et al. (1992), who termed this unit ‘sequence 5’, reported numerous internal unconformities and a lower boundary that generally onlaps the basin margins and structural highs.

Unit III: Tortonian

Unit III is defined by strong reflectors with parallel to divergent geometries. The seismic character and thickness of the unit show marked lateral variations. Strong parallel reflectors change laterally to near-transparent zones with chaotic and discontinuous reflections. The top of unit III is erosional over large areas, representing an angular unconformity (Jurado and Comas, 1992). This unit comprises clastic deposits that range from very fine-grained (clays) to coarse-grained (pebbly sandstones) sediment, along with graded sequences and some channel-like features with coarse-grained intervals (Comas et al., 1992).

Acoustic basement

The acoustic basement is mainly free of intracrustal reflections and its rough top causes scattering and poor energy attenuation (Booth-Rea et al., 2007). Although the basement over most of the Alboran Sea is generally considered to be metamorphic in nature (e.g. Maldonado et al., 1992; Comas et al., 1992), at the Almería Margin it is of volcanic origin (Duggen et al., 2004).

6.3.2. *New seismostratigraphic sequences identified in IMPULS seismic profiles*

6.3.2.1. Facies and key horizons identified in TOPAS profiles

Analyses of TOPAS profiles indicate the occurrence of various seismic facies in the Almería Margin (Fig. 6.6), including: (1) parallel-bedded stratification, which is the most common facies in the area, typically observed in flat areas; (2) divergent-bedded stratification, observed at the margins of leveed channels and canyons; (3) semi-transparent facies, usually interbedded with parallel-bedded stratification; (4) low-penetration chaotic facies, located at the bottom of the Almería Canyon and channels; (5) hyperbolic facies, locally observed within tributary valley systems; (6) bedding alternating with chaotic facies, which is widely observed; (7) opaque facies corresponding to volcanic outcrops; and (8) stratified prograding wedge which corresponds to shelf facies. Most of these facies are affected by faults and folds, especially by the CFZ. The parallel-bedded stratification is the most suitable facies with which to define vertical offset across the fault zone and with which to assess paleoseismic parameters.

Based on the seismic facies, four seismic units have been identified in the uppermost sedimentary cover, first described within the area of the DTVS (García et al., 2006) (Fig. 6.7). These units occur throughout the entire Almería Margin and are recognised in the TOPAS profiles from the IMPULS cruise, with slight variations in thickness between areas of gullies and areas sloping, planar seafloor. The age of each unit has been revised in the present study (see Chapter 7), with ages ranging from the Late Pleistocene to the Holocene.

TOPAS Unit I

The lowermost unit shows parallel-bedded facies with average thickness varying between 7 and 10 m at the DTVS area. The unit is thickest in the slope area of the Almería Margin (15–20 m). The top of the unit is usually observed as a marked double reflection, which is the strongest reflection observed in the TOPAS profiles.

TOPAS Unit II

Unit II is characterised by a semi-transparent facies and tabular geometry, with an almost constant thickness of about 5 m throughout the entire Almería Margin.

TOPAS Unit III

Unit III shows parallel-bedded facies with high reflectivity and a thickness of 4–12 m (average, 8–10 m). Its top is commonly observed as a neat double reflection.

TOPAS Unit IV

The youngest unit is characterised by semi-transparent facies, with a thickness of 7 m at the DTVS. It locally shows hyperbolic facies at the central sector of the DTVS. In smooth areas of the Almería slope area, the unit is relatively thin (2–4 m).

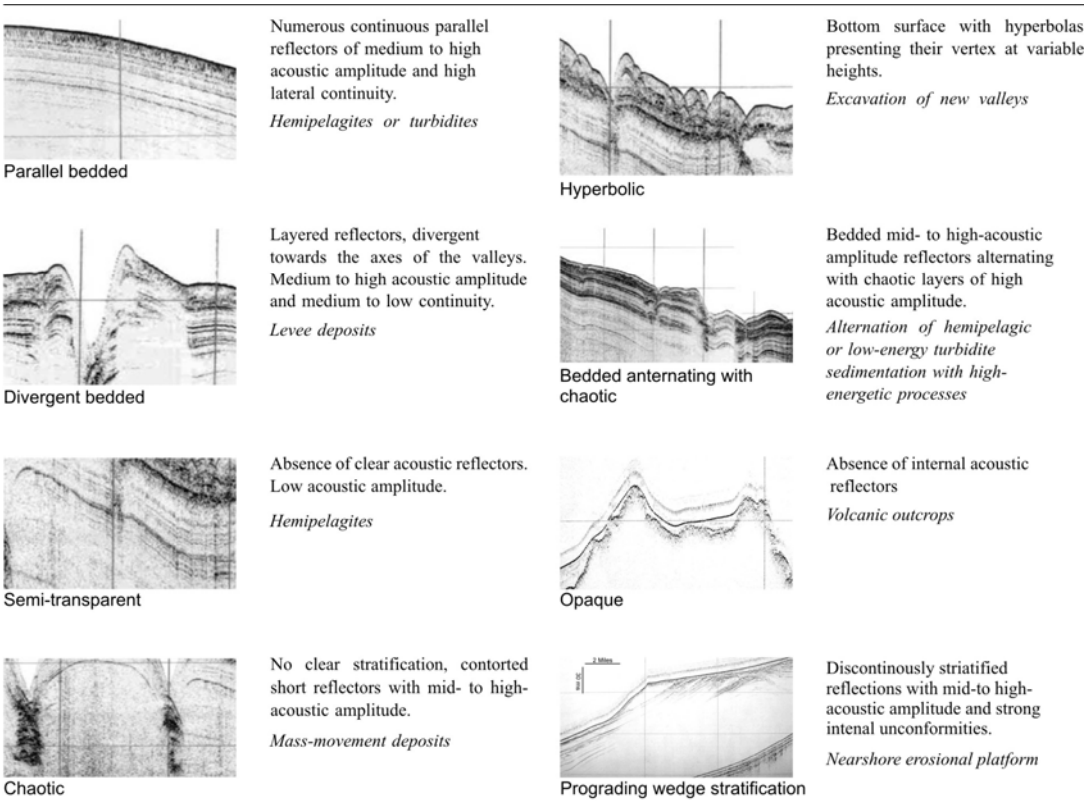

Figure 6.6. TOPAS images, showing descriptions and interpretations of the main seismic facies associations observed at the Almería margin (modified from García et al., 2006).

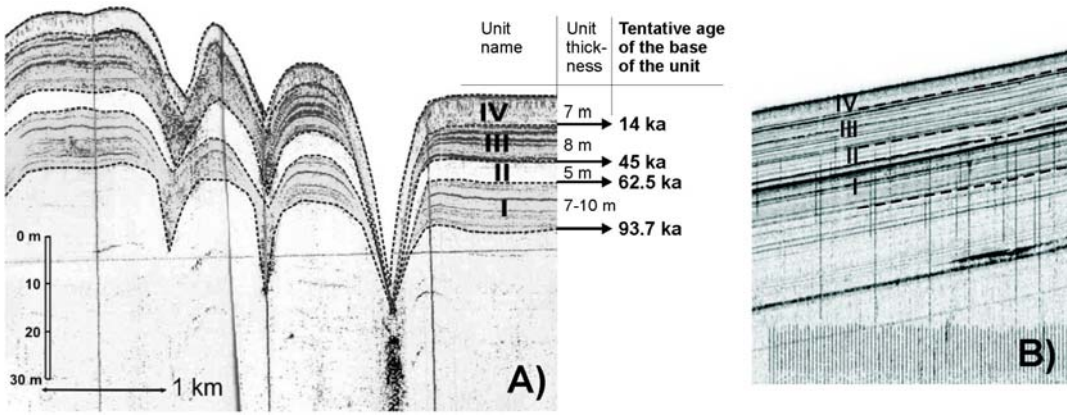

Figure 6.7. A) TOPAS profile showing the TOPAS seismic units (I to IV) at the Almería Margin, as described by García et al. (2006). Tentative ages are provided for the base of each unit, calculated from sedimentation rates reported in paleoceanographic studies of the Alboran Sea (Cacho et al., 1999) (further discussed in Chapter 7). (Modified from García et al., 2006). B) Identification of the TOPAS seismic units in the central section of the IMPULS IM-101 profile (see Fig. 6.1 for the location of the profile).

7.1.1.1. High-resolution MCS seismic units

Above the acoustic basement, eight units (Ia.1, Ia.2, Ia.3, Ia.4, Ib.1, Ib.2, II, and III) have been identified in the IMPULS high-resolution MCS profiles and extrapolated to the Sparker profiles. The new seismic units correlate to units Ia, Ib, II, and III of Jurado and Comas (1992). The six uppermost units (Ia.1–Ib.2) correspond to the four Plio-Quaternary sequences described by Campillo et al. (1992). The characteristics of these units are better defined in deeper parts of the area, far from active structures. Figure 6.8 shows the SE end of profile IM-11, where the eight units are observed and where the seismostratigraphy of the area has been defined.

Unit Ia.1: In the present study area, unit Ia.1 is evident as continuous and parallel reflectors of moderate amplitude with lenses of wavy and disrupted reflectors. The reflections show lateral changes to a more irregular, chaotic or even transparent facies associated with mass transport deposits in the slope domain or channel infill in flat areas. Upon the shelf, this unit clearly shows prograding sigmoids. The maximum thickness of this unit is seen at the base of the slope, where the TWTT is 0.1 sec (approximately 75 m). At the CFZ, the unit is generally uplifted and is commonly eroded in shallow areas. Its base is defined by a strong and continuous reflector (**S1 horizon)** which locally marks a smooth angular unconformity, particularly evident upon the shelf. This unit corresponds to Sequence 1 of Campillo et al. (1992) and is Late Quaternary in age (Fig. 6.8).

Unit Ia.2: The top of unit Ia.2 is similar to the uppermost unit, with moderate-amplitude, continuous and parallel reflectors. Towards deeper parts, there is a transition to low-amplitude, discontinuous facies. At the shelf, the unit is observed as a pile of parallel and wedge-shaped groups of reflectors. At the Almería fan area, the base of this unit is relatively thick and is evident as wavy and discontinuous reflections, probably related to fan lobe deposits. The unit is always overlain by unit Ia.1 (except at the CFZ near the shelf, where the upper unit has been removed by erosion) and has the same pattern of thickness as unit Ia.1. The base of this unit is marked by the **S2 horizon,** characterised by high-amplitude parallel reflectors with good lateral continuity, although low-angle unconformities are locally observed at the slope and base of the slope. At the shelf, this unit is highly erosive and the S2 reflection marks an angular unconformity. This unit corresponds to Sequence 2 of Campillo et al. (1992) and is Early Quaternary in age (Fig. 6.8).

Unit Ia.3: Unit Ia.3 is characterised by parallel and continuous reflectors of high amplitude with interbedded transparent wedges corresponding to mass movement deposits. At the shelf, it is observed as alternating parallel and continuous reflections with transparent layers. At the slope, this unit has a lower amplitude and is relatively thin, showing a transition to a semi-transparent zone. Its base is marked by the **S3 horizon,** which is a high-intensity, laterally continuous, and negative-polarity reflector. The unit is parallel to overlying units and is relatively thin, with a maximum thickness (at the base of the slope) of 0.06 s TWTT (approximately 45 m). This unit corresponds to the upper part of Sequence 3 of Campillo et al. (1992) and is Late Pliocene in age.

Unit Ia.4: Similarly to the overlying unit, Ia.4 is widely characterised by high-amplitude parallel and continuous reflectors with intercalated wedged facies which correspond to mass movement deposits. Its upper reflections usually have poor lateral continuity and are of low amplitude, corresponding to transparent facies. The base of the unit is

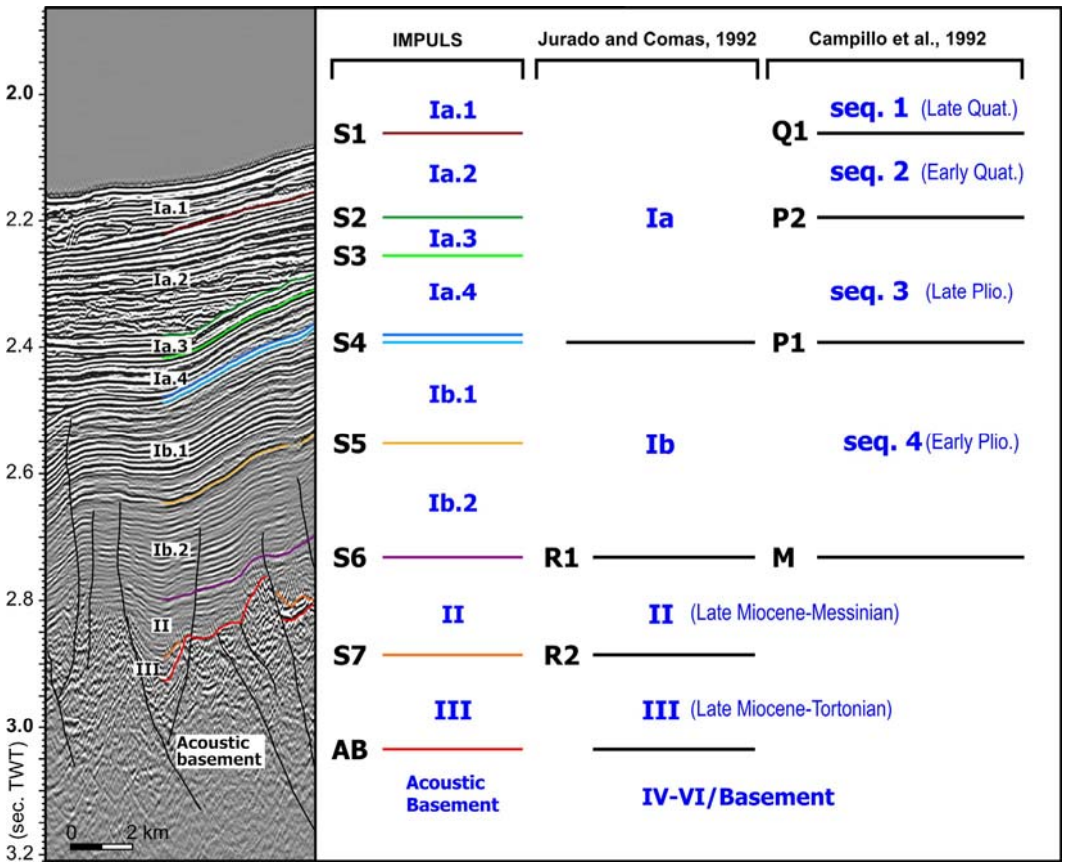

Figure 6.8. Seismostratigraphic units identified in IMPULS profiles and correlation with units defined in previous studies. The profile section corresponds to the SE end of the HR-MCS IM-11 profile (see Fig. 6.1).

defined by the **S4 horizon,** for which the base is usually defined by a strong positive reflection (light blue line in Fig. 6.8). However, this reflection is laterally discontinuous; consequently, the overlying continuous reflection (dark blue line in Fig. 6.8) is followed. The thickness of unit Ia.4 is greatest in the area of the Almería Canyon, where it is 0.1 s TWTT (approximately 80 m). This unit is correlated with the lower part of Sequence 3 of Campillo et al. (1992) (Fig. 6.8), which is Late Pliocene in age, and the S4 horizon is correlated with the P1 unconformity of Campillo et al. (1992).

Unit Ib.1

Unit Ib.1 is characterised by low amplitudes relative to the upper units, and shows a gradual decrease in amplitude toward its base. It is defined by parallel to sub-parallel continuous reflectors of low to moderate amplitude. The thickness of reflections is laterally variable. For example, a single thick reflector changes laterally to two or more smaller reflectors. At the shelf, wavy and chaotic layers are interbedded with parallel low-amplitude reflectors. The base of the unit is marked by the **S5 horizon,** defined by an alternating positive/negative/positive group of reflections with high amplitude and very poor continuity. The thickness of Ib.1 is

variable, with maximum values to the NW of the Carboneras Fault (0.3 s TWTT, approximately 250 m) and minimum values at the CFZ and basement highs. This unit corresponds to the upper part of Sequence 4 (Early Pliocene) of Campillo et al. (1992) (Fig. 6.8).

Unit Ib.2

The general decrease in amplitude from overlying units to unit Ib.1 is intensified in unit Ib.2, characterised by subparallel, discontinuous low-amplitude reflectors. At the shelf, parallel and low-amplitude reflectors are intercalated with wavy and chaotic layers. Some chaotic wedge-shaped bodies are also observed. The base of the unit is defined by the **S6 horizon,** which is correlated with the M unconformity at the top of Miocene deposits. This unconformity is highly erosive and was formed during the Messinian salinity crisis, being defined as a very high-amplitude reflection. However, at the Almería Margin this characteristic pattern is not laterally continuous. Its thickness is variable, with maximum values NW of the Carboneras Fault and west of the Chella Bank (0.3 s TWTT, approximately 250 m). The lateral continuity of the unit is often interrupted by basement highs. This unit is correlated with the lower part of unit Ib of Jurado and Comas (1992), and is Early Pliocene in age (Fig. 6.8).

Unit II

The top of unit II is usually defined by high-amplitude hummocky reflectors with poor continuity, changing laterally to semi-transparent facies, which also occurs at depth within the unit. The reflectors commonly toplap the overlying unit and the lower reflections downlap onto basement. This unit is not continuous throughout the study area, occurring as infill within small paleo-basins that occur between basement highs. The unit overlies the acoustic basement or overlies the lower part of unit III across an angular unconformity (**S7 horizon**). The maximum thickness is observed west of the Chella Bank (0.3 s TWTT, approximately 250 m). This unit corresponds to unit II (Late Miocene) of Jurado and Comas (1992).

Unit III

Unit III is poorly represented in the study area, occurring as patches of paleo-basin infill with a thickness of 0.1–0.2 s TWTT. It is more extensive to the west of the Chella Bank, at the mouth of the Alboran Channel, where it is defined by alternating thick, high-amplitude, reflectors with poor continuity and low-amplitude reflectors with poor continuity. The maximum thickness at the mouth of the Alboran Channel is 0.2 s TWTT (approximately 180 m). In the study area, this unit always overlies the acoustic basement.

6.3.3. *Ages of MCS seismic horizons based on analyses of commercial wells*

The IMPULS seismic stratigraphic units were correlated, based on facies descriptions, with bio-stratigraphically dated units from other studies (e.g. Jurado and Comas, 1992). In addition, the IMPULS seismic stratigraphy was directly correlated with the Andalucía A-1 commercial well (Fig. 6.9). The IM-11 profile was designed to intersect with the Andalucía A-1 well, which was drilled on the shelf of the Almería Margin (36°36′04″N and 2°44′04″W) by the Elf oil company in 1981 (Lanaja, 1987) (Fig. 6.1 and inset in Fig. 6.9). The boundaries of the stratigraphic units in the Andalucía A-1 well (Fig. 6.9), which have been described and dated, were converted to seconds (TWTT) using Normal Move Out (NMO) velocities from the commercial MCS profile AM-156 (inset in Fig. 6.9), and projected onto the MCS profile IM-11. Then, the well units were correlated with the IMPULS seismic horizons S5, S6, S7, and AB. The ages of the seismostratigraphic unconformities are coincident with the ages proposed in previous works (Fig. 6.8): a) horizon S5 corresponds to a Lower Pliocene (3.6–5.3 Ma) reflection; b) horizon S6 represents the base of the Pliocene (approximately 5.3 Ma), corresponding to the strongly erosive M (Messinian) unconformity; and c) horizon S7 corresponds to the base of the Upper Miocene (Tortonian?).

The Upper Pliocene and Pleistocene boundaries have been tentatively correlated with those identified at Site 978 of ODP Leg 161, in the Eastern Alboran Basin (Figs 6.2) (Shipboard Scientific Party, 1996). Although none of the seismic profiles used in this study intersects with ODP site 978, the eastern sections of the IMPULS profiles (located at the base of the slope) show similar depositional patterns to the ODP site 978 area. Thus, the IMPULS profiles show similar seismic stratigraphy to that of other MCS lines acquired near Site 978 (e.g. the TECALB, Conrad, and EVENT-DEEP profiles; Fig. 3.2). Based on this similarity, the ages of horizons S2, S3 and S4 have been inferred, and are coincident with the ages of the units identified by Campillo et al. (1992), as follows: a) horizon S2 corresponds to the base of the Calabrian stage, defined by the first occurrence of *Geophyrocapsa oceanica* (Shipboard Scientific Party, 1996), at 1.8 Ma; b) horizon S3 corresponds to the base of the Gelasian stage (established as the new base of the Quaternary period since 2009), defined by the extinction of *Discosaster pentaradiatus* and *Discosaster surculus* (Shipboard Scientific Party, 1996), at 2.6 Ma; and c) horizon S4 corresponds to the Lower/Upper Pleistocene boundary, defined from the general biostratigraphy (Shipboard Scientific Party, 1996), at 3.6 Ma.

In summary, based on the information obtained from the Almería A-1 well, Site 978 of ODP Leg 161, and previous seismostratigraphic studies of the area, the ages of the IMPULS seismic units have been established and are summarised in Table 6.1.

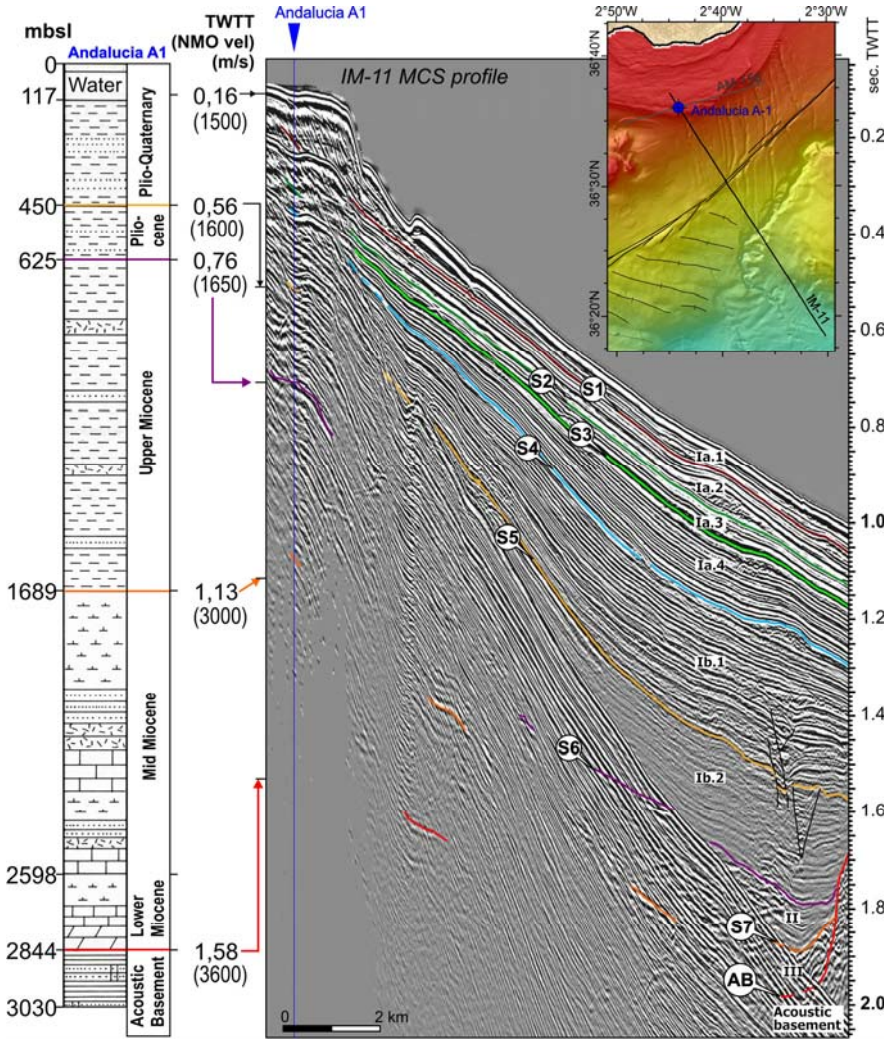

Figure 6.9. Projection of the Andalucia-A1 commercial well along the NW section of the HR-MCS profile IM-11 acquired during the IMPULS survey. Depths of unit boundaries are in meters below sea level (at the left of the well log) and are converted to TWTT (at the left of the seismic profile) using NMO velocities (in brackets) obtained from the commercial profile AM-156 from the same area. Inset: location of the Almería A-1 well, AM-156 commercial seismic line and IM-11 MCS profile. mbsl: meters below sea level; TWTT: two-way travel time.

Table 6.1: Summary of the ages of seismic units and horizons identified in IMPULS MCS profiles.

Age	Unit name	Seismic horizon
Late Quaternary	Ia.1	S1
Early Quaternary	Ia.2	S2→*Base of Calabrian stage (1.8 Ma)*
	Ia.3	S3→*Base of Gelasian stage (2.6 Ma)*
Late Pliocene	Ia.4	S4→*Lower/Upper Pliocene boundary (3.6 Ma)*
Early Pliocene	Ib.1	S5
	Ib.2	S6→*Messinian unconformity*
Late Miocene	II	S7
	III	Top of the acoustic basement
Neogene?	Acoustic Basement	

6.4. Characterization of structures at depth

The use of seismic methods with various resolutions enables imaging of the shallow and deep tectonic architecture of the CFZ and other nearby structures. The sedimentary units that overlie basement are affected by the CFZ, which is generally characterised by sub-vertical faults. Fault traces are rarely seen below the top of acoustic basement because of the massive internal structure of the basement and its relatively homogenous seismic facies, which prevents the identification of displacement upon faults. The CFZ is laterally variable in terms of its structure. Within the NCF and SCF segments, second-order structural segments (sub-segments) are also identified according to the structures observed in seismic profiles. These sub-segments are described below.

6.4.1. *The submarine North Carboneras Fault segment*

Based on seismic data, the submarine portion of the North Carboneras Fault (NCF), which strikes N047°, is divided in three structural sub-segments (from north to south: NCF-1, -2 and -3; Fig. 6.10a) which are respectively characterised by 1) a positive flower structure, 2) a vertical fault zone forming a pressure ridge, and 3) a narrow, vertical fault zone with uplift on the SE side and a gradual decrease in the intensity of deformation towards the SW.

Sub-segment NCF-1 extends for 19 km from the shelf to 36°40′45″N, with an average trend of N047.3° (Fig. 6.10a,b). Along the fault zone, sedimentary units are deformed and uplifted in a 4–5-km-wide band of sub-vertical fault traces that appear to converge at depth, forming a positive flower structure (see profile IM-18 in Fig. 6.13). The fault traces that reach the surface (i.e. active faults) are concentrated in the central part of the deformation zone, and sedimentary sequences are faulted and folded along a 1.0–1.5-km-wide fault zone (see profile EVE-1 in Fig. 6.13). Moreover, some of the fault traces that reach the seafloor have a bathymetric expression, indicating present-day or very recent fault activity. In profile IM-18, Quaternary units appear to be absent in the fault zone, indicating they were never deposited in this region or were uplifted and removed by erosion. However, the uppermost 75 m of the fault zone in this area is clearly depicted by the TOPAS system, as Upper Quaternary TOPAS units are faulted at least up to unit II (see profiles IM-213 and IM-201 in Fig. 6.11). Moreover, the occurrence of growth strata indicates ongoing fault activity in recent times.

Profile EVE-1 (Fig. 6.13) shows the S2 horizon as a highly erosive surface, representing a strong angular unconformity between the Lower Pleistocene and Upper Pleistocene units, as only observed on the shelf area. This erosion is interpreted to reflect a decrease in sea level during this period (beginning of the Calabrian stage), which is consistent with the start of a major glaciation that produced a sea-level drop (lowstand), thereby generating pronounced erosional

surfaces on the shelf. HR-MCS profiles show deeper-level imaging of the features described above.

Sub-segment NCF-2 extends for 7 km from 36°40′45″ to 36°38′12″, with a dominant orientation of N045.4° (Fig. 6.10a,b). Only the central fault trace of the flower structure sub-segment continues towards the SW, and a new parallel fault trace gives way to a right-overlapping step-over, generating a 500-m-wide pressure ridge between the two traces. The fault zone comprises several vertical fault traces, some of which displace the Quaternary S3 horizon (see profile IM-204 in Fig. 6.14). The younger units are also probably faulted, although they are not imaged in the HR-MCS profiles due to the size of the source-wavelet in the first arrivals (i.e. the first three reflectors below the seafloor). In any case, the higher-resolution TOPAS system shows offset reflections at least up to the base of TOPAS unit III (see IM-profile 204 in Fig. 6.11). This fault trace appears to extend to the surface, although higher-resolution imaging is required to confirm this observation.

Sub-segment NCF-3 extends for 25 km from 36°38′23″ to 36°29′17″, with a dominant orientation of N046.8° (Fig. 6.10a,b). This sub-segment is approximately 400 m wide along most of the fault zone, although the width increases to 1 km in its central part, along a 6-km-long fault trace that is parallel to the main fault trace. Based on its width, this sub-segment is described in terms of the following three parts, from north to south.

a) At the end of the SE trace of sub-segment NCF-2, the fault zone becomes narrower and simpler. Along the first 10 km of sub-segment NCF-3, Plio-Quaternary faulting is concentrated in a 400-m-wide fault zone of vertical fault traces, with uplift to the SE (see profile IM-16 in Fig. 6.14). Smooth flexures are evident on each side of the fault zone, indicating the deformation occurs in a 1-km-wide zone. Towards the most recent units, the fault zone becomes narrower (approximately 200 m wide; see profile IM-16 in Fig. 6.11) and some fault traces reach the seafloor with a bathymetric expression, suggesting active faulting or very recent activity.

The architecture of the sedimentary infilling of the Almería Canyon is observed SE of HR-MCS profile IM-16. Plio-Quaternary reflections are disrupted at the flanks of the canyon, depicting the canyon morphology at the time of each horizon. A V-shaped valley is apparent in the acoustic basement, which would have controlled the location of the canyon.

b) At the DTVS area, between 36°34′58″N and 36°32′31″N, a newly recognised 6-km-long fault trace runs parallel to the CFZ, 700 m to the NW (Fig. 6.10a,b), meaning that the fault zone in this area is 1-km wide. This new fault trace shows an offset up to the S3 reflection at the base of the Quaternary units, in contrast to the main fault zone to the SE, which affects all the Quaternary units up to the S1 horizon (see profile IM-14 in Fig. 6.15). The new fault trace is considered to be active because it deforms Quaternary units, although most of the recent deformation is concentrated along the main fault trace to the SE.

c) Farther south, the trace (located NW of the main fault) ends, and the fault zone narrows again to 450-m wide (Fig. 6.10a,b), with uplift on the SE side that affects all the Quaternary seismic units, at least up to the S1 horizon (see profiles IM-11 and IM-12 in Fig. 6.15). Close to the seafloor, the fault zone becomes narrower (approximately 200 m wide) and all the units up to the base of the youngest TOPAS unit IV are folded and displaced by several fault strands (see profile IM-11 in Fig. 6.12). The deformation extends to the surface, indicating active faulting or very recent activity. At depth, immediately below the fault zone, the flanks of a prominent 2-km-wide basement high coincide with inactive fault traces, suggesting that the fault zone was wider during the early stages of faulting (see profiles IM-12 and IM-11 in Fig. 6.15). Farther south, the intensity of deformation in the fault zone shows a rapid decrease and the fault zone narrows to only 80 m wide (see profile IM-301 in Fig. 6.15). Near-surface sediments are affected by mild Quaternary deformation (see profile IM-301 in Fig. 6.12) compared with sediments located farther NE. This weakening of deformation is interpreted to indicate the end of the NCF segment.

In the central part of the HR-MCS IM-11 profile (Fig. 6.15), the Almería Channel shows a smooth architecture compared with the IM-16 HR-MCS profile described above (Fig. 6.14). In addition, the basement beneath the channel shows no evidence of V-shaped relief, instead occurring as a flat area bounded by two small highs. At the SE tip of the HR-MCS IM-11 profile, the occurrence of lobes of the Almería fan produces a thickening on the Quaternary units above the S2 reflection, suggesting that on the left flank of the Almería Channel, the fan was initiated at the beginning of the Calabrian stage.

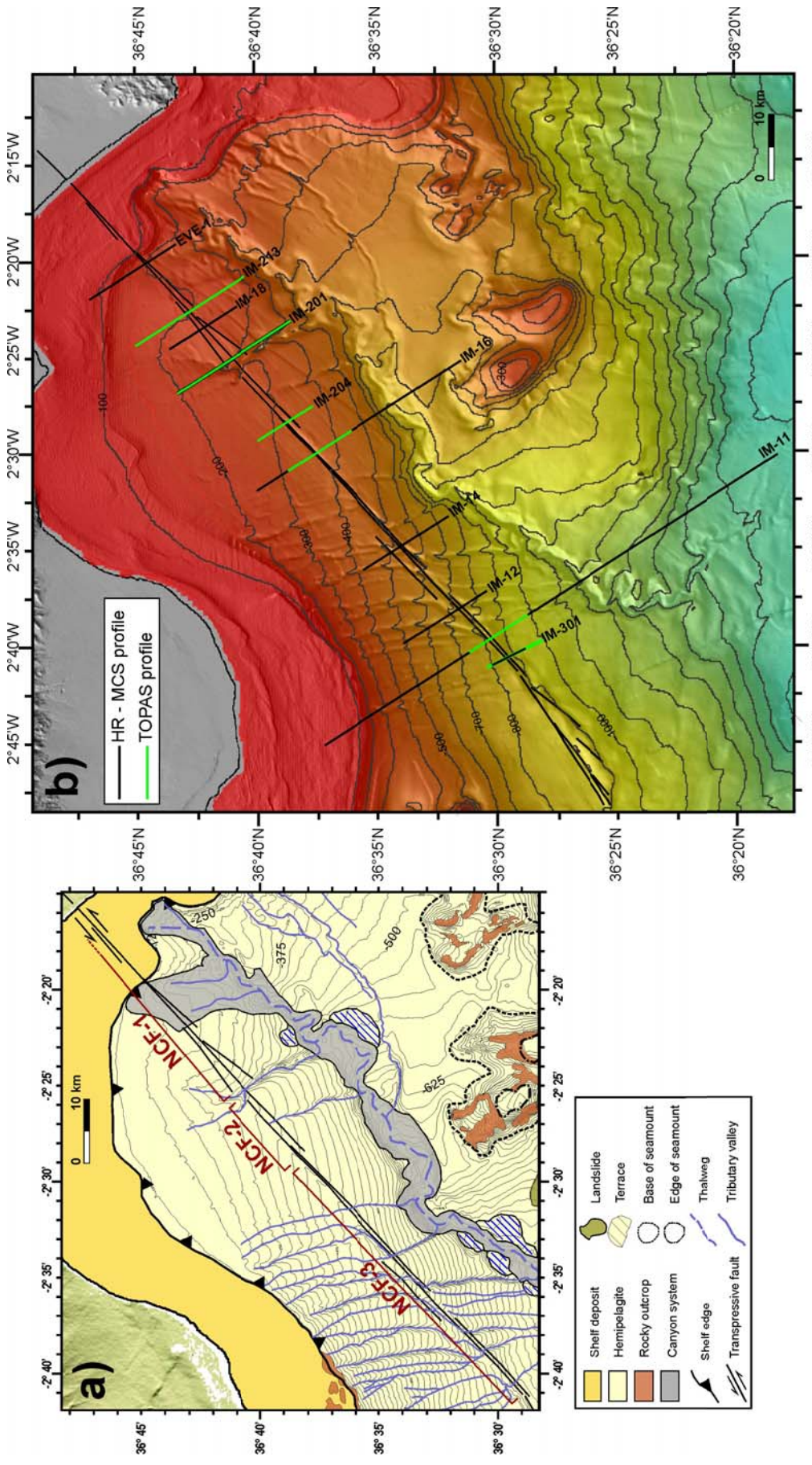

Figure 6.10. a) Geomorphological map showing the structural sub-segments of the submarine North Carboneras Fault segment. b) Bathymetric map of the Northern Carboneras Fault segment and location of the HR-MCS, Sparker and TOPAS profiles shown in Figs 6.11–6.15.

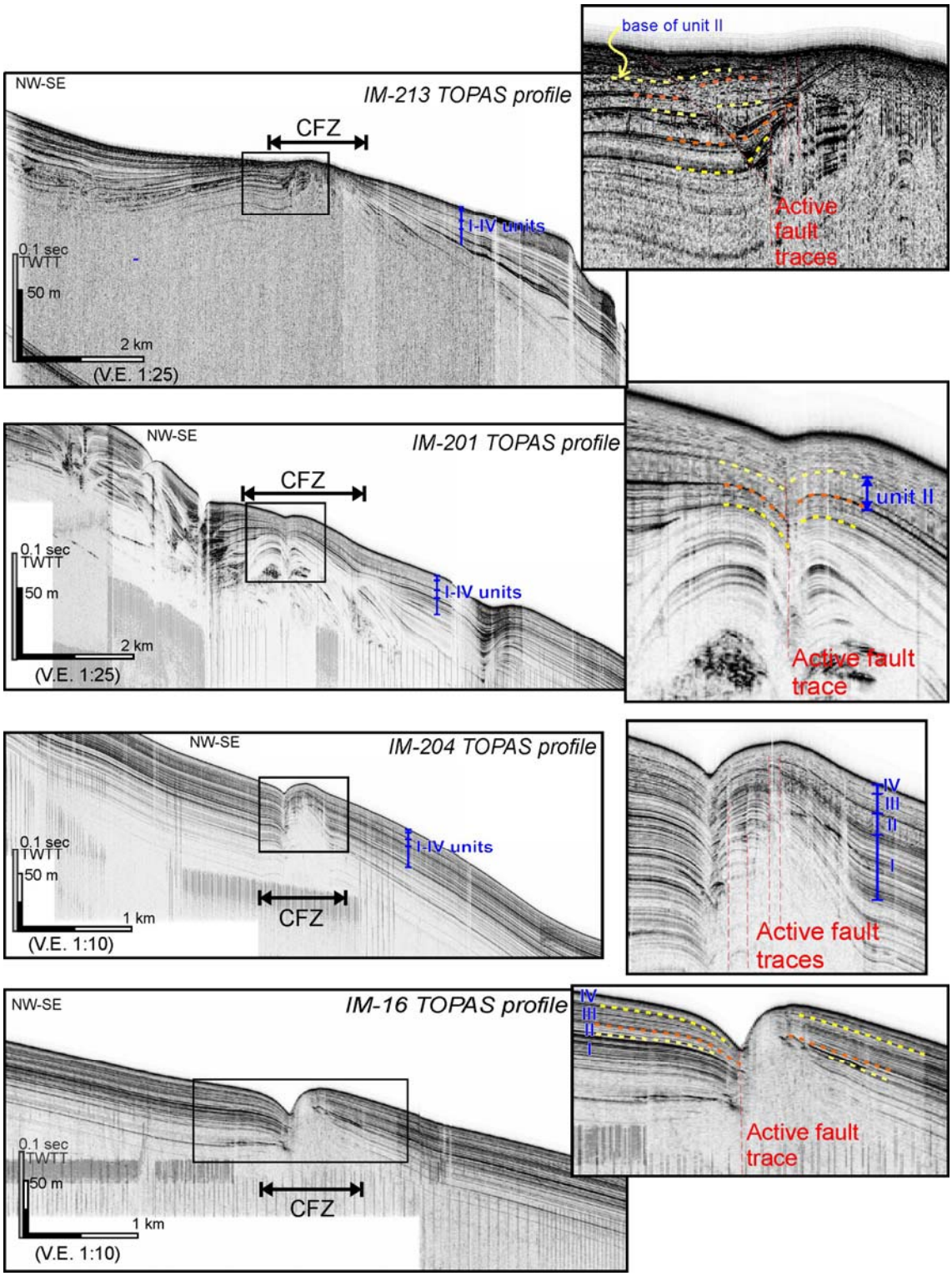

Figure 6.11. TOPAS profiles across the northern part of the submarine North Carboneras Fault segment (rectangles indicate the enlarged areas shown to the right). Dashed lines show the boundaries between units. The vertical scale (m) was calculated using the velocity of sound in water (1500 m/s). For profile locations, see the bathymetric map in Fig. 6.10b. V.E.: Vertical exaggeration; CFZ: Carboneras Fault Zone; TWTT: two way travel time.

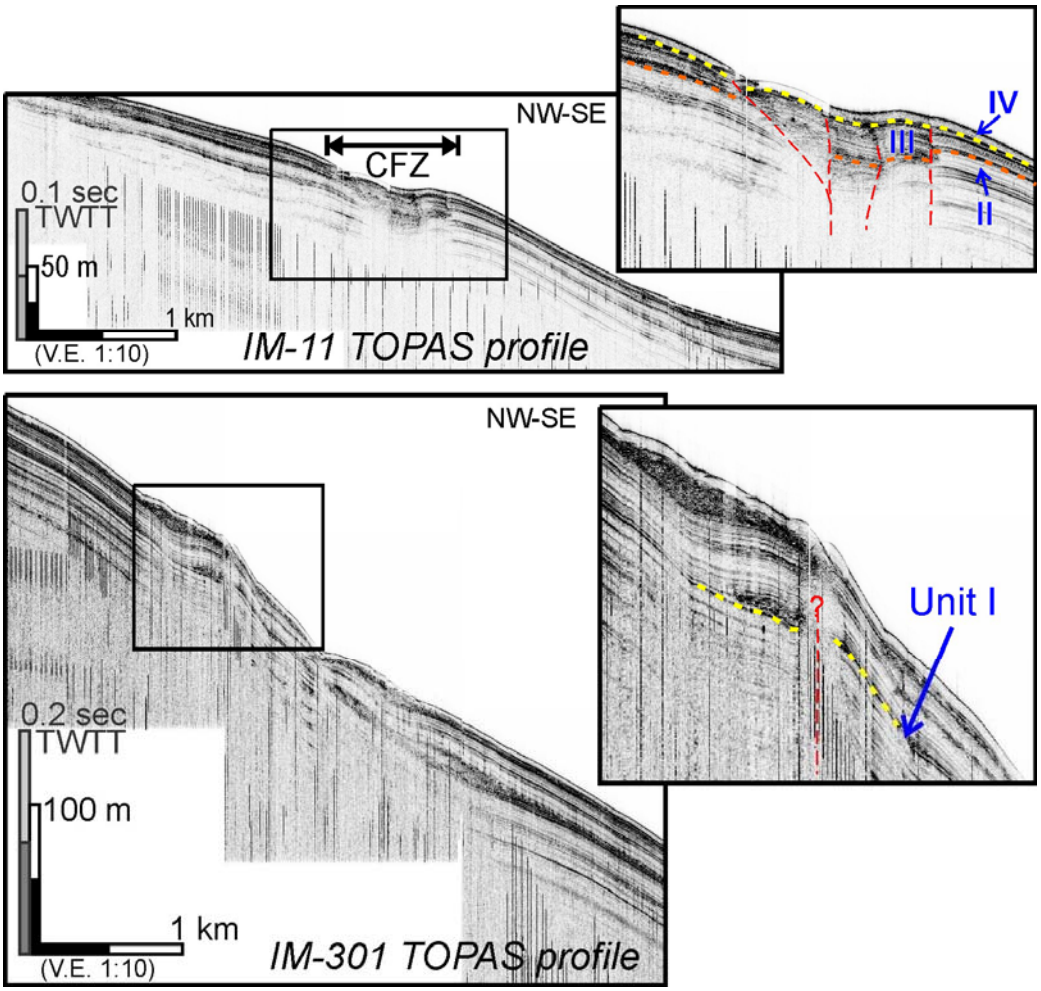

Figure 6.12. TOPAS profiles across the southern part of the North Carboneras Fault segment (rectangles indicate the enlarged areas shown to the right). Dashed lines show the boundaries between units. Red dotted lines are faults. The vertical scale (m) was calculated using the velocity of sound in water (1500 m/s). For profile locations, see the bathymetric map in Fig. 6.10b. V.E.: Vertical exaggeration; CFZ: Carboneras Fault Zone; TWTT: two way travel time.

Following pages:

Figure 6.13. Sparker line EVE-1 and HR-MCS profile IM-18 across the northern part of the submarine North Carboneras Fault segment, corresponding to sub-segment NCF-1 (positive flower structure). Vertical exaggeration is 10:1 for profile EVE-1 and 5:1 for profile IM-18, taking into account the velocity of sound in water (1500 m/s). For profile locations, see the bathymetric map in Fig. 6.10b.

Figure 6.14. HR-MCS profiles IM-204 and IM-16 across the central part of the submarine North Carboneras Fault Segment, corresponding to sub-segment NCF-2 (pressure ridge). Vertical exaggeration is 10:1 for profile EVE-1 and 5:1 for profile IM-16, taking into account the velocity of sound in water (1500 m/s). For profile locations, see the bathymetric map in Fig. 6.10b.

Figure 6.15. HR-MCS profiles IM-14, IM-12, IM11 and IM-301 across the southern part of the Northern Carboneras Fault Segment, corresponding to the sub-segment NCF-3 (narrow vertical fault zone). Vertical exaggeration is 5:1 for all profiles, taking into account the velocity of sound in water (1500 m/s). For profile locations, see the bathymetric map in Fig. 6.10b.

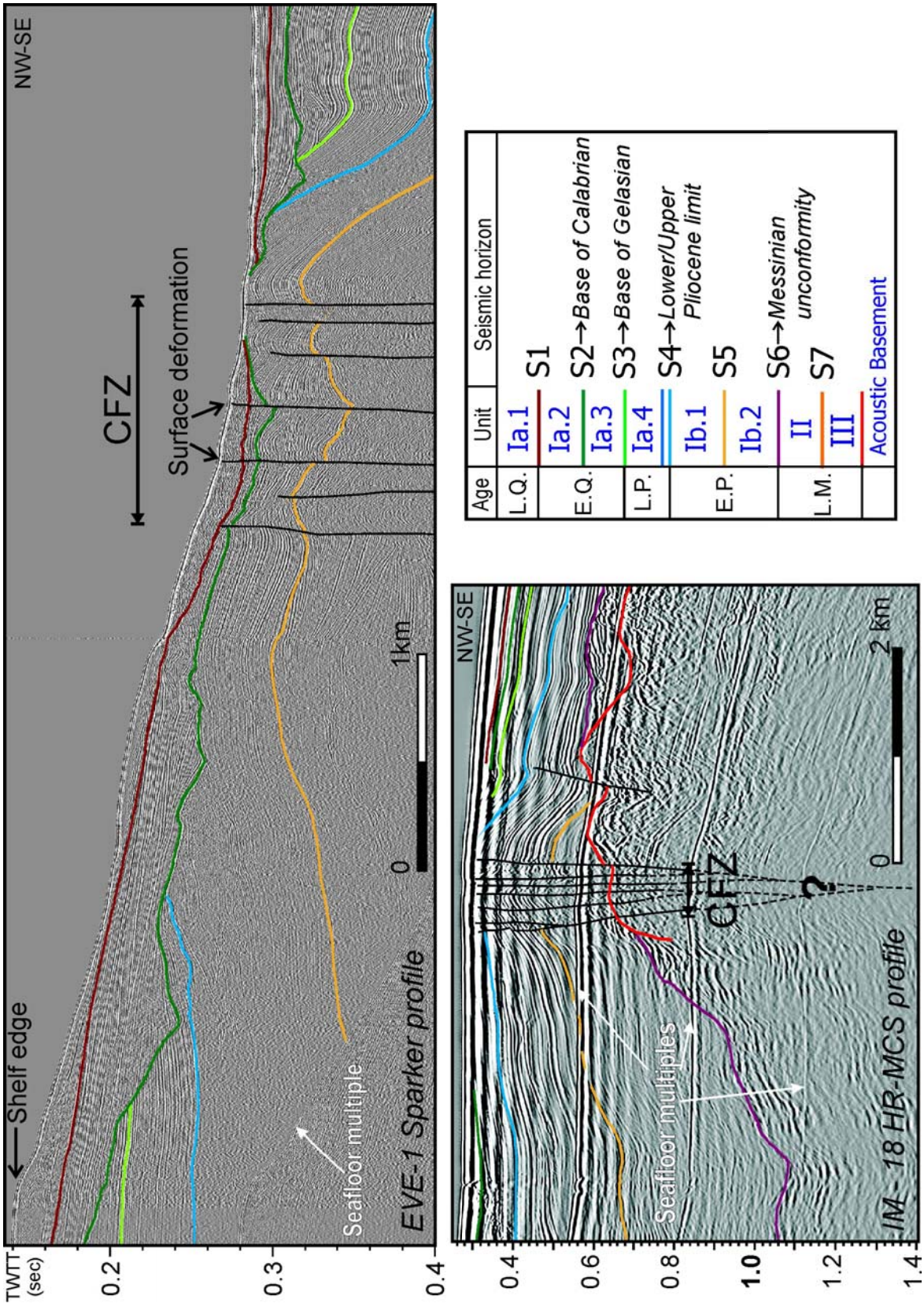
NW-SE
Shelf edge
CFZ
Surface deformation
Seafloor multiple
EVE-1 Sparker profile
0
1km
TWTT (sec)
0.2
0.3
0.4
Age
Unit
Seismic horizon
L.Q.
Ia.1
S1
Ia.2
S2→Base of Calabrian
E.Q.
Ia.3
S3→Base of Gelasian
L.P.
Ia.4
S4→Lower/Upper Pliocene limit
Ib.1
E.P.
S5
Ib.2
S6→Messinian unconformity
L.M.
II
S7
III
Acoustic Basement
NW-SE
CFZ
?
Seafloor multiples
0
2 km
IM- 18 HR-MCS profile
0.4
0.6
0.8
1.0
1.2
1.4

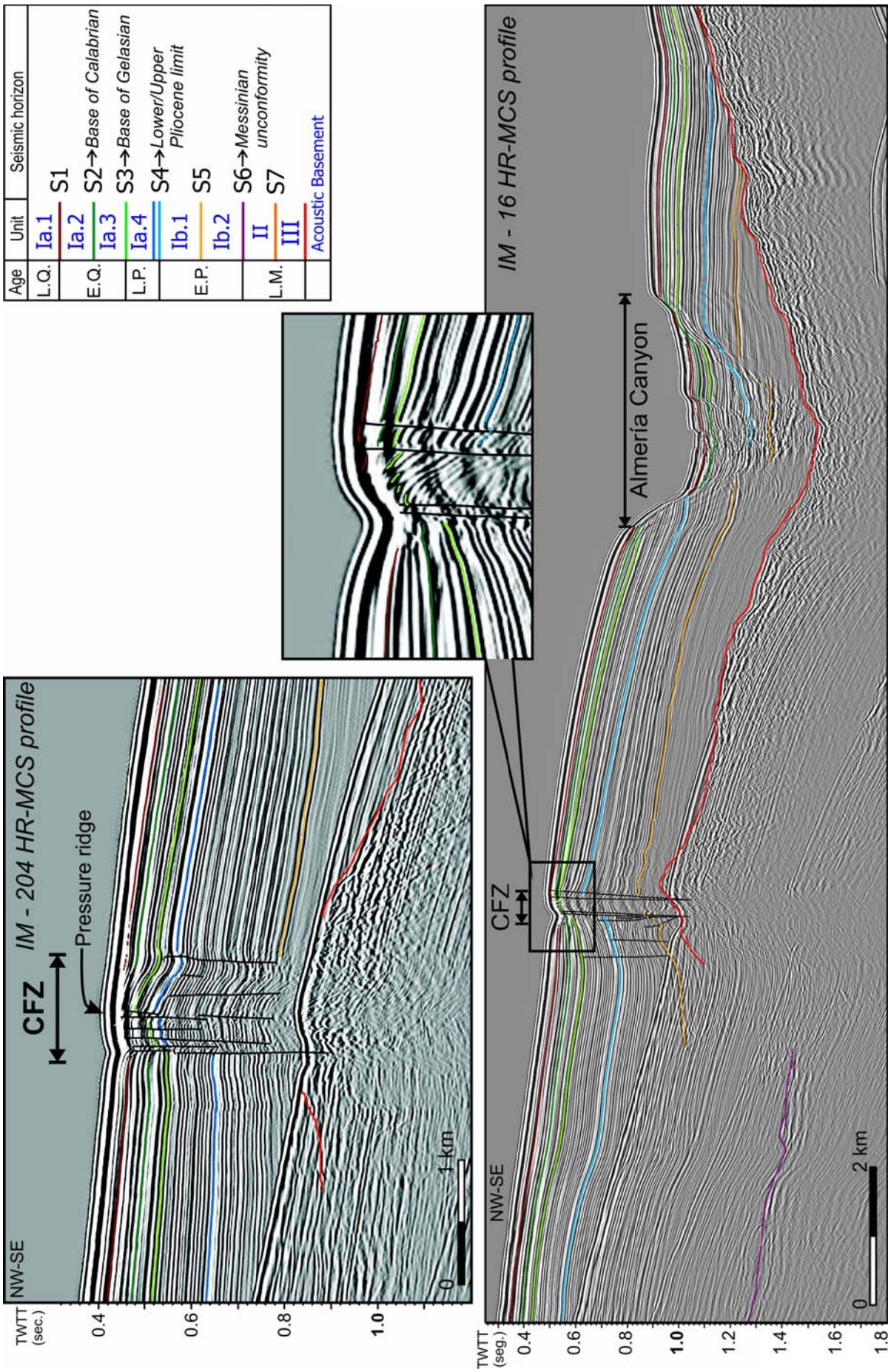
Age
Unit
Seismic horizon
L.Q.
Ia.1
S1
Ia.2
E.Q.
S2→Base of Calabrian
Ia.3
S3→Base of Gelasian
L.P.
Ia.4
S4→Lower/Upper Pliocene limit
Ib.1
E.P.
S5
Ib.2
S6→Messinian unconformity
II
L.M.
S7
III
Acoustic Basement
IM - 204 HR-MCS profile
CFZ
Pressure ridge
NW-SE
TWTT (sec.)
0.4
0.6
0.8
1.0
0
1 km
IM - 16 HR-MCS profile
Almería Canyon
CFZ
NW-SE
TWTT (seg.)
0.4
0.6
0.8
1.0
1.2
1.4
1.6
1.8
0
2 km

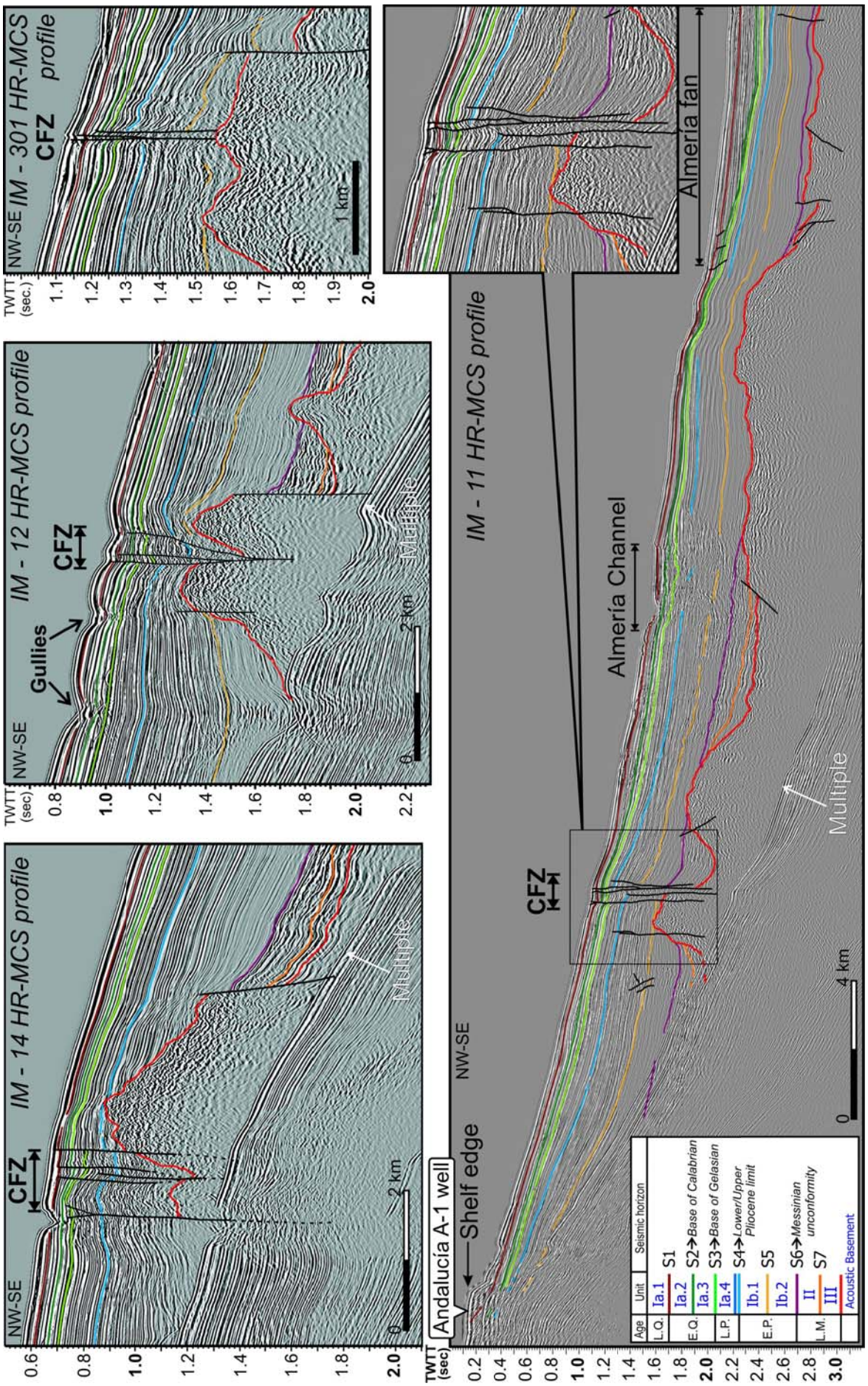
IM - 14 HR-MCS profile
IM - 12 HR-MCS profile
IM - 301 HR-MCS profile
IM - 11 HR-MCS profile
CFZ
Gullies
Multiple
Andalucía A-1 well
Shelf edge
Almería Channel
Almería fan
NW-SE
TWTT (sec.)
2 km
4 km
1 km
Age
Unit
Seismic horizon
L.Q.
E.Q.
L.P.
E.P.
L.M.
Ia.1
Ia.2
Ia.3
Ia.4
Ib.1
Ib.2
II
III
S1
S2→Base of Calabrian
S3→Base of Gelasian
S4→Lower/Upper Pliocene limit
S5
S6→Messinian unconformity
S7
Acoustic Basement

6.4.2. *The South Carboneras Fault segment*

The N059°/050°-trending Southern Carboneras Fault (SCF) segment shows variable tectonic architecture along its trace. Based on seismic observations, this segment is divided into three structural sub-segments (from north to south: SCF-4, SCF-5 and SCF-6; Fig. 6.16a) characterised by prominent pressure ridges with a dominant orientation of N059°, a narrow vertical fault zone trending N059°, and a narrow vertical fault zone trending N050°, respectively. Along SCF-5 and SCF-6, uplift occurs on the NW side, and along each sub-segment, the intensity of deformation shows a gradual decrease towards the south.

Sub-segment SCF-4 extends for 20 km from 36°29′01″N to 36°23′14″N, with an average orientation of N057.7° (Fig. 6.16a,b). The segment is defined by two pressure ridges, both narrowing to the NE and described separately below.

a) The northern pressure ridge is 10 km long and reaches its maximum width (1.2 km) at its southern part, and its maximum height (about 75 m) towards its northern part; the average height is around 30 m. This pressure ridge is observed at depth as a prominent basement high (1.3–2.3 km wide) bounded by faults, some of them inactive (see the IM-10 and IM-09 HR-MCS profiles in Fig. 6.18). The most recently active faults are concentrated on the NW side of the basement high, along a fault zone of 100–500 m in width. On the NW side of this sub-segment, the main fault zone is marked by an elongate "sag pond"-like feature showing growth strata since the Early Pliocene (see the IM-09 HR-MCS profile in Fig. 6.18), indicating ongoing activity since this time. The faults on the NW flank of the sag pond reach the surface and displace all the TOPAS units (see profile IM-304 in Fig. 6.17), indicating recent fault activity. The HR-MCS profile IM-10 (Fig. 6.18) crosses the NE end of the pressure ridge with a smooth present-day surface expression but marked by a prominent basement high with the top surface located at only 0.1 s TWTT (about 100 m) below the seafloor. On the NW side of the fault zone, the occurrence of growth strata since the Early Pliocene is consistent with the above interpretation of ongoing fault activity.

To the SE, the HR-MCS profile IM-10 (Fig. 6.18) shows deposits of the Almería fan lobe including sedimentary units above the S5 Lower Pliocene horizon, suggesting that the fan became active on this flank of the Almería Channel during this time.

b) The southern pressure ridge is 7.5 km long and 1 km wide at the surface (Fig. 6.16a,b). It reaches heights of 30–45 m above the seafloor and is observed at depth as a smooth anticline developed in Plio-Quaternary sedimentary units, bounded by sub-vertical faults (see the IM-310 HR-MCS profile in Fig. 6.18). The most recent active faults are concentrated along the NW edge of the ridge and displace the younger units below the seafloor, at least up to unit II, and surface deformation is apparent (see profile IM-08 in Fig. 6.17).

Sub-segment SCF-5 extends for 10 km from 36°23′14″N to 36°20′37″N, with an average orientation of N062° (Fig. 6.16a,b). In the north, this sub-segment is a 200-m-wide vertical fault zone with minor uplift to the NW, and there is a southward decrease in the width of the fault zone and in the amount of vertical displacement (see profiles IM-07, IM-313 and IM-316 in Fig. 6.19). Deformation is concentrated close to the fault zone, evident as slight flexures in seismic horizons within several hundred meters of the fault zone. Fault activity has continued throughout the Quaternary, as indicated by the displacement of TOPAS units (see the IM-06 TOPAS profile in Fig. 6.17), although the amount of displacement is less than that along the other sub-segments.

The IM-07 HR-MCS profile (Fig. 6.19) also shows a vertical fault to the NW of the main CFZ, displacing the S3 horizon (base of the Quaternary), indicating an active structure. However, this fault is not apparent on the bathymetric map or on TOPAS profiles from the area; consequently, its geometry (e.g. orientation and length) are unknown. On the same profile, other faults, located SE of the CFZ, displace seismic units up to the base of the Quaternary. These faults define a 2.5-km-wide zone of deformation that contains fold with axes that trend N110° (Fig. 6.16a), as discussed in the following section.

Sub-segment SCF-6 extends for 9 km from 36°20′39″N to 36°17′32″N, with an average orientation of N050.3° (Fig. 6.16a,b). It consists of a single vertical fault trace evident as smooth flexures in the seismic reflections on both sides of the fault (see profile IM-05 in Fig. 6.20). At depth, this sub-segment is similar in appearance to the end of sub-segment SCF-5, but with greater intensity of deformation. The basement top shows a vertical offset of 0.1 s TWTT (about 100 m), and the base of the Quaternary (S3 horizon) is offset by 0.09 s TWTT (about 80 m). The higher-resolution TOPAS system shows a 45-m-high scarp and displacement of the most recent TOPAS units across a very narrow fault zone (see profile IM-05 in Fig. 6.17). This fault zone may represent a single trace, as seen in the HR-MCS IM-05 profile, although this possibility cannot be confirmed due to the loss of TOPAS signal intensity in steeply dipping zones. To the SW, there is a decrease in deformation along the CFZ, with a smooth reduction in the amount of vertical offset (see profile IM-04 in Fig. 6.20) until it is no longer apparent (see profile IM-03 in Fig. 6.20).

Other faults are observed in HR-MCS profiles IM-05, IM-04 and IM-03 (Fig. 6.20), defining wide deformation zones to the NW and SE of the SCF-6 sub-segment, although with very little, if any, offset of the basement. These structures, associated with folds that trend N110°, or to the NW-SE pervasively faulted zone, are discussed in the following section. However, it is remarkable that the combination of some of these structures with the CFZ results in a graben-like structure within the basement and overlying units (see profile IM-05 in Fig. 6.17), which should not be confused with extension related to the CFZ itself.

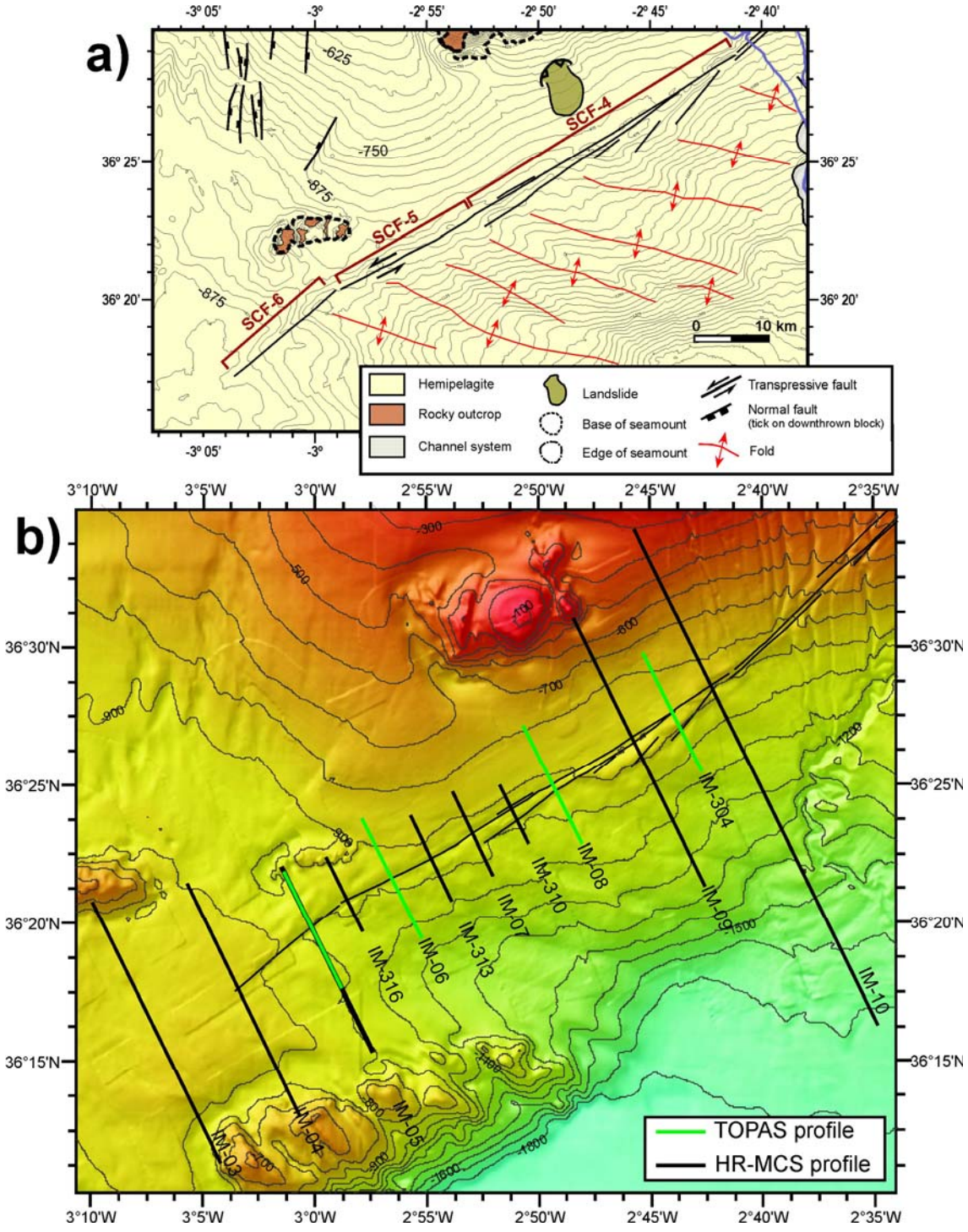

Figure 6.16. a) Geomorphological map showing the structural sub-segments of the South Carboneras Fault segment. b) Bathymetric map of the Southern Carboneras Fault segment and location of the HR-MCS and TOPAS profiles presented in Figs 6.17 to 7.20.

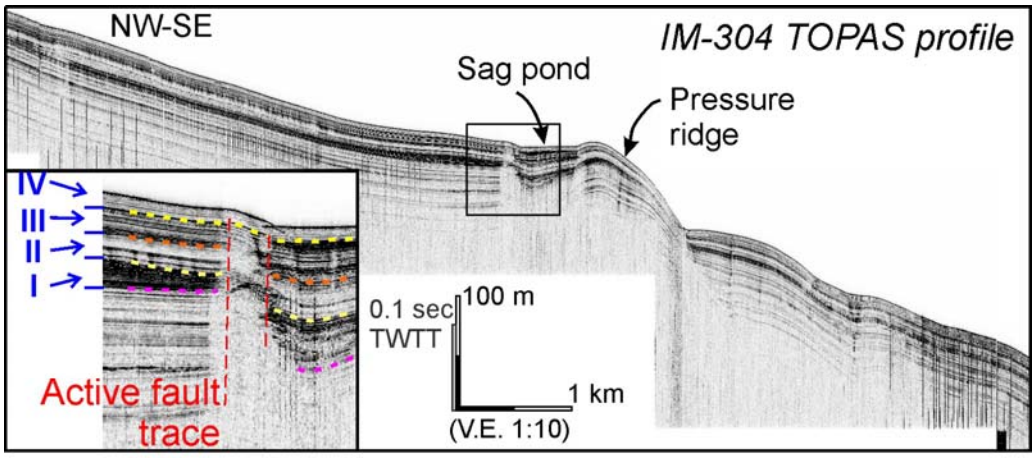
NW-SE
IM-304 TOPAS profile
Sag pond
Pressure ridge
IV
III
II
I
Active fault trace
0.1 sec TWTT
100 m
1 km
(V.E. 1:10)

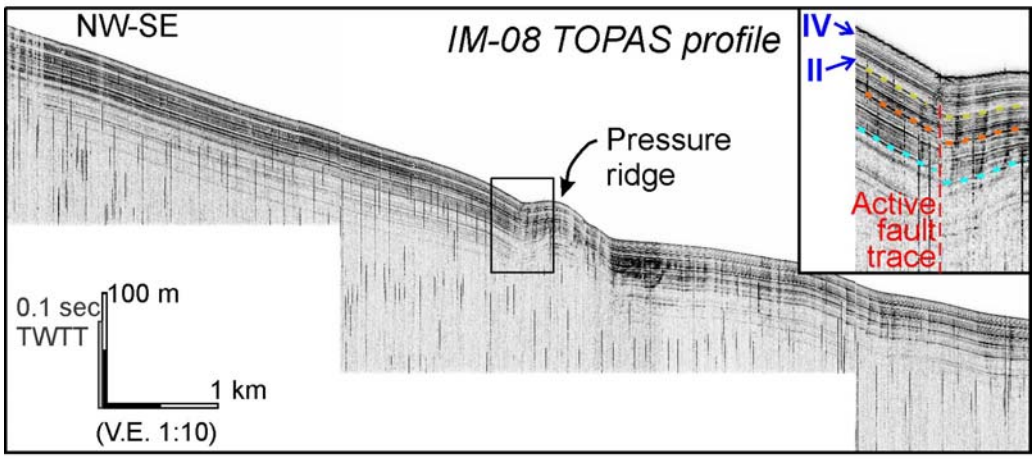
NW-SE
IM-08 TOPAS profile
IV
II
Pressure ridge
Active fault trace
0.1 sec TWTT
100 m
1 km
(V.E. 1:10)

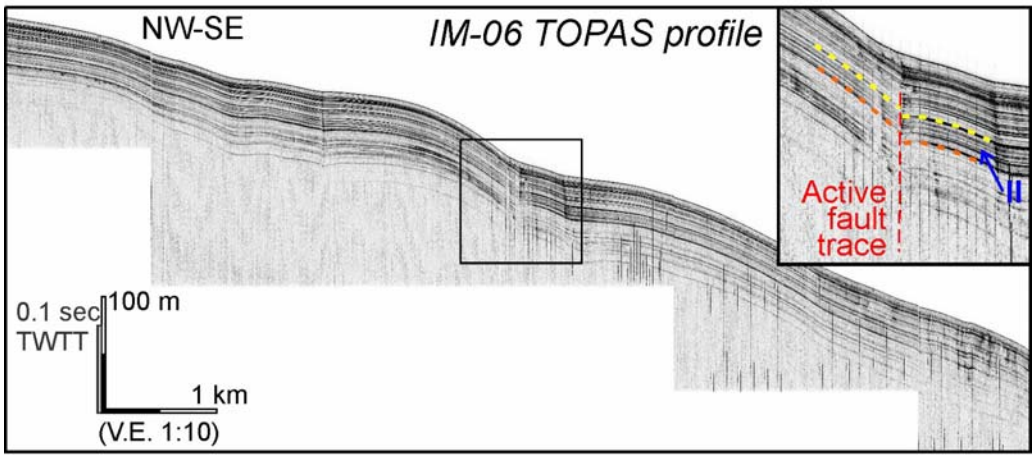
NW-SE
IM-06 TOPAS profile
Active fault trace
II
0.1 sec TWTT
100 m
1 km
(V.E. 1:10)

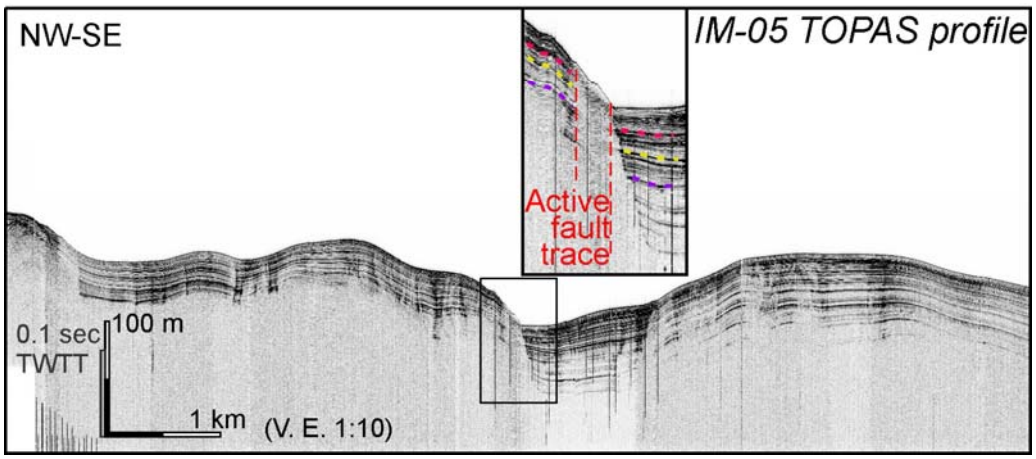
NW-SE
IM-05 TOPAS profile
Active fault trace
0.1 sec TWTT
100 m
1 km
(V. E. 1:10)

Figure 6.17. (Previous page) From north to south: IM-304, IM-08, IM-06 and IM-05 TOPAS profiles across the South Carboneras Fault segment. Rectangles indicate the enlargements shown in the insets. Dotted lines indicate unit boundaries. The vertical scale (m) was calculated taking into account the velocity of sound in water (1500 m/s). Vertical exaggeration for all TOPAS profiles is 10:1. For profile locations, see Fig. 6.16b.

Following pages:

Figure 6.18. HR-MCS profiles IM-10, IM-09 and IM-310 across the northern part of the Southern Carboneras Fault segment, corresponding to sub-segment SCF-4 (pressure ridges). Vertical exaggeration is 5:1 for all the profiles, taking into account the velocity of sound in water (1500 m/s). For profile locations, see the bathymetric map in Fig. 6.16b.

Figure 6.19. HR-MCS profiles IM-07, IM-13 and IM-316 across the northern part of the Southern Carboneras Fault segment, corresponding to sub-segment SCF-5 (N059°-trending, narrow vertical fault zone). Vertical exaggeration is 5:1 for all the profiles, taking into account the velocity of sound in water (1500 m/s). For profile locations, see the bathymetric map in Fig. 6.16b.

Figure 6.20. HR-MCS profiles IM-05, IM-04 and IM-03 across the northern part of the Southern Carboneras Fault segment, corresponding to sub-segment SCF-6 (N050°-trending, narrow vertical fault zone). Vertical exaggeration is 5:1 for all the profiles, taking into account the velocity of sound in water (1500 m/s). For profile locations, see the bathymetric map in Fig. 6.16b.

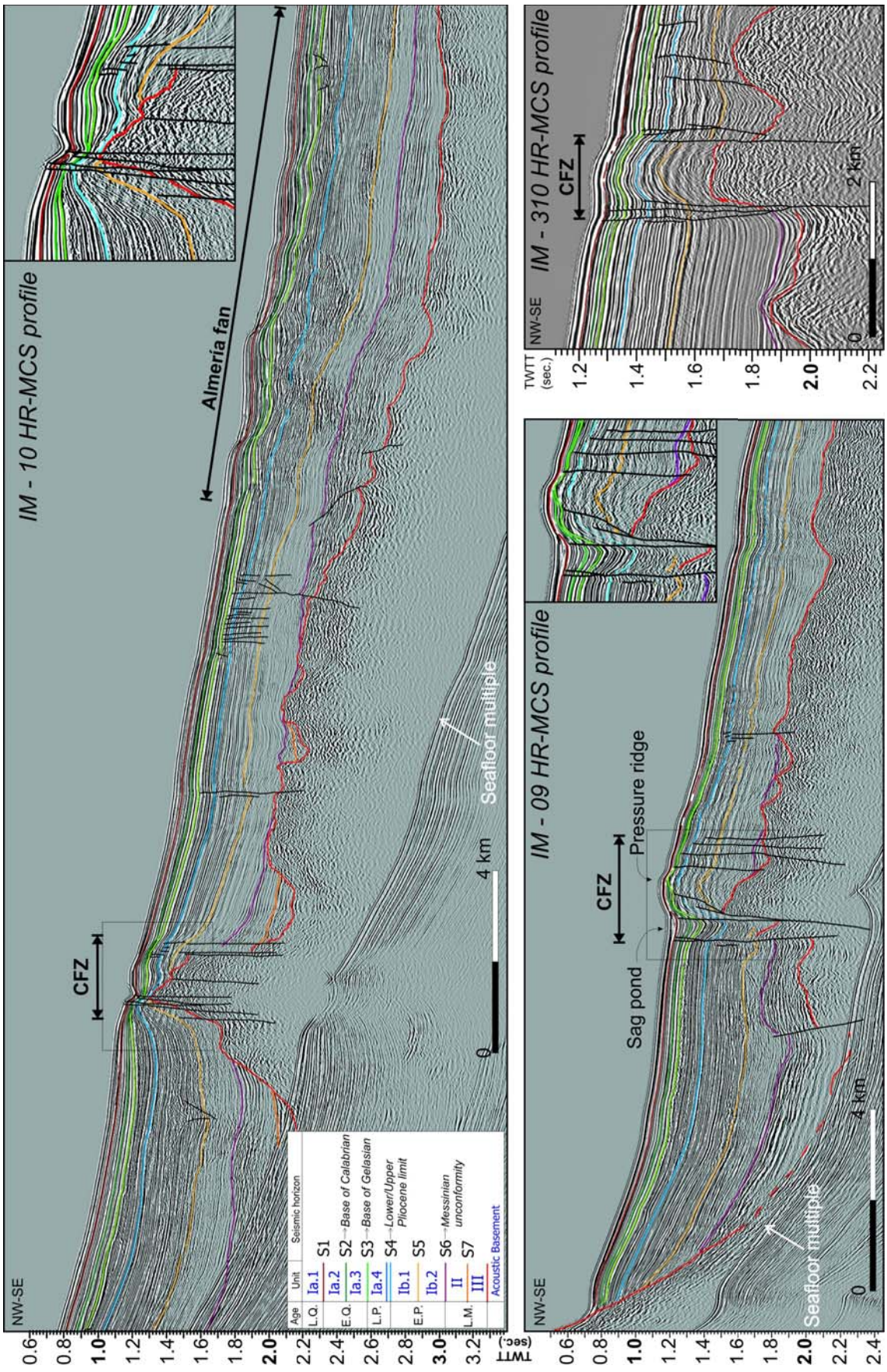
IM - 10 HR-MCS profile
NW-SE
CFZ
Almería fan
Seafloor multiple
4 km
0
Age
Unit
Seismic horizon
L.Q.
Ia.1
S1
Ia.2
S2→Base of Calabrian
E.Q.
Ia.3
S3→Base of Gelasian
L.P.
Ia.4
S4→Lower/Upper Pliocene limit
Ib.1
S5
E.P.
Ib.2
S6→Messinian unconformity
L.M.
II
S7
III
Acoustic Basement
TWTT (sec.)
IM - 09 HR-MCS profile
Sag pond
Pressure ridge
IM - 310 HR-MCS profile
2 km

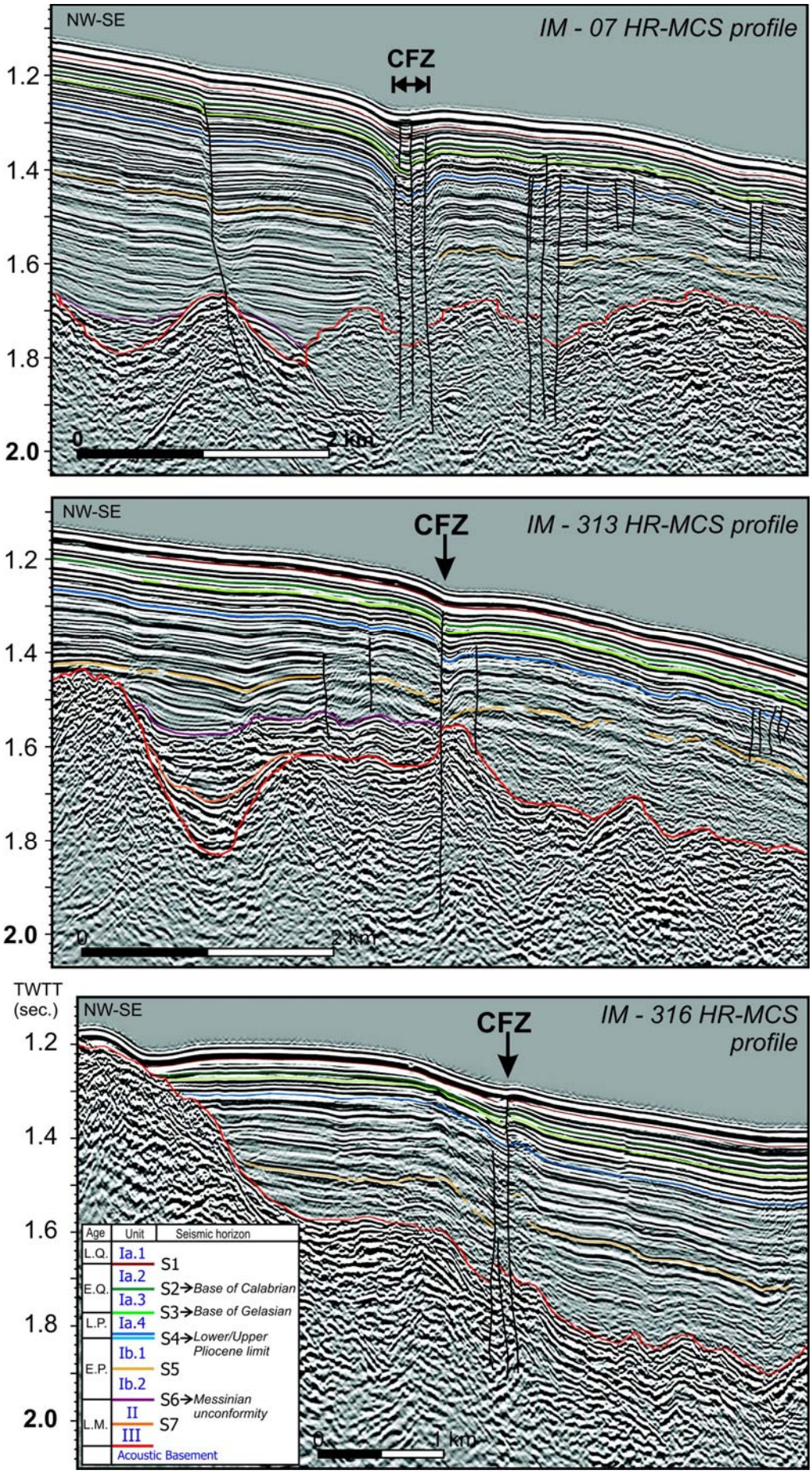
NW-SE
IM - 07 HR-MCS profile
CFZ
1.2
1.4
1.6
1.8
2.0
0
2 km
NW-SE
CFZ
IM - 313 HR-MCS profile
1.2
1.4
1.6
1.8
2.0
0
2 km
TWTT
(sec.)
NW-SE
CFZ
IM - 316 HR-MCS
profile
1.2
1.4
1.6
1.8
2.0
Age
Unit
Seismic horizon
L.Q.
Ia.1
S1
E.Q.
Ia.2
S2→Base of Calabrian
Ia.3
S3→Base of Gelasian
L.P.
Ia.4
S4→Lower/Upper Pliocene limit
E.P.
Ib.1
S5
Ib.2
S6→Messinian unconformity
L.M.
II
S7
III
Acoustic Basement
0
1 km

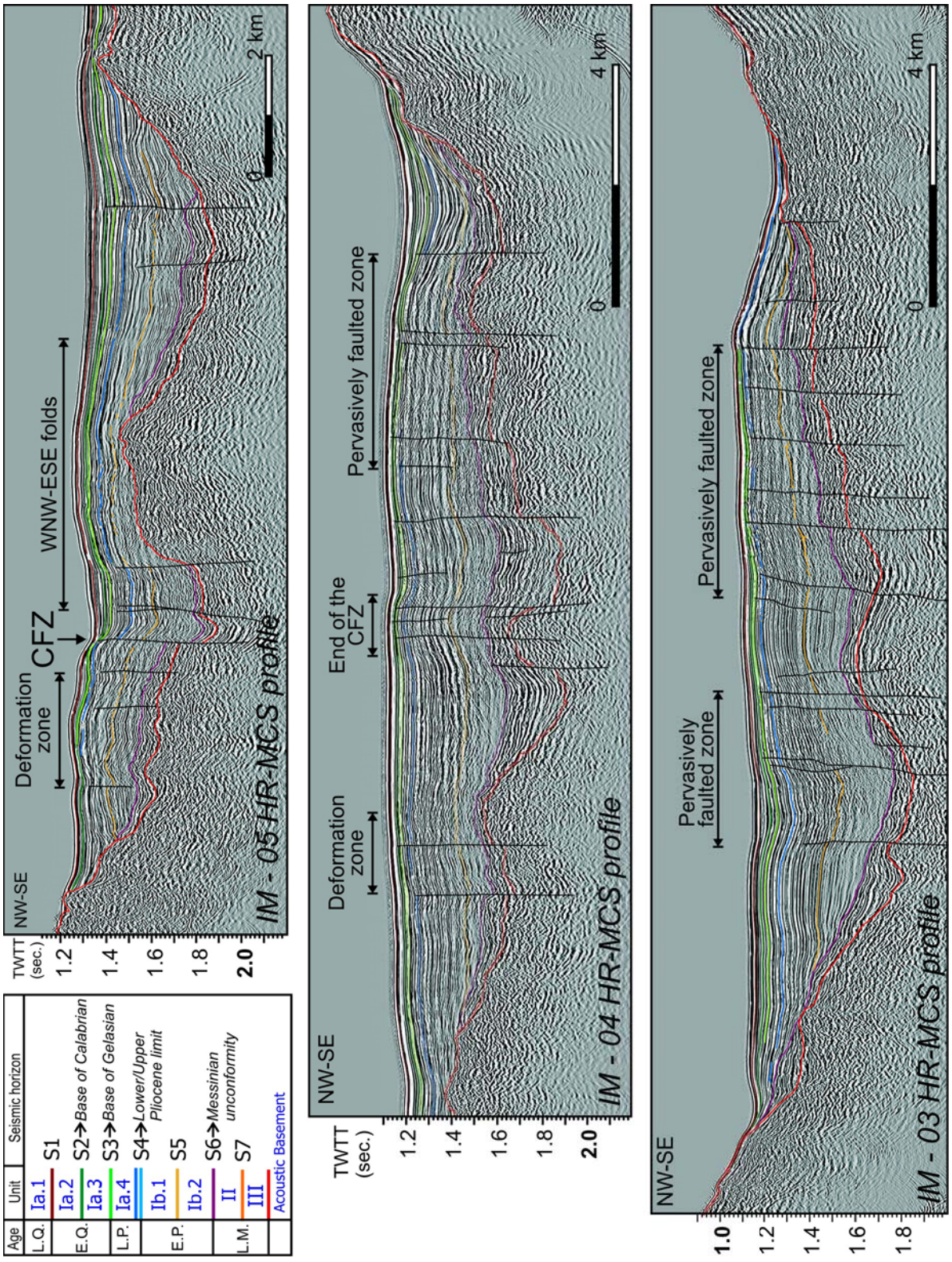
Age
Unit
Seismic horizon
L.Q.
Ia.1
S1
E.Q.
Ia.2
S2→Base of Calabrian
Ia.3
S3→Base of Gelasian
L.P.
Ia.4
S4→Lower/Upper Pliocene limit
Ib.1
E.P.
S5
Ib.2
S6→Messinian unconformity
L.M.
II
S7
III
Acoustic Basement
TWTT (sec.)
NW-SE
Deformation zone
CFZ
WNW-ESE folds
IM - 05 HR MCS profile
2 km
End of the CFZ
Pervasively faulted zone
IM - 04 HR-MCS profile
4 km
Pervasively faulted zone
IM - 03 HR-MCS profile

6.4.3. *Other CFZ-related structures in the area*

As stated above, various structures appear to be related to the southern segment of the offshore CFZ, including N110°-trending folds and a zone of pervasive faulting oriented parallel to the main N120°-trending Adra Ridge Fault (Fig. 6.21).

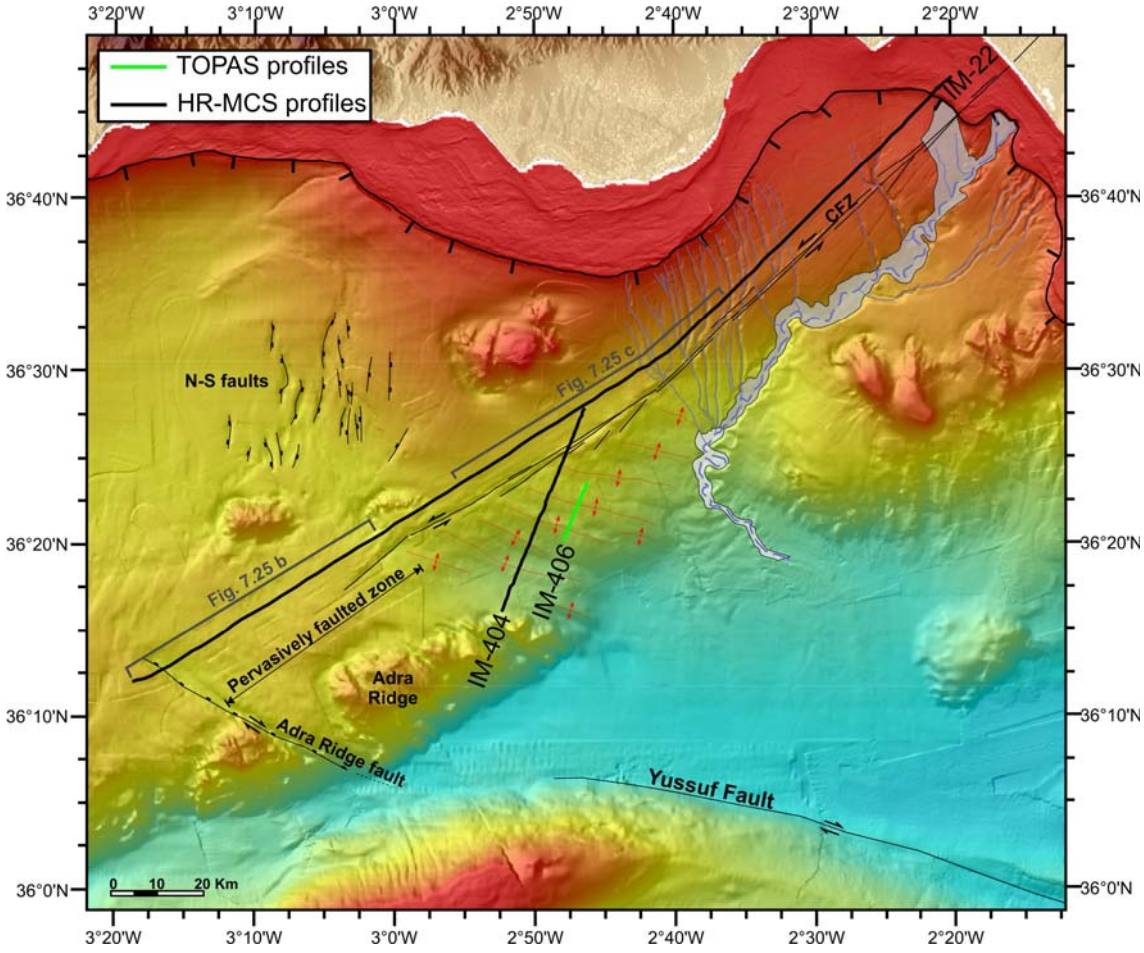

Figure 6.21. Bathymetric map and structures of the Almería margin, showing the locations of the HR-MCS and TOPAS profiles depicted in Figs 6.22 and 6.23. See Fig. 6.3 for geomorphological/tectonic legend.

Southeast of sub-segment SCF-4, the seafloor is marked by a series of undulations (folds) within a zone of 30 km wide, trending N110°. The folds are 5–15 km in length and have a wavelength of 2–3 km (Fig. 6.21). The locations of the folds are controlled by faults at depth (see the IM-404 profile in Fig. 6.22). Most of the faults show displacement at least up to the base of the Quaternary seismic units, and some displace the Late Quaternary units (just below the S1 horizon). The most recent seismic units are also folded and some faults show vertical offset up to the base of TOPAS unit II (see the IM-406 profile in Fig. 6.22), indicating recent fault activity.

To the SW, the undulations are not observed and the Adra Ridge volcanic high shows evidence of minor right-lateral displacement, apparently due to faults

trending sub-parallel to the folds. At the southern tip of the Adra Ridge, there occurs a NW–SE-trending trough, 9 km wide and 20 km long, named here the Adra Ridge Fault (ARF) (Fig. 6.21). This structure is clearly imaged in seismic profiles as a vertical fault, with a strong dip-slip component (see the SW end of the IM-22 profile in Fig. 6.23b), vertically offsetting the S7 horizon (Late Miocene) by about 0.6 s TWTT (approximately 550 m). The ARF also displaces Quaternary units, indicating recent tectonic activity. The Plio-Quaternary sedimentary units on the NE side of the fault contain growth strata, in contrast to the lower Miocene units, which maintain their thickness on both sides of the fault. These observations suggest the fault became active in the Early Pliocene. The ARF is also characterised by right-lateral strike-slip, as indicated by the lateral displacement of a 400-m-high scarp bounding the Adra Ridge to the SE, which is offset by about 5 km (Fig. 6.21).

To the NE of the ARF, the IM-22 HR-MCS profile (Fig. 6.23b) shows a pervasively faulted zone with scarce surface expression. These faults, which are densely distributed within a zone of 20 km across, represent the shear zone responsible for the minor right-lateral displacements observed on the Adra Ridge. The more densely distributed and active faults are observed immediately SW of the end of the CFZ, although deformation is observed in Pliocene units along the NW side of the SCF-6 sub-segment. These faults produce small vertical displacements, affecting up to the Quaternary unit (above the S2 horizon), with offsets of up to 8 ms TWTT (about 6.5 m) at the S3 horizon (base of the Quaternary).

6.4.4. *Basement paleo-relief*

In many of the HR-MCS profiles considered in this study, the basement surface is irregular, comprising highs and small paleo-basins (Figs 6.14, 6.15, 6.18–6.22). The dense grid of seismic profiles acquired during the IMPULS cruise (2006) along the Almería Margin enables the compilation of a contour map of the surface corresponding to the top of the acoustic basement, represented by the AB seismic horizon (Fig. 6.24). The information is represented in TWTT with sea level as a reference; thus, deformation is included and the map should not be considered a real image of the basement top. In addition, to obtain a realistic image of the relief at the time of sediment infill (Late Miocene), overprinting tectonic deformation

Following pages:

Figure 6.22. HR-MCS profile IM-404 and TOPAS IM-406 profile across the zone of N110°-trending folds. Vertical exaggeration is 5:1 for the IM-404 profile and 10:1 for the IM-406 profile, taking into account the velocity of sound in water (1500 m/s). For profile locations, see the bathymetric map in Fig. 6.21

Figure 6.23. HR-MCS IM-22 profile oriented parallel to the CFZ. Vertical exaggeration is 5:1, taking into account the velocity of sound in water (1500 m/s). For the profile location, see the bathymetric map in Fig. 6.21.

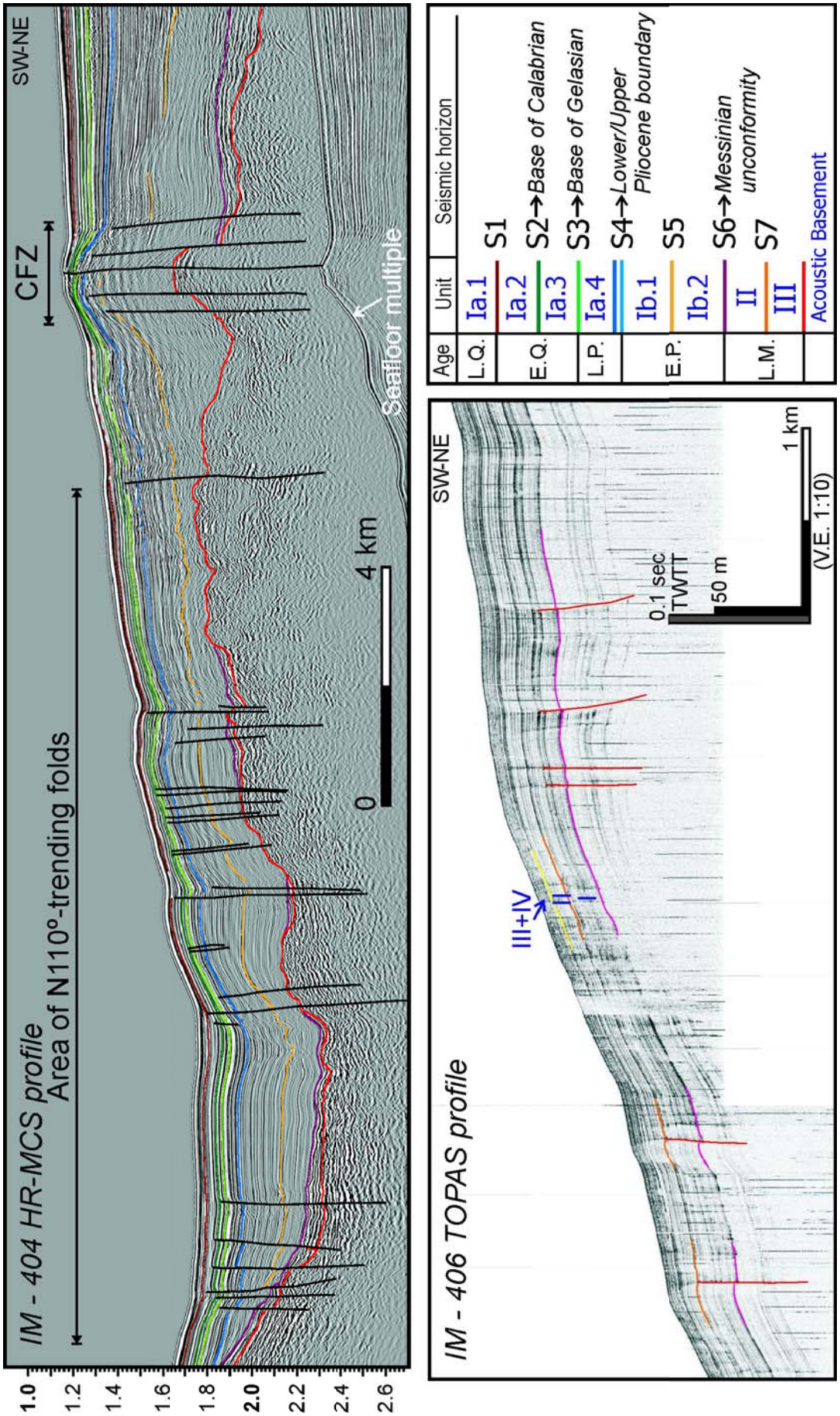
IM - 404 HR-MCS profile
Area of N110º-trending folds
SW-NE
CFZ
Seafloor multiple
0
4 km
1.0
1.2
1.4
1.6
1.8
2.0
2.2
2.4
2.6
IM - 406 TOPAS profile
SW-NE
III+IV
II
I
0.1 sec TWTT
50 m
1 km
(V.E. 1:10)
Age
Unit
Seismic horizon
L.Q.
Ia.1
S1
Ia.2
S2→Base of Calabrian
E.Q.
Ia.3
S3→Base of Gelasian
L.P.
Ia.4
S4→Lower/Upper Pliocene boundary
Ib.1
E.P.
S5
Ib.2
S6→Messinian unconformity
II
L.M.
S7
III
Acoustic Basement

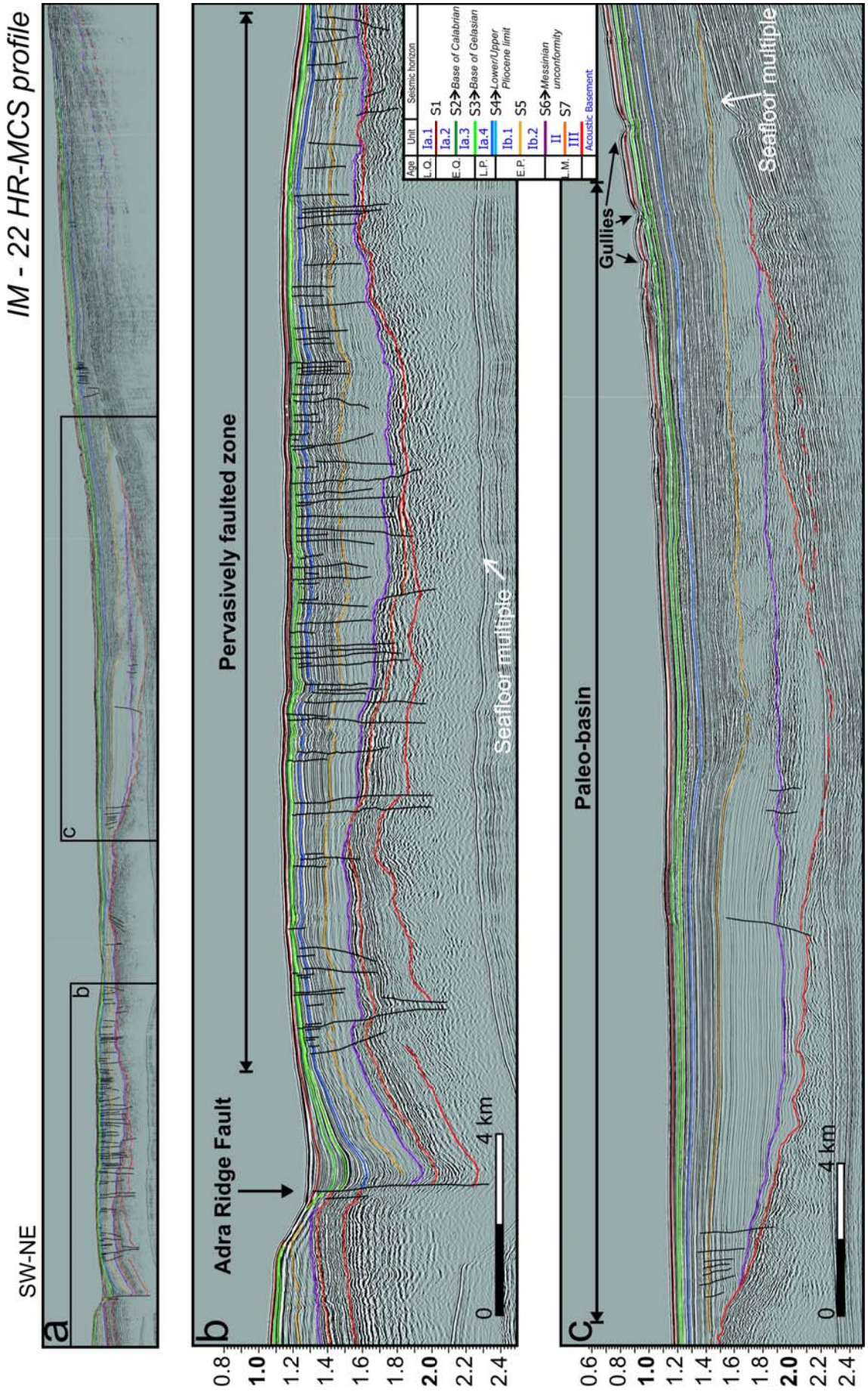
IM - 22 HR-MCS profile
SW-NE
a
b
c
Adra Ridge Fault
Pervasively faulted zone
Seafloor multiple
Paleo-basin
Gullies
Seafloor multiple
4 km
0
Age
Unit
Seismic horizon
L.Q.
Ia.1
S1
E.Q.
Ia.2
S2→Base of Calabrian
Ia.3
S3→Base of Gelasian
L.P.
Ia.4
S4→Lower/Upper Pliocene limit
E.P.
Ib.1
S5
Ib.2
S6→Messinian unconformity
L.M.
II
S7
III
Acoustic Basement
0.6
0.8
1.0
1.2
1.4
1.6
1.8
2.0
2.2
2.4

should be removed. Although the map is uncorrected and expressed in s (TWTT), it gives an indication of the basement paleo-relief and shows the simplified distribution of basement highs and paleo-valleys (Fig. 6.24).

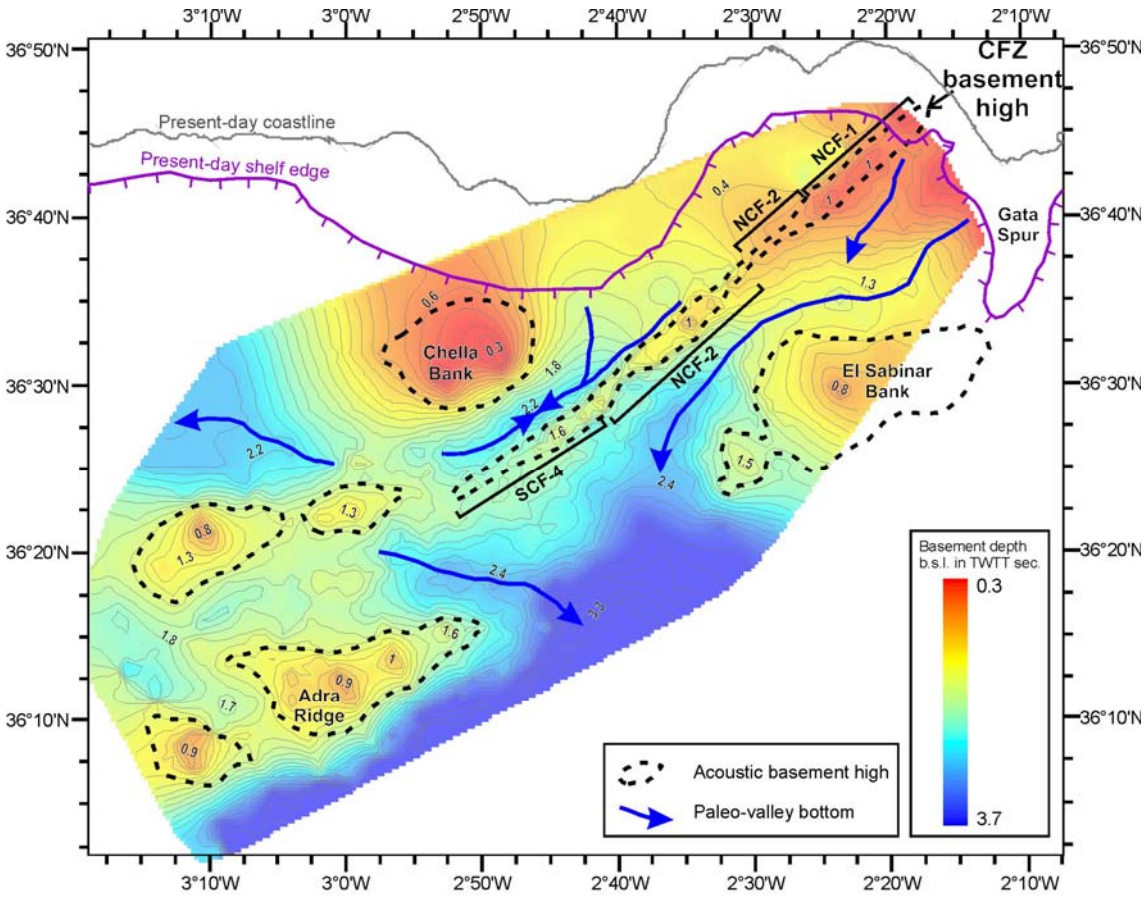

Figure 6.24. Colour contour map of the top of the basement surface in s (TWTT) below the sea level (b.s.l.), showing basement highs and the paleo-valley thalwegs.

Figure 6.24 shows a series of basement highs, most of which are elongate NE–SW. The CFZ is observed as a narrow and elongated basement high trending N050° over a distance of 65 km. This high is present along the entire NCF segment and continues southwards along the SCF-4 sub-segment. Towards the south, the elongate basement high is discontinuous.

To the SE of the CFZ, a paleo-valley is delimited by the basement highs of the El Sabinar Bank and Gata Spur, and by the fault zone itself. The head of this paleo-valley is marked by the confluence of two paleo-thalwegs: that to the NW hosts the present-day Almería Canyon, and that to the SE hosts the present-day Gata Tributary Valley System (Fig. 6.2). These observations indicate that the similar orientations of the Almería Canyon and the northern CFZ reflect the general NE–SW trend of structures in the area.

To the SE of the Chella Bank, a small and elongate NE–SW-trending paleo-basin is delimited to the south by the CFZ basement high. The depocentre of this

basin is located north of the SCF-4 sub-segment, where a present-day sag pond is located (IM-09 profile in Fig. 6.18). The IM-22 HR-MCS profile (Fig. 6.23a,c) shows this paleo-basin defined by the top of the acoustic basement, overlain by sedimentary sequences of Late Miocene age or younger. These sedimentary seismic units show lateral variations in thickness. Pliocene units (Ia.4, Ib.1 and Ib.2) define a flexure centred on the axis of the paleo-basin. Unit Ib-2 (Early Pliocene) is twice as thick in the SW as in the NE. To the SW, the lower reflectors of this unit downlap the S6 Messinian unconformity, which is an unusual feature of basin infilling, suggesting that these layers have been tilted. In contrast to the lower unit, units Ib.1 and Ia.4 are twice as thick in the NE as in the SW. Reflectors of units Ib.1 and Ia.4 at the NE part of the flexure have a relatively high amplitude and are interbedded with chaotic facies, interpreted as mass transport deposits.

The above observations indicate a change in the location of the basin depocentre during the Pliocene. The thickness distribution of unit II indicates that the basin depocentre during the Late Miocene was coincident with the actual acoustic basement depocentre (AB depocentre in Fig. 6.25). Subsequently, a tilting occurred at the beginning of the Early Pliocene, and the depocentre moved towards the SW, at the site of downlapping lower Pliocene reflections (Ib.2 depocentre in Fig. 6.25). At the end of unit Ib.2 time, during the Early Pliocene, compression produced a flexure in the Ib.2 unit, uplifting the region and displacing the depocentre towards the NE. This uplift continued throughout the Early and Late Pliocene, resulting in a gradual thickening of units in the NE relative to the SW. Moreover, the gradual uplift may explain the deposition of mass transport deposits at the base of the flexure. Although the upper Quaternary units are very thin in this region, small lateral variations in thickness can be observed by following the Ia.4 and Ib.1 patterns, indicating that uplift of the SW part of the paleo-basin continued through recent times.

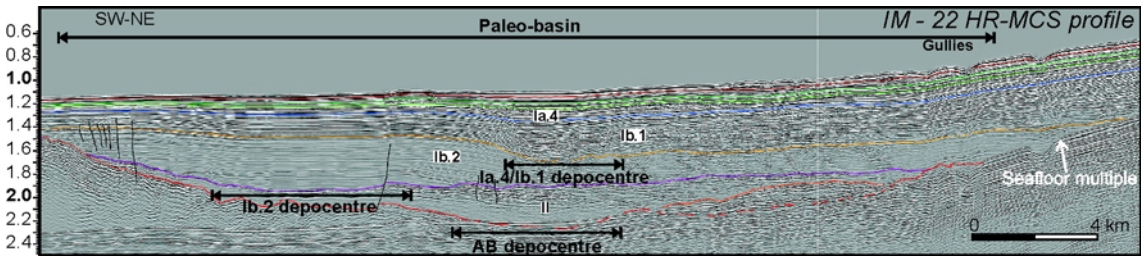

Figure 6.25. Enlargement of the IM-22 HR-MCS profile along the paleo-basin in basement. Vertical exaggeration is 5:1, taking into account the velocity of sound in water (1500 m/s). For an enlargement of the profile, see Fig. 6.23a,c; the location of the profile is shown in Fig. 6.21.

6.5. Discussion

In the preceding sections, it was shown that high-resolution seismic imaging of the Almería Margin provides insight into the tectonic architecture of the offshore CFZ and surrounding structures. The following sections discuss the implications of these findings for the Neogene evolution of the CFZ and the Almería Margin.

6.5.1. *Tectonic evolution of the offshore Carboneras Fault Zone*

The paleo-basin located south of the Chella Bank (Figs 6.24–6.26) is truncated to the south by the CFZ basement high, indicating the formation of the paleo-basin was controlled by activity within the CFZ. The oldest sedimentary unit infilling the paleo-basin corresponds to unit II (Upper Miocene; Fig. 6.23c). Moreover, in this area, the contrasting thickness of unit II on each side of the CFZ (e.g. see the IM-09 HR-MCS profile in Fig. 6.18) supports the hypothesis that during the Late Miocene, the paleo-basin was truncated to the south by a basement high. These lines of evidence suggest that the CFZ became active at least before the deposition of unit II (Late Miocene). In terms of the overlaying units, the IM-10 HR-MCS profile (Fig. 6.18) shows a bending of the seismic units towards the CFZ, with greater amounts of deformation in the oldest units, suggesting ongoing fault activity since that time.

During the Quaternary, activity upon the CFZ was concentrated within a narrow fault zone (HR-MCS profiles IM-16, IM-14, IM-12, IM-11, IM-10, IM-09 and IM-310 in Figs 6.14, 6.15 and 6.18). The CFZ was active during the Late Quaternary, as demonstrated by displacement of the most recent seismic horizons in TOPAS profiles (Figs 6.11, 6.12 and 6.17). Further discussion on the age of the faulted TOPAS units (see the following chapter) will provide insight to the most recent activity on the fault. In any case, fault traces can be observed at the seafloor, associated with surface deformation, suggesting present-day or very recent fault activity.

6.5.2. *Segmentation and evolution of the deep architecture of the offshore Carboneras Fault Zone*

In the case of long faults, it is rare that an earthquake ruptures the entire length of the fault. More commonly, one or two segments rupture during a large event (Keller and Pinter, 1996). The identification of earthquake segmentation, based on rupture behaviour during historical earthquakes, is an ideal approach for evaluating paleoseismicity and seismic hazards. Nevertheless, it is difficult to identify earthquake segments upon faults with a long recurrence interval, due to the lack of historical reports and the preservation of features related to old earthquake ruptures. In any case, it is generally agreed that faults may be segmented at a range

of scales (from a few meters to several tens of kilometres in length) (Schwartz and Sibson, 1989); consequently, structural segments are defined to better understand the nature of fault mechanics.

Along the submerged portion of the CFZ, two scales of structural segmentation are defined in the present study. First, based on bathymetric data, two morphological segments are identified based on their dominant orientation: the North Carboneras Fault (NCF) segment, trending N047°, and the South Carboneras Fault (SCF) segment, trending N059°/050°. Second, based on seismic interpretations of the uppermost 1 km below the sea floor, six structural sub-segments are identified: three along the submerged part of the NCF segment, and three along the SCF segment. The main characteristics of these segments are as follows (from north to south): NCF-1) a positive flower structure; NCF-2) a vertical fault zone forming a pressure ridge; NCF-3) a narrow vertical fault zone with uplift to the SW; SCF-4) a fault zone with prominent pressure ridges; SCF-5) a N059°-tending narrow vertical fault zone; and SCF-6) a N050°-trending narrow vertical fault zone. The segments and sub-segments are described in Table 6.2.

Table 6.2: Description of morphological segments and structural sub-segments along the offshore part of the Carboneras Fault Zone

First-order segment	Second-order segment	Location of SW tip (longitude, latitude)	Orientation (of the main fault trace)	Average	Length (km)	
Offshore North Carboneras Fault segment (NCF)	NCF-1	2°25′20″W, 36°40′45″N	N047.3°	N047°	19	51
	NCF-2	2°28′35″W, 36°38′12″N	N045.4°		7	
	NCF-3	2°41′19″W, 36°29′17″N	N046.8°		25	
South Carboneras Fault segment (SCF)	SCF-4	2°52′51″W, 36°23′14″N	N057.7°	N059°	20	39
	SCF-5	2°58′43″W, 36°20′37″N	N062.0°		10	
	SCF-6	3°03′34″W, 36°17′32″N	N050.3°	N050°	9	

It is important to emphasise the main difference between the NCF and SCF segments, apart from the difference in strike: along the NCF, the uplifted block is that to the SE, whereas along the SCF the uplifted block is that to the NW. This indicates scissor-type block rotation, as suggested by Gràcia et al. (2006), with the axis of rotation located within the SCF-4 sub-segment, which is characterised by prominent pressure ridges. This rotation mechanism also explains the partial uplift and change in depocentre location in the paleo-basin in the area south of the Chella Bank (Figs 6.24 and 6.26). Thus, the rocks located NW of the fault are rotating relatively to those SE of the fault. This observation is consistent with the multi-fractured block escape model proposed by Martínez-Díaz (1998) (Fig. 2.5), with the relative movement and tilting of the sub-blocks limited by the CFZ and the Alpujarras Fault Zone.

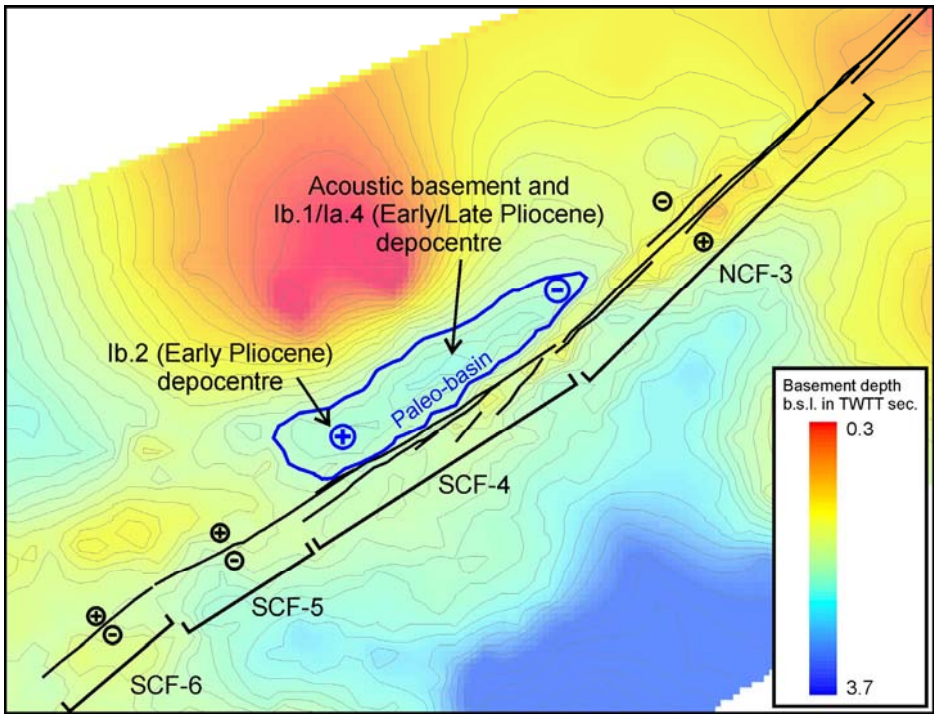

Figure 6.26. Enlargement of the acoustic basement map in Fig. 6.24, showing the location of the paleo-basin and relative uplift/subsidence of blocks on each side of the fault. Based on these data, a scissor-type rotation of the NW block is inferred (see the text for details). Colours indicate the depth to basement.

6.5.3. *Estimate of moment magnitude for the Carboneras Fault Zone segments*

Although the segments and sub-segments that make up the CFZ do not necessarily represent fracture arrest during an earthquake, they provide an idea of the variability of the architecture at depth and of the major changes that occur along the fault trace. Thus, these structural changes might somehow represent a difficulty to the transmission of the rupture, and rupture scenarios can be envisioned and the maximum magnitudes for each case estimated. The empirical relationships provided by Wells & Coppersmith (1994) enable the estimation of the moment magnitude (Mw) from the maximum rupture length (MRL), as follows:

Mw = a + b * log (SRL) where a = 5.16±0.13 and b = 1.1±0.08 are the coefficients obtained for strike-slip faults. For this equation, the standard deviation is s = 0.28 and the correlation coefficient is r = 0.91.

If considering separately the offshore portion of the NCF segment and the SCF segments, with different orientations and lengths of 51 and 39 km, respectively (Table 6.2), the maximum moment magnitudes calculated are 7.1±0.3 and 6.9±0.3, respectively. However, the shoreline does not represent a segment boundary, and further analysis of structural segmentation of the NCF offshore, together with the

onshore portion of the fault, is required. If considering the different orientations of sub-segments of the SCF segment in terms of rupture barriers, a Mw of 6.8±0.3 is obtained for the N059° sub-segment (30 km long), and 6.2±0.3 for the N050° sub-segment (9 km long). Finally, when considering all the structural sub-segments, the highest magnitude obtained is 6.7±0.3 for the NCF-1 sub-segment (25 km long), and the minimum value is 6.2±0.3 for the southern SCF-6 sub-segment (9 km long). Nevertheless, these magnitude estimates probably have little significance for paleoseismicity, as changes in the superficial architecture (i.e. uppermost kilometres below the seafloor) do not necessarily correspond to an earthquake segment boundary, which is defined at greater seismogenic depths (Schwartz and Sibson, 1989).

6.5.4. *Southern end of the Carboneras Fault Zone and strain transfer to nearby structures*

To the south of the NE–SW-trending SCF segment, two NW–SE-trending structures are observed: the Yussuf Fault and the Adra Ridge Fault (Fig. 6.21). Within the triangle defined by these three structures, deformation seems to be relatively widely distributed along smaller structures such as folds and faults, shear zones and zones of pervasive faulting. This area marks the zone of interaction among these major structures.

Interaction between areas of folding and faulting along the SCF segment

The N110°-trending fold zone observed from bathymetric data are constrained to the SE side of the N059°-trending SCF segment (sub-segments SCF-4 and SCF-5) (Fig. 6.21). In turns, these folds are controlled by NW–SE-trending active faults at depth (Fig. 6.23), suggesting a link between these structures. The NW–SE-trending faults are interpreted as a 30-km-wide shear zone, truncated to the north by the CFZ. In this framework, the folds represent a solution to the problem of accommodating deformation in the limited space between the CFZ and the shear zone.

The shear zone may be responsible for the change in orientation of the CFZ segments. To explain this proposal, Fig. 6.27 shows a model of the interaction between oblique active faults. In a simplified case (Fig. 6.27a), the NE–SW-trending fault is right-laterally offset by the NW–SE-trending faults, and further activity along the former fault results in the development of *en echelon* traces and compression between the fault step-overs. In a more complex case (Fig. 6.27b), representing the present study, the NW–SE-trending faults occur as a densely fractured shear zone. Movement upon the NW–SE-trending shear zone first displaces and rotates the surface trace of the NE–SW-trending fault. Subsequently, movement upon the NE–SW-trending fault links the *en echelon* segments, as reported by Tchalenko (1970)

from clay-cake experiments (see section 1.5 of this thesis). However, these two stages of fault activity do not necessarily occur at different times: they may occur simultaneously during the period of fault activity.

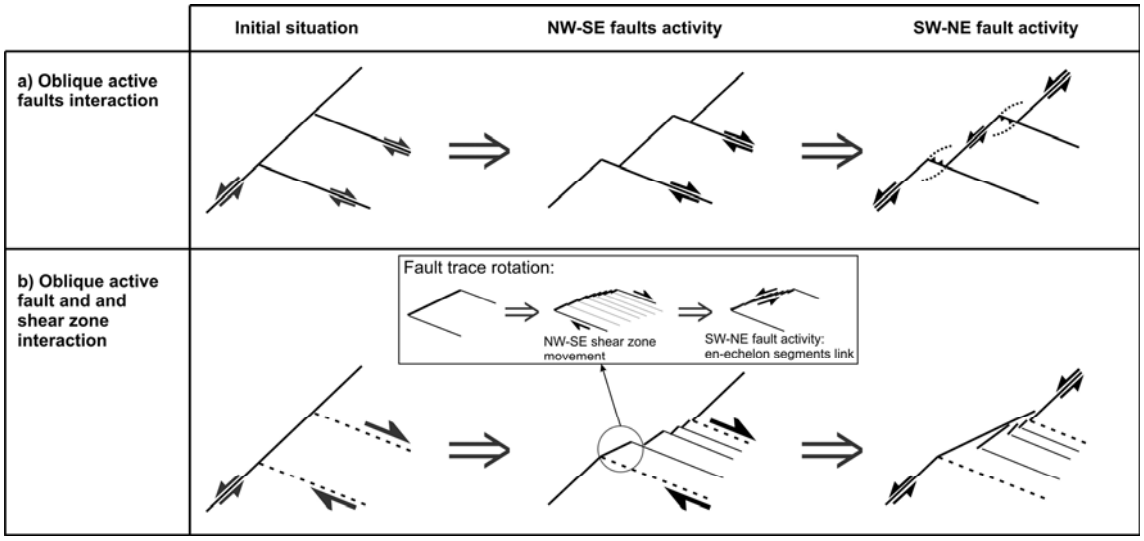

Figure 6.27. Surface structures resulting from interaction between a) oblique active faults and b) an oblique active fault and a shear zone. The second scenario would result in a change in the orientation of the CFZ segments.

Interaction between the CFZ and the NW–SE shear zone would have two main tectonic implications. First, it would produce a double change in the orientation of the CFZ trace, from N047° to N059° and then to N050°, possibly influencing earthquake segmentation, because a change in fault orientation is usually interpreted as the end of an earthquake segment (Keller and Pinter, 1996). Second, it is inferred that along sub-segment SCF-5, the regional stress field is not accommodated solely by the CFZ: some deformation occurs along the shear zone, resulting in a decrease in activity along the southern segments of the CFZ. Numerical analyses are required to confirm these interpretations.

Interactions among the Adra Ridge Fault, the pervasively faulted zone, the Yussuf Fault, and the CFZ

As the intensity of deformation decreases along the southernmost SCF sub-segment (SCF-6), the NW–SE-trending faults of the pervasively faulted zone become more intensely developed and active, suggesting a transfer of strain between these structures. The pervasively faulted zone has little bathymetric expression, although a significant deformation history is suggested by the right-lateral *en echelon* pattern clearly observed on top of the Adra Ridge (Fig. 6.21). This pervasively faulted zone ends towards the SW at the prominent Adra Ridge Fault (Fig. 6.23b), interpreted as the southern end of a 23-km-wide NW–SE-trending fault zone located WNW of the right-lateral Yussuf Fault; both structures have the same orientation and are separated

by the erosive Alboran Channel (Fig. 6.2). The fault zone is considered an extensional horsetail splay termination of the Yussuf Fault (Fig. 6.28a). In this tectonic model, the individual faults of the pervasive faulted zone would converge at depth towards the Adra Ridge Fault, partitioning the pure strike-slip motion of the Yussuf Fault into a combination of right-lateral strike-slip and extensional dip-slip over a wide area (Fig. 6.28b). Further work is required to test this hypothesis, including a detailed analysis of the new HR-MCS across the intersection between the Yussuf Fault and the Adra Ridge (captured as part of the EVENT-DEEP 2010 survey).

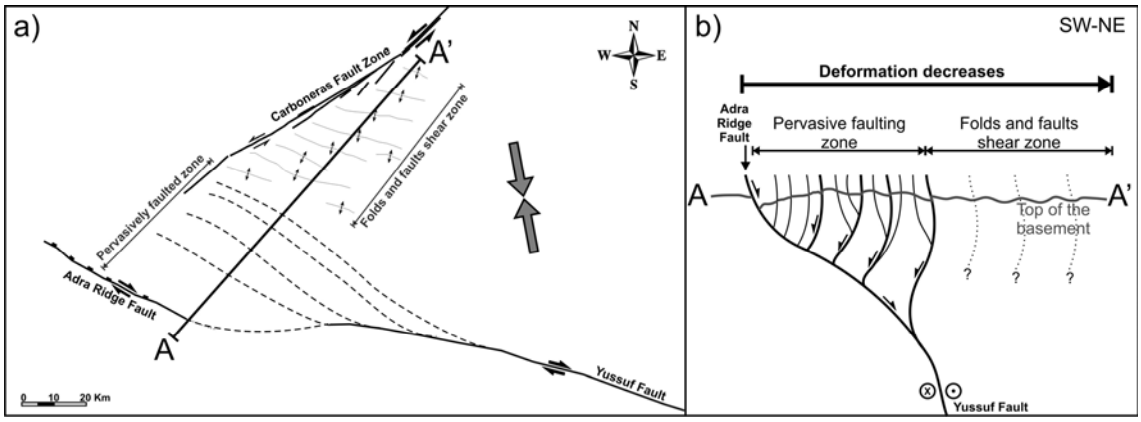

Figure 6.28. a) Schematic model interpretation of the transtensional horsetail splay termination of the Yussuf Fault, and its geometric relationship with the end of the CFZ. Grey arrows show the direction of plate convergence for the northern portion of the Trans Alboran Shear Zone (Stich et al., 2006). b) Schematic cross-section through the Yussuf Fault horsetail splay termination.

The above interpretation indicates that the southern end of the CFZ is the site of a progressive strain transfer from the NE–SW-trending left-lateral strike-slip CFZ to the NW–SE-trending structures. More precisely, the southward decrease in deformation within the CFZ could be explained by the strain being partially accommodated by the NW–SE shear zone, and by the NW–SE-trending Yussuf Fault horsetail splay.

The occurrence of growth strata in Plio-Quaternary units on the NE side of the Adra Ridge Fault, combined with the fact that the Late Miocene units are of equal thickness across the fault, suggests that the fault became active during the Early Pliocene and has been active since that time. These observations indicate a long-term minimum dip-slip rate of 0.1 mm/a. Similarly, the displaced Adra Ridge scarp along the Adra Ridge Fault suggests a right-lateral offset of 5 km since the formation of the fault, corresponding to a long-term minimum strike-slip rate of 0.9 mm/a. Given these values and its proximity to the CFZ, the Adra Ridge Fault could be considered a candidate for the AD 1522 Almería earthquake. The prominent surface relief would be in agreement with the occurrence of a tsunami associated

with this event (Martínez-Solares and Mezcua, 2002). However, the isoseismal map for the AD 1522 event, with all its uncertainties (Fig. 2.8), suggests a NE–SW-trending structure, such as the CFZ, rather than a NW–SE-trending structure, such as the Adra Ridge Fault. In any case, the scarce historical record for this event leaves many questions unanswered.

6.5.5. *Structure of the Almería Canyon and Turbidite Channel System*

Analyses of seismic profiles across the Almería Canyon indicate that it has been active, with a strong erosive pattern, since at least the Lower Pliocene, which is the age of the deeper sedimentary units observed in the seismic profiles (see profile IM-16 in Fig. 6.14). Moreover, HR-MCS profiles show that the Almería Canyon has always been located in the same place (there is no evidence of lateral migration) and that its width has increased through time. In contrast, the Almería Channel shows evidence of several migration events over time.

The similar orientation of the Almería Canyon and the CFZ has led several authors to propose the existence of a fault parallel to the CFZ and located underneath (and thereby controlling the orientation of) the canyon (e.g. Woodside and Maldonado, 1992). However, seismic profiles across the Almería Canyon and the Almería Channel show that the top of the acoustic basement below these structures has a smooth valley topography and is clearly unaffected by significant faulting (HR-MCS profiles IM-16 and IM-11 in Figs 6.14 and 6.15, respectively). Moreover, the basement contour map indicates that the similar orientation of the Almería Canyon and the CFZ is due to the general NE–SW trend of basement highs and paleo-valleys. Consequently, the new HR-MCS data demonstrate that the development of the Almería Canyon was not directly controlled by faults; thus, there are no other major faults in the study area oriented parallel to the CFZ.

6.6. Conclusions

Based on analyses of high-resolution multi-channel seismic profiles, eight seismo-stratigraphic units were identified above the acoustic basement at the Almería Margin. The ages of these units were estimated based on data from commercial wells and ODP sites. Seismostratigraphic Units II and III are of Upper Miocene age and their upper limit is marked by the S6 horizon (the Messinian unconformity). Units Ib.1 and Ib.2 are of Early Pliocene age. Unit Ia.4 is of Late Pliocene age, and the S4 horizon at its base corresponds to the Early–Late Pliocene boundary (3.6 Ma). Units Ia.1, Ia.2 and Ia.3 are of Quaternary age, as the S2 horizon (i.e. the base of Ia.2) corresponds to the Calabrian stage (1.8 Ma) and the S3 horizon (i.e. the base of Ia.3) corresponds to the Gelasian stage (2.6 Ma). In addition, four TOPAS seismic units of Late Quaternary age were identified at the Almería Margin.

Seismo-stratigraphic data indicate that the Carboneras Fault Zone (CFZ) became active during the Late Miocene or earlier, with activity continuing during the Pliocene and Quaternary. The fault zone becomes narrower in the Quaternary units, although it is active up to the Late Quaternary along the entire fault trace.

Two scales of structural segmentation were identified along the submerged portion of the CFZ. First-order segments, defined on the basis of fault trace orientation, include the N047°-trending North Carboneras Fault (NCF) segment and the N059°/050°-trending South Carboneras Fault (SCF) segment. Second-order sub-segments were differentiated according to lateral variations in fault structure within the uppermost several kilometres below the seafloor. Six structural sub-segments were defined: three along the submerged part of the NCF segment (NCF-1, NCF-2 and NCF-3) and three along the SCF segment (SCF-4, SCF-5 and SCF-6). These sub-segments are characterised by (from north to south) a positive flower structure (NCF-1); a vertical fault zone forming a pressure ridge (NCF-2); a N047°-trending, narrow, vertical fault zone (NCF-3); a fault zone with prominent pressure ridges (SCF-4); a N059°-trending, narrow, vertical fault zone (SCF-5); and a N050°-trending, narrow, vertical fault zone (SCF-6).

The NW block along the CFZ has been subjected to a scissor-type rotation, with the axis of rotation located at the SCF pressure ridge sub-segment and with relative uplift to the SW. The change in orientation of the fault trace at the SCF segment is inferred to be produced by the interaction between the CFZ and a NW–SE-trending shear zone.

The maximum magnitude of earthquakes was estimated from the length of the offshore structural segments and sub-segments, based on empirical relationships. The maximum magnitudes values range between Mw 6.2±0.3 and Mw 7.1±0.3, although further analysis is required, taking into account the onshore portion of the fault.

Towards the SW end of the CFZ, the intensity of deformation shows a steady decrease, interpreted to reflect a gradual transfer of strain to the Adra Ridge Fault and eventually to the Yussuf Fault, first through a fault shear zone and then through the pervasive faulting zone of the Yussuf Fault horsetail splay. The Adra Ridge Fault, which shows clear evidence of Quaternary tectonic activity, has a cumulative long-term minimum slip-rate of 0.9 mm/a in the right-lateral component and 0.1 mm/a in the vertical component. This fault is a candidate for producing large earthquakes and tsunamis in the area, such as the AD 1522 Almería earthquake. There are no other nearby NE–SW-trending faults oriented parallel to the CFZ at the Almería Margin.

Chapter 7: Paleoseismic study along the offshore Carboneras Fault Zone

Offset seismic reflectors observed on the multi-channel seismic (MCS) profiles enabled us to evaluate the Quaternary tectonic evolution of the Carboneras Fault Zone (CFZ). Moreover, higher resolution parametric echo-sounder systems (TOPAS) provided evidence of its Late Pleistocene-Holocene activity. Dating seismic horizons is essential for obtaining quantitative paleoseismic results of the recent fault activity, and thus, sub-seafloor samples are required. To this end, 6 gravity cores were acquired close to the fault zone (see section 3.2.2 for coring information), at sites of paleoseismic interest in line with observations of TOPAS profiles (see Table 3.2). Sedimentation rates are obtained and an age model will be proposed on the basis of dating analysis. Paleoseismic results for the offshore CFZ are obtained on the basis of chronostratigraphy together with geomorphological and stratigraphic cross-cutting relationships.

7.1. Dating key TOPAS horizons

7.1.1. Analysis of sediment cores from the Almería Margin slope

Cores recovered in the Almería Margin are distributed at two sites: A and B (Fig. 7.1). At Site A, three cores were collected: CIM1, CIM2 and M349. Core M349 is a twin core of the CIM2, which was recovered some distance from the target because of bad weather and sea conditions. Site A is located in the northern segment of the Carboneras Fault relatively proximal to the shelf break (7.5 km) with water depths ranging from 350 m (CIM1) to 440 m (CIM2). This sector probably receives the influence of the Dalías Tributary Valley System (DTVS), which conveys sediments from the shelf-edge off Campo de Dalías to the Almería Channel. TOPAS profiles (IM-101 profile in Fig. 7.1) show that Site A has flat or nearly flat highly penetrative and well-stratified facies. Mass transport deposits characterized by chaotic facies can also be observed, although these are located below the core sampling depth.

At Site B (Fig. 7.1), cores CIM3, M340 and M348 were collected. Core M340 is a twin core of the CIM3, which was recovered at some distance from the target because of bad weather and sea conditions. This site is located SE of Chella Bank, at the intersection zone between the northern and southern segments (NCF and SCF) of the Carboneras Fault Zone, approximately 15.5 km from the shelf break (distal sector), with water depths ranging from 802 m (M348) to 867 m (M340). Site B is characterized by

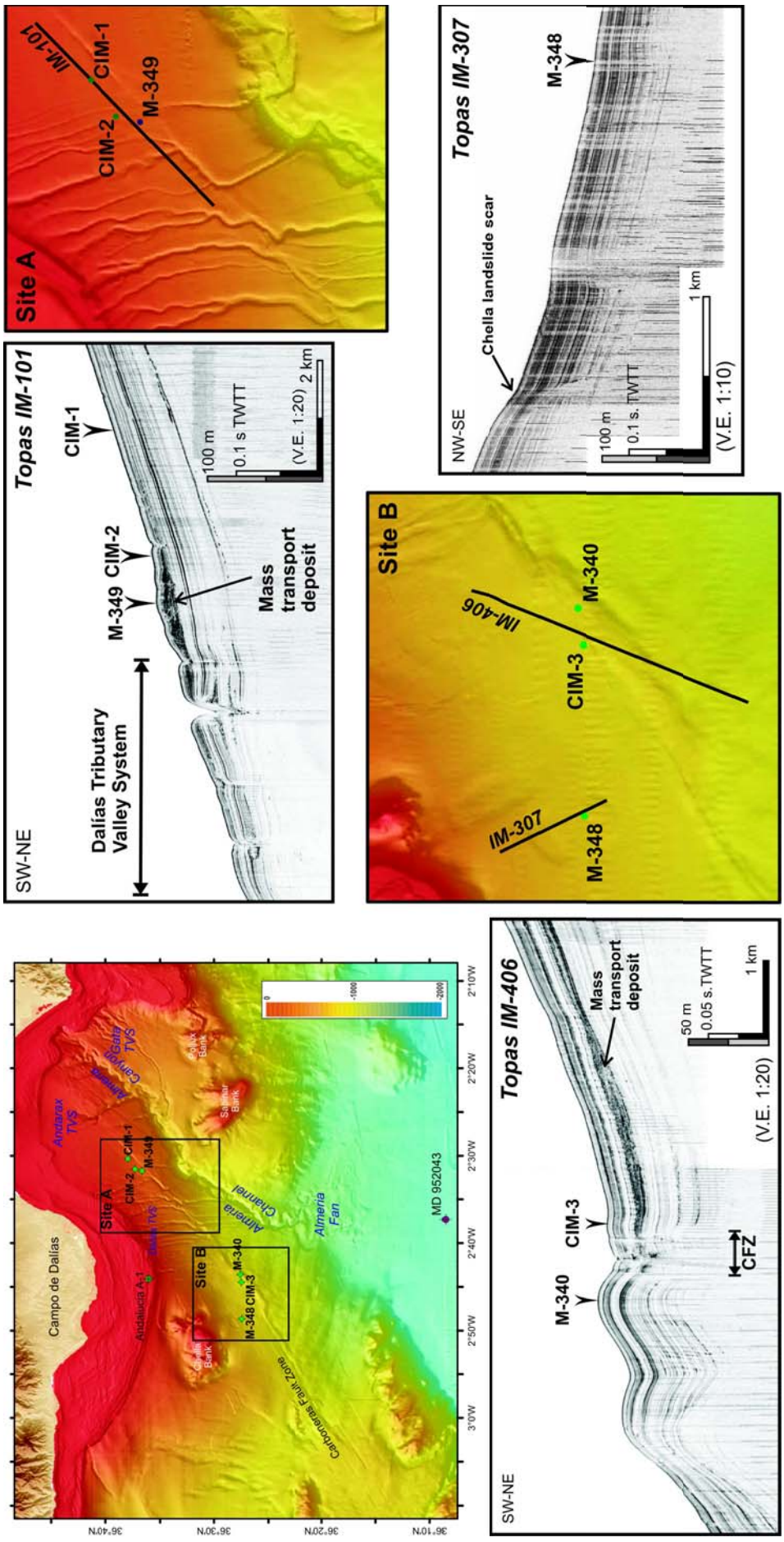

Figure 7.1. Bathymetric maps and TOPAS seismic profiles with the location of the gravity cores at the sampling Sites A and B.

highly penetrative and well-stratified acoustic facies that appears as folded and faulted reflectors in the CFZ (IM-406 profile in Fig. 7.1). Core M348 is located in the depositional zone of a small slope failure located on the SE slope of the Chella Bank, known as Chella Landslide (Fig. 6.2) (IM-307 profile in Fig. 7.1).

7.1.1.1. Sedimentary facies

Site A

Core CIM 1 (Fig. 7.2) is made up of hemipelagic facies, characterized by clayey silt. Distribution of sand ranges between 5 and 10% of the total. In the upper part of the core (0-80 cm), the appearance is homogeneous; whereas in the lower part (80-185 cm) bioturbation, faint clayed laminations and dark/light coloured sediment layering give a non homogeneous appearance. Organic-rich spots are especially abundant at the base of the core.

Core CIM2 (Fig. 7.2) is made up of hemipelagic facies characterized by clayey silt with proportions of sand of 4-16 %. Sediments are characterized by faint bioturbation and sparse shell debris; this debris is more abundant in the lower part of the core (90-173 cm) where organic-rich spots were also observed.

Core M69-349 (Fig. 7.3) is entirely constituted by hemipelagic facies made up of clayey silt with distribution of sand ranging between 7 and 17%. Sediments are characterized by faint bioturbation, scattered shell debris, isolated patches filled with very fine sand, and detached silty layers.

In general, sediments from Site A consist of olive grey to dark grey clayed silt. According to the calculated statistical parameters, grainsize classes range from fine to very fine silt (6.65 phi<M<8.0 phi), sorting is very poor (2.0 phi<SD<2.7 phi), and kurtosis is very to extremely high (2.19<K<3.97). Sediments from Site A display calcium carbonate mean values of 23% (core CIM1), 24% (core CIM2) and 26% (core M349) (Ca intensity 33600 cps). Biogenic components consist of planktonic and benthic foraminifera shells, as well as isolated fragments of sponge spicula, ostracods and echinoderms.

Site B

Core CIM3 is composed of about 120 cm of hemipelagic facies made up of silty clay with less than 6% of sand. Downcore, along interval 120-185 cm, is dominated by silty clays although with higher proportions of sand (10-18 %) and silt (24-74 %). At about 130 cmbsf clayey silts predominate. This very fine sand interval is arranged in irregular patches filled with sand and/or shell debris, and is interpreted as a sandy debrite-type mass transport deposit (MTD). The transition between hemipelagic and MTD sequences is very gradual (Fig. 7.4)

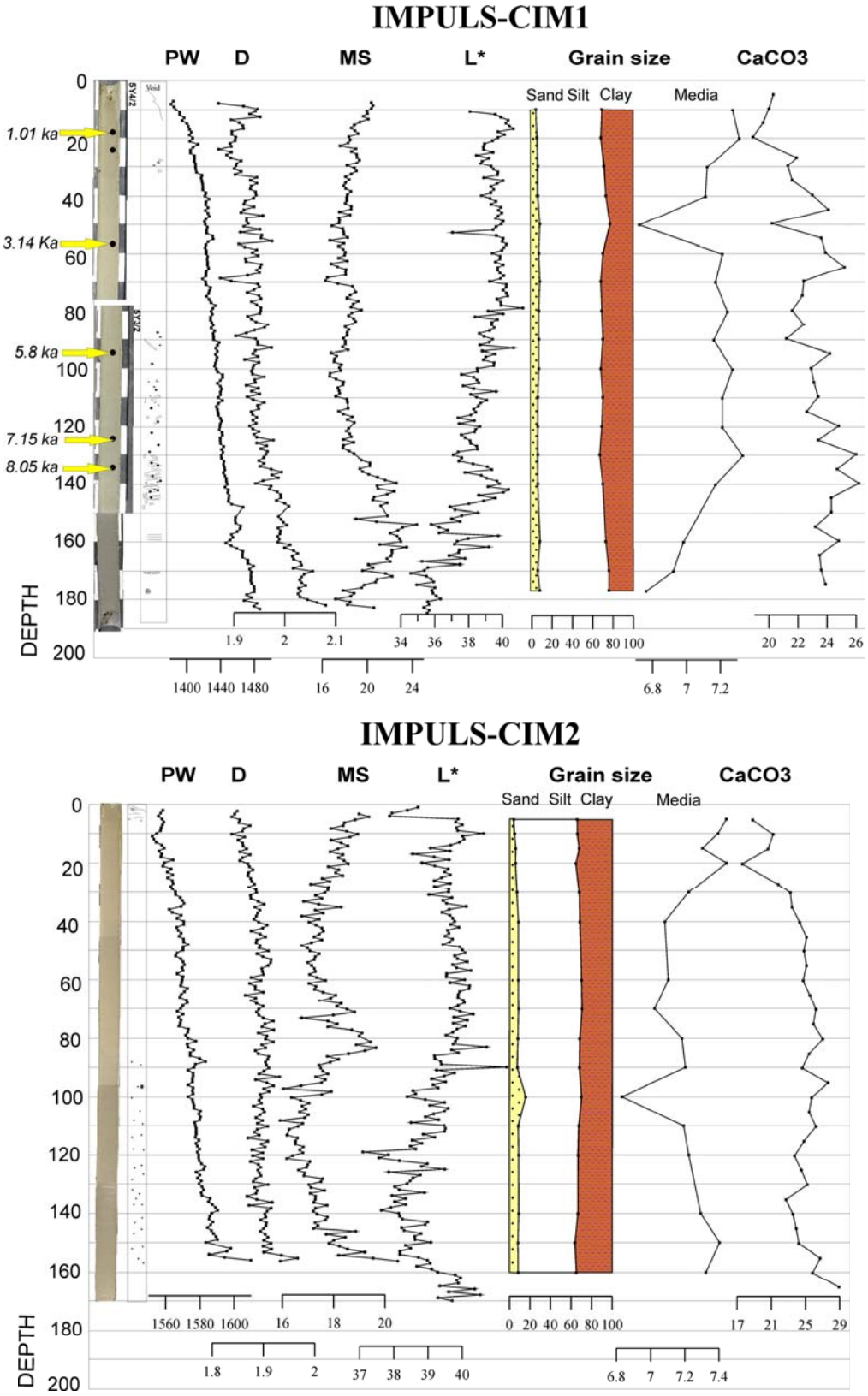

Figure 7.2. Image, structure, physical properties, carbonate and textural composition of cores CIM1 and CIM2 from Site A. Black dots correspond to ^{14}C dating samples and dating results are indicated. Depth is in cm. PW: P-wave velocity; D: Density; MS: Magnetic Susceptibility; L*: Lightness parameter.

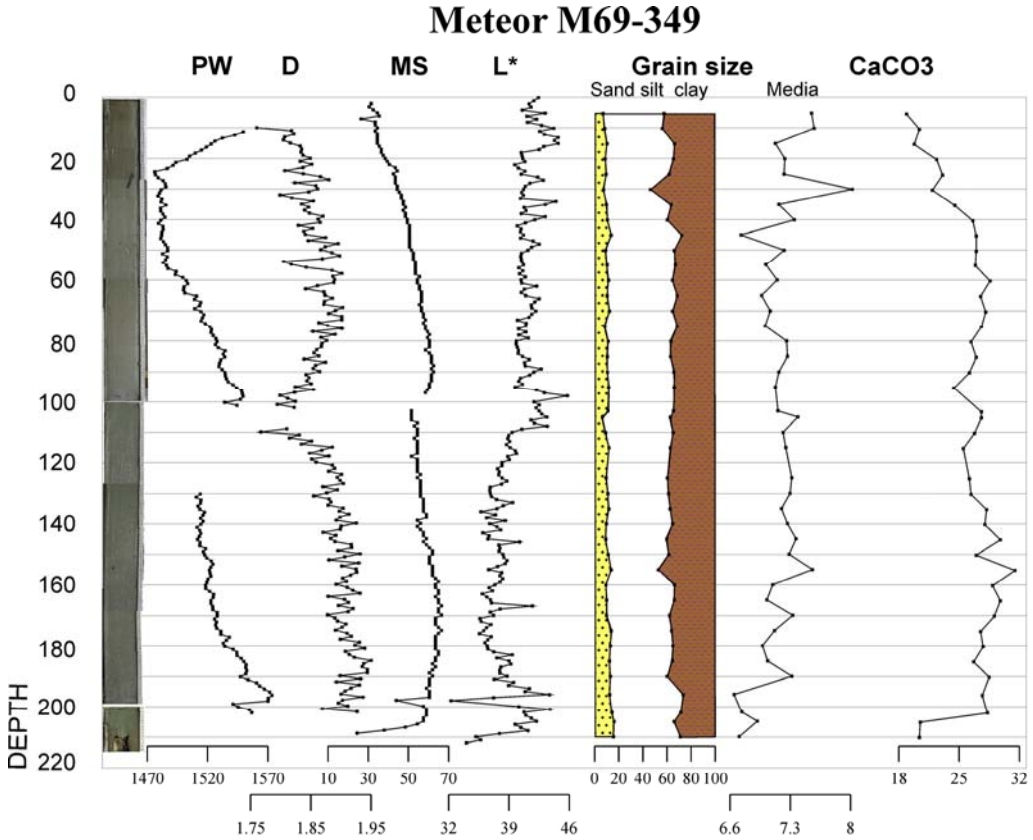

Figure 7.3. Image, physical properties, carbonate and textural composition of core M349 from Site A. Depth is in cm. PW: P-wave velocity; D: Density; MS: Magnetic Susceptibility; L*: Lightness parameter.

Core M69-340 is formed by 205 cm of hemipelagic facies made up of silty clays with sand distribution of 7-10 %. Downcore, a MTD interval ranges from 205 cm as far as the base of the core at 300 cm. Most of this interval is composed of a silty clay matrix with patches and soft clasts of sand (reaching up to 10-19 %) and small percentages of gravel (~0.1 %), which has been interpreted as a debrite deposit (Fig. 7.5).

Core M69-348 is formed from the core top down to 190 cm by silty clays with less than 7% of sand, interpreted as hemipelagites. Downcore, from 190 cm to 546 cm, is dominated by coarse size sediments, mainly clayed silts with proportions of sand ranging between 11% and 22%, corresponding to a MTD interval. Very fine sands are locally distributed in shell debris patches (debrites) or in thin layers (turbidites). Two intervals with a smaller proportion of sand (7-11%) are interbedded at 330-410 cm and 520-536 cm, which may correspond to hemipelagites or muddy turbidites. Bioturbation is intense and shell debris are abundant throughout the core (Fig. 7.5)

In general, sediments from Site B are characterized by olive grey to dark grey silty clays to clayed silts. According to the calculated statistical parameters, grainsize classes range from fine to very fine silt (6.0 phi <M<8.55 phi), sorting is poor to very poor (1.7 phi<SD<2.9 phi), kurtosis is very high to extremely high (2.19<K<6.24).

Sediments from Site B exhibit higher calcium carbonate content than those from site A, with average values of 34% in core CIM3 and 31% in core M340. Biogenic components mainly consist of planktonic and benthic foraminifera, with abundant bioclasts (i.e. bivalves and sponge spicula).

Cores from Site A are dominated by hemipelagic sediments and lack MTD layers given the texture, sedimentary structure, facies, physical properties and geochemical composition (Figs. 7.2 and 7.3). This is in agreement with the core sampling location on the slope, at some distance from the gully system (Fig. 7.1).

Site B is located in a more confined area of the slope, with the positive relief of the CFZ acting as a sedimentary barrier to the SE. The three cores acquired at this site are characterized by MTD intervals in line with the texture, sedimentary structure, facies, physical properties and geochemical composition. These MTDs correspond to: a) debrites with soft clast structures, b) thin intervals of very fine sand turbidites, and c) muddy turbidites produced by turbidity current plumes. The last MTDs are difficult to

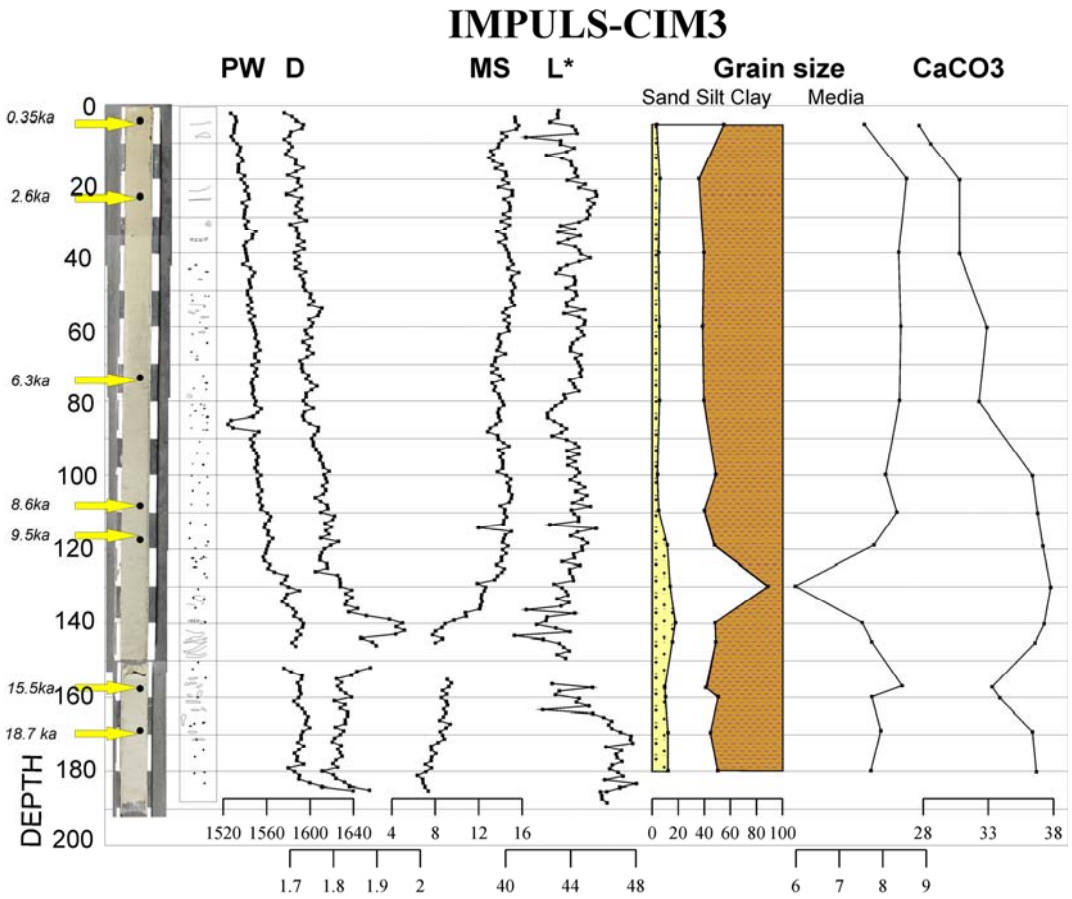

Figure 7.4. Image, structure, physical properties, carbonate and textural composition of core CIM3 from Site B. Black dots correspond to ^{14}C dating samples and dating results are indicated. Depth is in cm. PW: P-wave velocity; D: Density; MS: Magnetic Susceptibility; L*: Lightness parameter.

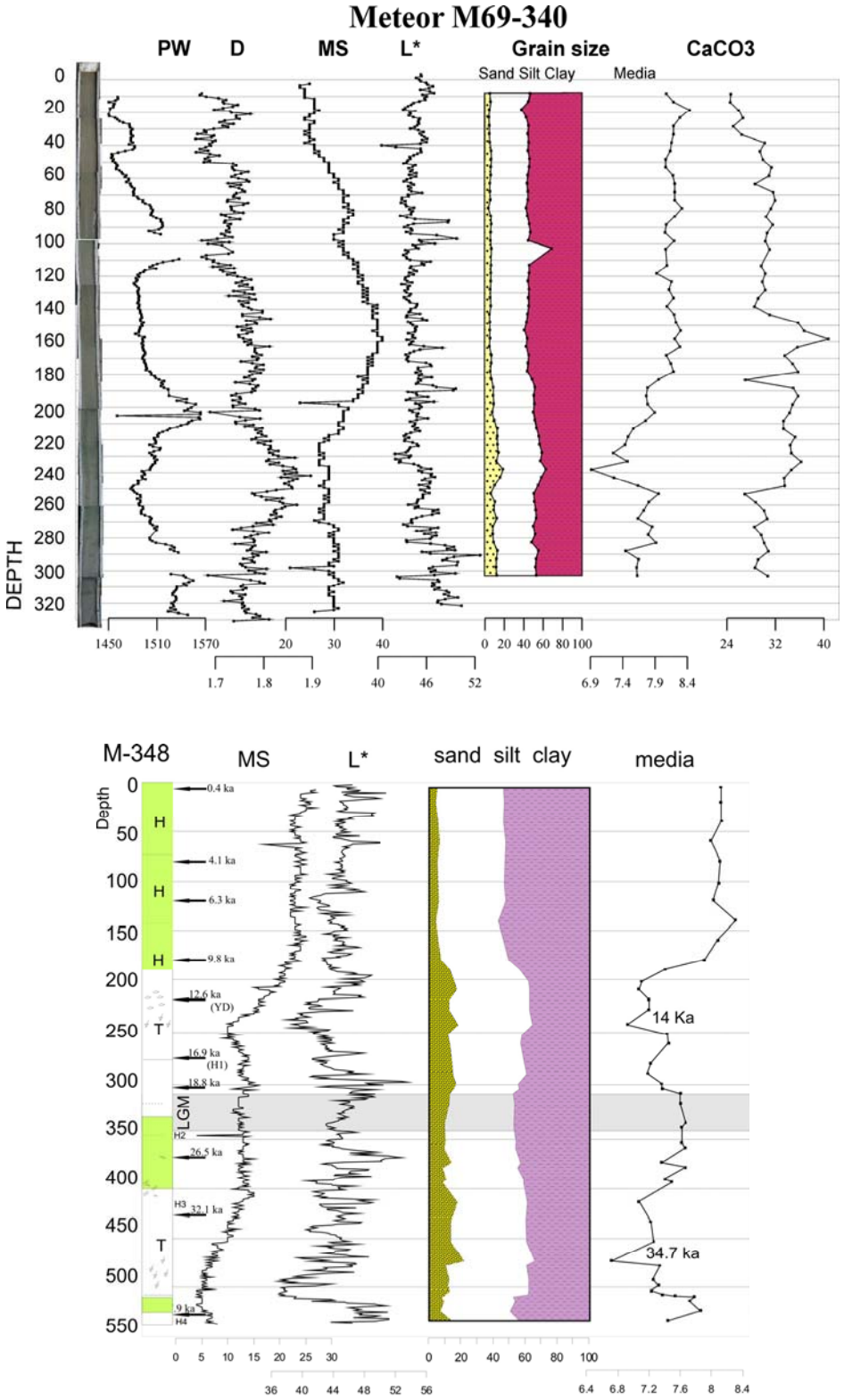

Figure 7.5. Image, structure, physical properties, carbonate and textural composition of cores M-340 and M-348 from Site B. Black arrows correspond to ^{14}C dating samples and dating results are indicated. Depth is in cm. PW: P-wave velocity; D: Density; MS: Magnetic Susceptibility; L*: Lightness parameter. P-wave velocity and Density logs for core M-348 were not acquired because of problems with the logger system.

identify in the cores from this study as they lack the typical turbidite structure with sharp erosional bases and fining upward sequences and are not linked to variations in the physical properties (i.e. magnetic susceptibility, density, P-wave velocity and lightness). The specific location of each core determines the type of sedimentary facies recorded. For instance, cores CIM3 (sag pond) and M348 (Chella slide deposit) have turbidite layers (Figs. 7.4 and 7.5) that are better defined and preserved because of their location in confined areas (Fig. 7.1). MTDs from the three cores are located in different downcore positions and cannot be correlated.

7.1.1.2. Dating analysis and sedimentation rates

In order to date the sediment cores and obtain sedimentation rates, selected planktonic foraminifera were picked from sediment samples and dated by AMS Radiocarbon in NOSAMS (USA). Radiocarbon results are listed in table 7.1. Chronostratigraphy for Site A is based on a total of 10 dating samples from cores CIM1 and M349. Core CIM2 was excluded for dating in preference to its twin core M349. Chronostratigraphy at Site B is based on 24 dating samples from the three cores: CIM3, M340 and M348.

At Site A, core CIM1 reaches the early Holocene back to 8100 Cal yr BP at 134 cm depth, whereas core M349 spans the last 9500 Cal yr BP (Table 7.1) at 180 cm depth. Holocene sedimentation rates differ little between these two cores, from 16.7 cm/kyr for core CIM1 to 19.0 cm/kyr for core M349 (Fig. 7.6 and Table 7.2).

Cores from site B extends to the Late Pleistocene. Core CIM3 was dated 18700 Cal yr BP at 168 cm depth whereas in core M340 similar ages are obtained, 18900 Cal yr BP, at almost twice the depth, at 311 cm depth (Table 7.1). Core M348 is the longest, reaching an age of 37900 Cal yr BP at 535 cm depth. Changes in sedimentation rates are observed along these cores, especially in core CIM3 decreasing from 12.4 cm/kyr for the Holocene to 3 cm/kyr for the 11200-19000 Cal yr BP period (Fig. 7.6 and Table 7.2). Cores M340 and M348 present similar sedimentation rates for the Holocene (18.0 cm/ka and 18.4 cm/kyr respectively) and for the 11200-19000 Cal yr BP (14.1 cm/kyr and 14.5 cm/kyr respectively). Moreover, in core M348 sedimentation rates of 9.4 cm/kyr for the 19000-32000 Cal yr BP period, and 17.2 cm/kyr for the 32000-38500 Cal yr BP period were calculated, suggesting a mean value of 12.4 cm/kyr for the Late Pleistocene sampled sediments.

In general, sedimentation rates calculated from the RV Meteor cores (M340, M348 and M349) are higher than those calculated for the IMPULS cores from the RV Hesperides (CIM1 and CIM2) (Fig. 7.6 and Table 7.2). This may be attributed to several factors: a) different coring systems (i.e. compressing or expanding the cored sediment); b) the fact that the vessel is equipped with dynamic positioning (DP), which prevents movement during the coring operation; and c) different weather conditions at

the time of sampling. In the case of the RV Meteor cores (M340, M348 and M349), as the cores were longer, weather conditions were optimal and the vessel was equipped with DP, the resulting sediment cores are of better quality than the ones acquired with the RV Hesperides. Thus, in order to have more consistent results, sedimentation rates from Meteor cores will be used for further analyses.

Table 7.1: Radiocarbon dates and calibrated calendar ages of samples from Sites A and B. AMS code corresponds to the NOSAMS Laboratory (WHOI, USA) reference number for each date. Pfs: Planktonic foraminifera species used are Globorotalia inflata (1), Globigerina bulloides (2), Neogloboquadrina pachyderma (3) and Globigerinoides ruber (4). Calendar ages correspond to δ 1 value obtained with OxCal 4.1 calibration software. The ΔR used is the one from Malaga -22 +/-35 ^{14}C yr.

Site	Core	Depth (cm)	AMS code	Pfs	^{14}C Yr	Error ±	Calendar Yr BP	Error ±
A	**CIM 1**	17-18.5	60679	1	1470	35	**1035**	**65**
		56-57,5	60680	1	3300	35	**3177.5**	**78.5**
		94-95,5	60681	1	5420	80	**5810**	**97**
		124-125,5	60682	1	6610	50	**7168.5**	**76.5**
		134-135,5	60683	4	7590	50	**8074**	**69**
	M69/1 349	50	62881	1	2640	25	**2356**	**56**
		80	62882	1	3960	30	**3988.5**	**72.5**
		105	62883	1	4910	35	**5260**	**123**
		150	62884	1	6900	30	**7438.5**	**45.5**
		180	62885	3	8770	35	**9466**	**41**
B	**CIM 3**	3-4.5	60684	1	715	30	**373.5**	**54.5**
		25-26.5	60685	1	2860	35	**2663**	**68**
		75-76.5	60686	1	5870	40	**6318**	**55**
		107.5-109	60687	4	8170	40	**8681.5**	**95.5**
		117-118.5	60688	4	8790	45	**9477.5**	**45.5**
		158-159.5	60689	2	13500	75	**15500**	**190**
		167.5-169	60690	3	15700	80	**18702.5**	**72.5**
	M69/1 340	3	62887	1	490	25	**156**	**76**
		63	62888	1	3390	25	**3292**	**55**
		123	62889	1	6090	35	**6545**	**66**
		163	65160	3	8450	40	**9081.5**	**78.5**
		203	62891	3	10250	65	**11256**	**80**
		263	62892	2+3	13700	60	**15792.5**	**195.5**
		311	62893	3	16050	70	**18909**	**59**
	M69/1 348	5	65161	1	740	35	**397**	**63**
		80	65162	1	4100	40	**4174**	**86**
		120	65163	1	5920	40	**6346.5**	**55.5**
		180	65164	3	9060	55	**9797**	**127**
		220	65165	3	11000	50	**12604.5**	**185.5**
		280	65166	3	14550	80	**16902**	**225**
		310	65167	3	15900	70	**18824.5**	**62.5**
		380	65169	2	22000	120	**26468**	**171**
		435	65170	3	26800	130	**32093**	**206**
		535	65171	3	32500	220	**37896**	**268**

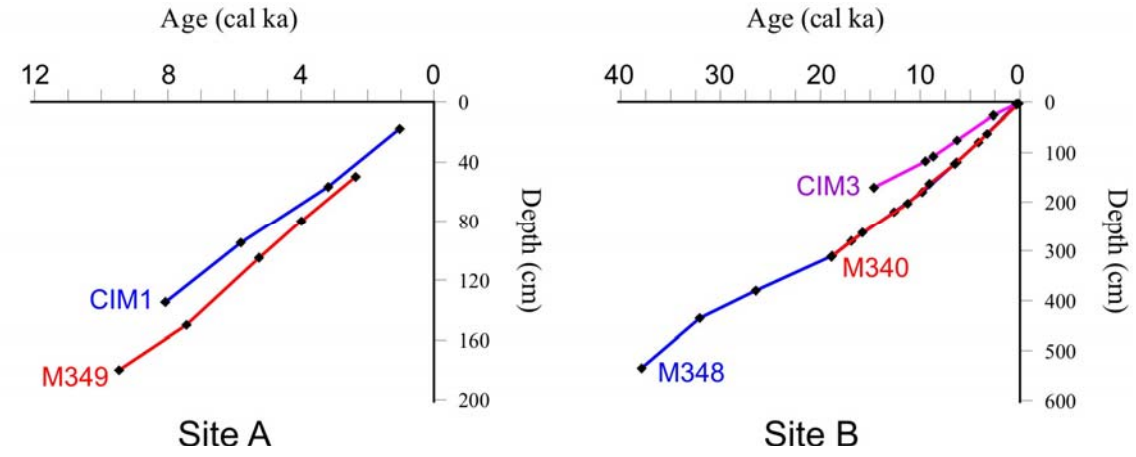

Figure 7.6. Sedimentation rates (cm/ka) of sediment cores from Sites A and B located on the Almería Margin slope.

Table 7.2: Summary of the average sedimentation rates (in cm/ka) calculated for cores at Sites A and B on the Almería Margin slope.

SITE	CORES	AVERAGE SEDIMENTATION RATES (cm/ka)			
		0-11.2Ka BP	*11.2-19Ka BP*	*19-32Ka BP*	*32-38.5Ka BP*
A	CIM1	16.8			
	M349	19.0			
B	CIM3	12.4	3		
	M340	18.0	14.1		
	M348	18.4	14.5	9.8	17.2

Sedimentation rates obtained at Sites A and B from the Almería Margin slope show higher values for the Holocene than for the Upper Pleistocene. These sedimentation rates contrast with those of other studies of the Almería canyon and turbidite channel system (Bozzano et al., 2009) and Alboran Sea (Jimenez-Espejo et al., 2008). For example, Bozzano et al. (2009) found values of 10-11 cm/ka for the Holocene and 20 cm/ka for the Pleistocene at the base of the Almería turbidite system. One explanation could be that cores from our study are located at shallow depth (350-867 m deep) whereas the cores from the aforementioned works are from deeper environments (1275-1650 m, Bozzano et al., 2009) (1869-2382 m, Jimenez-Espejo et al., 2008), and thus a change in the sedimentation pattern for the Holocene could account for the misfit. Nevertheless, a detailed study on this subject is recommended.

7.1.2. Age model for the TOPAS seismostratigraphic units

As already described in Chapter 6, the uppermost units (I-IV) identified in the TOPAS profiles from the Almería Margin were described as an alternation of transparent/semi-transparent and well-stratified facies. This alternation between semi-transparent and parallel bedded facies in the uppermost metres below seafloor is

interpreted as a succession of periods dominated by high-energy processes (units I and III) and low-energy processes (units II and IV), respectively (García et al., 2006). High-energy processes are dominated by turbidity currents that create a succession of turbidite layers between hemipelagic sequences. In contrast, low-energy periods mainly accumulate hemipelagic sediments producing the characteristic semi-transparent facies with uniform thickness mimicking the pre-existing morphology ("draping"). García et al. (2006) tentatively date the bottom of each TOPAS unit based on sedimentation rates from paleoceanographic studies in the Alboran Sea (i.e. Cacho et al., (1999) (Fig. 6.7). These authors use sedimentation rates from the CALYPSO giant piston core MD95-2043 located in the deeper parts of the Eastern Alboran Basin (Fig. 7.1), whose values vary considerably with respect to the values from the slope (e.g. 40 cm/ka for the Holocene from the deep basin after Cacho et al. (1999) to 11 cm/ka in the Almería turbidite system after Bozzano et al. (2009)). These large variations correspond not only to the different location (base of the slope and slope respectively) but also to the different acquisition systems (piston cores tend to extend the sediments whereas gravity cores tend to compress them). Thus, the ages of the TOPAS units from the Almería Margin are revised here in line with the results from cores sampled in the slope correlated with our TOPAS profiles acquired at the sampling sites. This new chronostratigraphy is subsequently linked to Marine Isotopic Stages (MIS) boundary ages, and the variability in the Almería Margin TOPAS units will be correlated with climatic stages.

7.1.2.1. Proposed ages for TOPAS units based on local sedimentation rates

The longest core acquired on the Almería Margin slope (core M-348, 5.57 m long) was used to estimate the ages of the base of each TOPAS unit. The ages obtained along core M-348 were projected on the IM-307 TOPAS profile by applying a sound propagation velocity in the upper sediments of 1600 m/s. In figure 7.7, the base of the Holocene, represented by a red dot, is estimated to be at 2.1 m depth by using the 18.4 cm/ka sedimentation rate calculated for this period (Table 7.2). The bottom of the core, depicted by a green dot, is estimated to be at 38.5 ka BP on the basis of the sedimentation rate at the base of the core. From there, the age of the base of subsequent TOPAS units was estimated by applying the average value of 12.4 cm/ka for the Late Pleistocene. Thus, the base of unit IV would correspond to 31.1 ka BP, the base of unit III to 92.8 ka BP, the base of unit III to 120.5 ka BP and the base of unit I to 197.8 ka BP (Fig. 7.7).

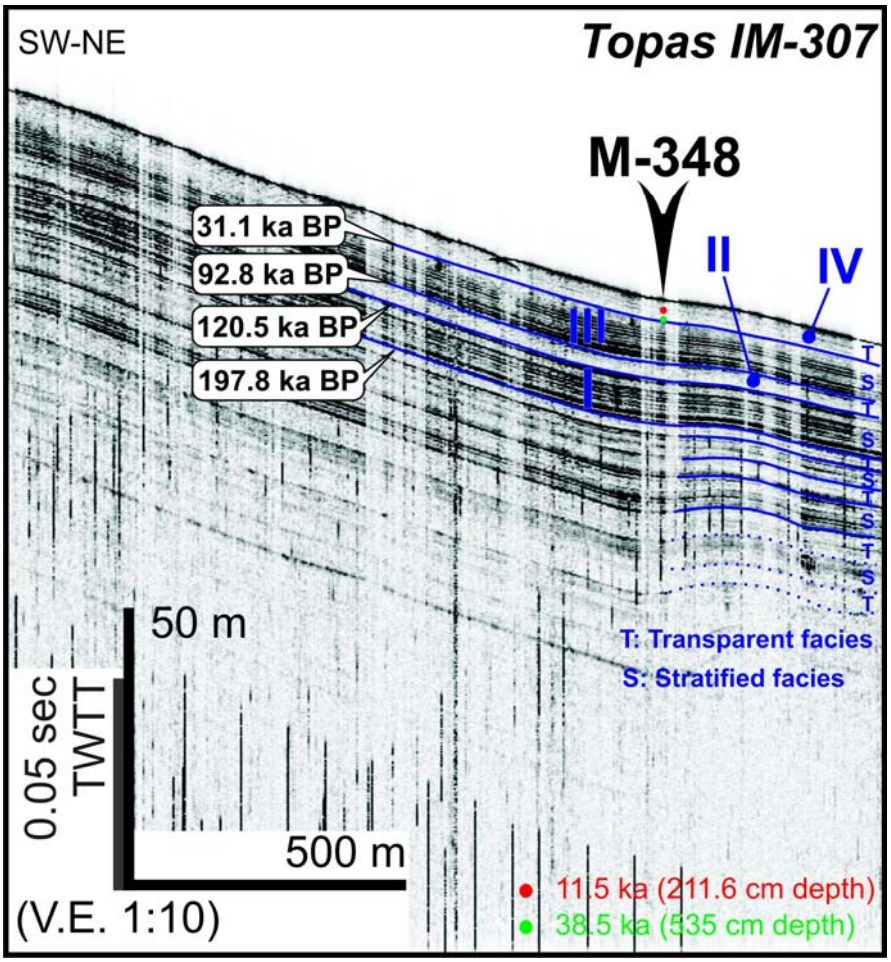

Figure 7.7. TOPAS IM-307 profile running along the M348 coring site. Tentative ages of the base of each TOPAS unit are calculated from sedimentation rates obtained from the M348 core: 18.4 cm/ka for the Holocene and an average value of 12.4 cm/ka for the Upper Pleistocene, and applying a sound velocity propagation in the upper sediments of 1600 m/s. The red dot depicts the estimated depth of the base of the Holocene period in the M348 core. The green dot represents the bottom of the M348 core. Vertical scale in m is calculated by applying a sound velocity propagation in the water of 1500 m/s. See location in Fig. 7.1. V.E.: Vertical exaggeration.

7.1.2.2. Correlation between TOPAS seismic units and climatic variability

Assigning an age to a key horizon based on core sedimentation rates is a first approximation. However, since core sampling is limited to a few metres depth, we extrapolated downwards the results obtained in the uppermost meters to calculate the age of the deeper seismic horizons. It is well known that sedimentation rates are not constant downcore with the result that this method could lead to errors of thousands of years in the unit ages.

According to the hypothesis that parallel bedded facies are generated during high-energy processes and that semi-transparent facies are formed by low-energy processes (e.g. García et al., 2006), well-stratified units (I and III) should be associated

with low sea-level periods (lowstands) or even Marine Isotopic Stages (MIS), and semi-transparent units (II and IV) with high sea-level periods (highstands) or odd MIS. Ages calculated by core M348 sedimentation rates are tentatively correlated with MIS boundary ages (Table 7.3) following the benthic $d^{18}O$ standardized isotopic curve of Lisiekci and Raymo (2005; 2009). Well stratified unit I is estimated to have been deposited during the cold MIS 6, its base being at 191 ka BP. Semi-transparent unit II is assumed to have been deposited during the warm MIS 5, its base being at 130 ka BP. Well stratified unit III is estimated to have been deposited during cold stages MIS 2-4 (MIS 3 is a moderate warm stage and usually not well represented in the sedimentary record), its base being at 71 ka BP. Following the same argument, semi-transparent unit IV would have been deposited during MIS 1-2. However, as the base of unit IV corresponds to the bottom of the M348 core (Fig. 7.7), the age of 31.1 ka BP was selected for this unit.

In the Almería Margin, the base of each semi-transparent unit is often limited by a characteristic high-amplitude positive (black) reflector, followed throughout the area (Fig. 7.7). These strong reflectors are interpreted to represent the sharp climate variations from cold to warm stages, known as terminations (Lisiecki and Raymo, 2009).

Table 7.3: Tentative correlation between calculated ages for the base of each unit based on a gravity core sedimentation rates and boundary ages of Marine Isotopic Stages (MIS). Final ages proposed for the base of each TOPAS unit are represented in bold.

TOPAS seismic unit	Estimated age from core sedimentation rates		MIS boundary ages	MIS stages
				MIS 1
Unit IV →	**31.1 ka BP**		14 ka BP ←	
				MIS 2-4
Unit III →	92.8 ka BP	~	**71 ka BP** ←	
				MIS 5
Unit II →	120.5 ka BP	~	**130 ka BP** ←	
				MIS 6
Unit I →	197.8 ka BP	~	**191 ka BP** ←	

7.2. Morphological and stratigraphic evidence of recent tectonic activity

Morphological and stratigraphic evidence of the Quaternary tectonic activity along the offshore part of the Carboneras Fault is well represented by fault scarps, pressure ridges and flower structures observed on bathymetry, HR-MCS and TOPAS profiles all along the fault trace. These structures have been fully described in Chapter 6 (Figs. 6.12-6.22) and will be analysed from a paleoseismic point of view in the following section (7.3.2).

As already discussed in the previous chapter, the CFZ is responsible for the sharp course deflection of the gullies of the Dalías Tributary Valley System (DTVS) (Fig. 7.8a). Most of the gullies are deflected for more than 2 km towards the SW when intersecting the uplifted SE block of the North Carboneras Fault (NCF) segment. Taking into account the left-lateral motion of the fault, we rule out the possibility that a fault offset is responsible for the present-day distribution of the gullies.

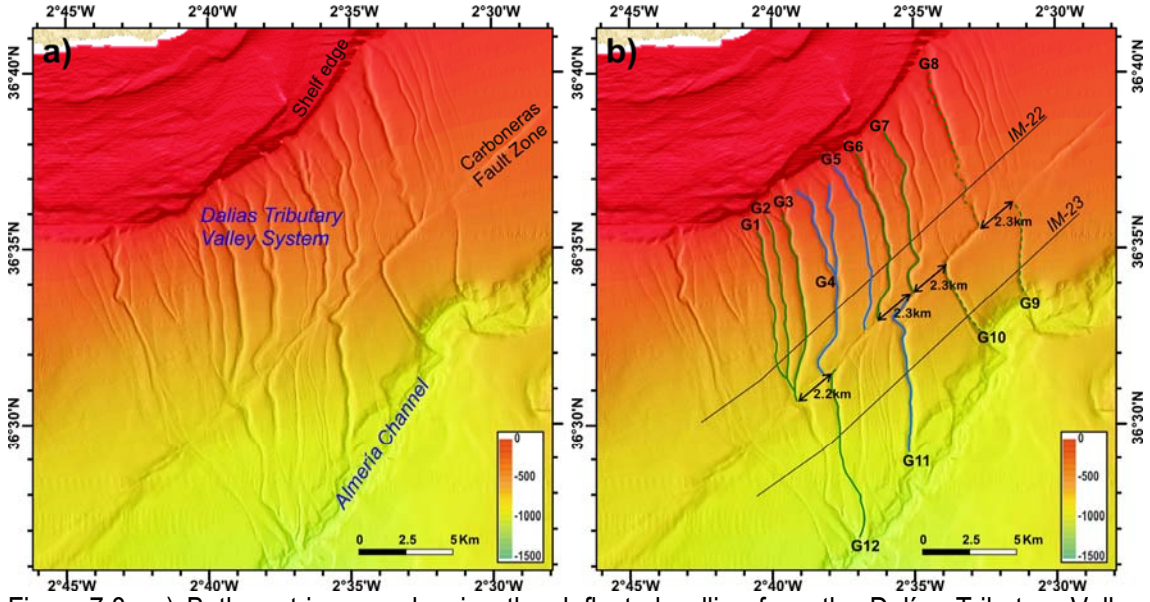

Figure 7.8. a) Bathymetric map showing the deflected gullies from the Dalías Tributary Valley System along the Northern Carboneras Fault segment. b) Same map where the HR-MCS IM-22 and IM-23 profiles presented in Fig. 7.9 are located. Colour of gullies depends on the degree of incision in the bathymetry and HR-MCS. Thus, green gullies started to be active above the S2 horizon and blue gullies started above the S4 horizon.

García et al. (2006) studied the sedimentary architecture of the DTVS of the Almería Canyon and observed that gullies show no lateral migration in the TOPAS profiles. Moreover, these authors observed that most of the valleys show an upward evolution from channels to gullies, as suggested by the presence of levees in the sub-bottom layers and the absence of these near the seafloor.

In order to link the gullies located on both sides of the fault trace, HR-MCS profiles running across the gullies and parallel to the fault zone were acquired during the IMPULS cruise: the IM-22 profile runs 2 km to the north of the CFZ and the IM-23 profile runs 3 km to the south of the CFZ (Fig. 7.8b and 7.9). Channel-levee structures are observed in the Plio-Quaternary reflectors along profiles IM-22 and IM-23 and are indicated by a yellow arrow in Fig. 7.9. The orange arrow indicates chaotic reflections interpreted as a channel infill deposit.

Three generations of gullies are inferred from the analysis of sedimentary features observed in the seismic profiles. Gullies from the first (oldest) generation (G4, G5 and G11 indicated by a blue arrow in Fig. 7.9) show channel-levee structures just below the S3 seismic horizon, and thus they were formed during the Upper Pliocene. Gullies from the second generation (G1, G2, G3, G6, G7, and G12 indicated by a continuous green arrow in Fig. 7.9) show features above the S2 seismic horizon, and are therefore younger than 1.8 Ma. The third (youngest) generation of gullies is observed on surface with small incisions (Fig. 7.9) and usually does not present sedimentary features on the HR-MCS lines, or presents features above the S1 horizon, such as the southwestern gully from the IM-23 profile (Fig. 7.9), suggesting a Late Quaternary age. Gullies G9 and G10 do not show sedimentary features below the seafloor, probably because of its strong erosive character (Fig. 7.9), represented by discontinuous reflections observed above the S2 seismic horizon. Although the erosion could be more recent than the formation of the second generation of gullies, it is unlikely that these gullies belong to the third generation as they are characterized by a pattern of little incision. Thus, these gullies (G9 and G10), indicated by green dashed lines, could be part of the second generation (<1.8 Ma). Likewise, gully G8 does not show levee structures but a chaotic, channel-filling facies between the S2 and S1 seismic horizons. This was ascribed to a second gully generation as it is unlikely that the first generation eroded down to this level and filled it up again.

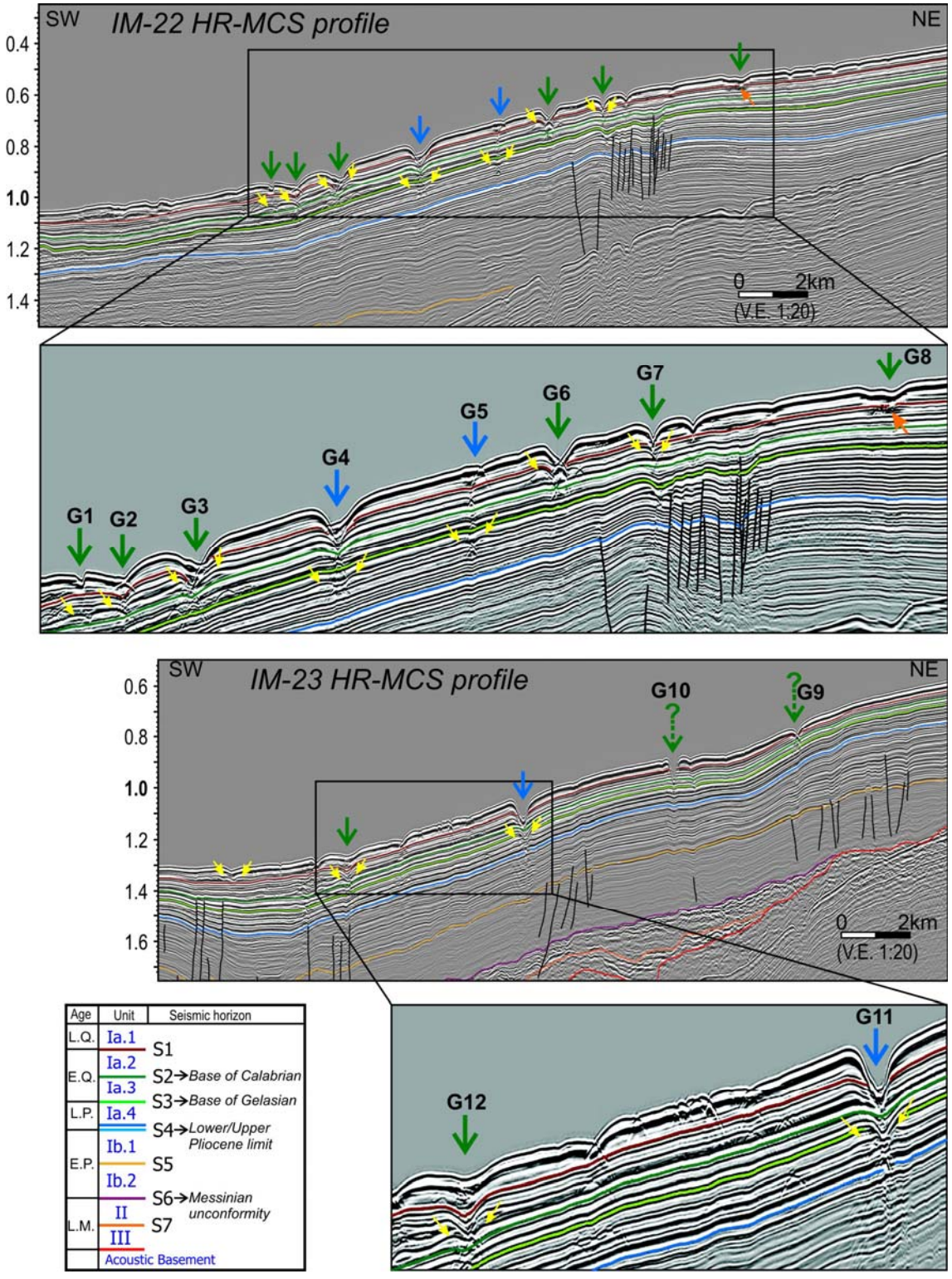

Figure 7.9. HR-MCS profiles IM-22 and IM-23 across the gullies and parallel to the CFZ. See Fig. 7.8b for location. Yellow arrows indicate channel levees features giving a minimum age for the gullies. The orange arrow indicates a chaotic facies interpreted to be a gully filled deposit. Thick green arrows indicate the gullies attributed to the start of the Calabrian age (S2 seismic horizon). Thick blue arrows indicate the gullies ascribed to the Upper Pliocene (above the S4 seismic horizon).

7.3. Discussion

7.3.1. Strike-slip rate analysis from geomorphological offset evidence

The first two generations of gullies are depicted in the bathymetric map of figure 7.8b by a blue line (first generation) and a green line (second generation). Gullies G8, G9 and G10, probably belonging to the second generation, are represented by dashed green lines. The third generation is not drawn in this map but can be observed as smooth incisions in the seafloor. The reconstruction in Fig. 7.10a demonstrates that the gullies from the second generation located at the NW block of the CFZ can be linked with a second or first generation gullies from the SE block, in accordance with a constant left-lateral 2.3-2.5 km offset (Fig. 7.8b). This constant value between piercing points suggests that it is attributed to a fault offset rather than a morphological deflection. The approximate 2.4 km offset together with the age of the second generation gullies suggest a minimum long-term strike-slip rate for the CFZ of 1.3 mm/yr for the last 1.8 Ma.

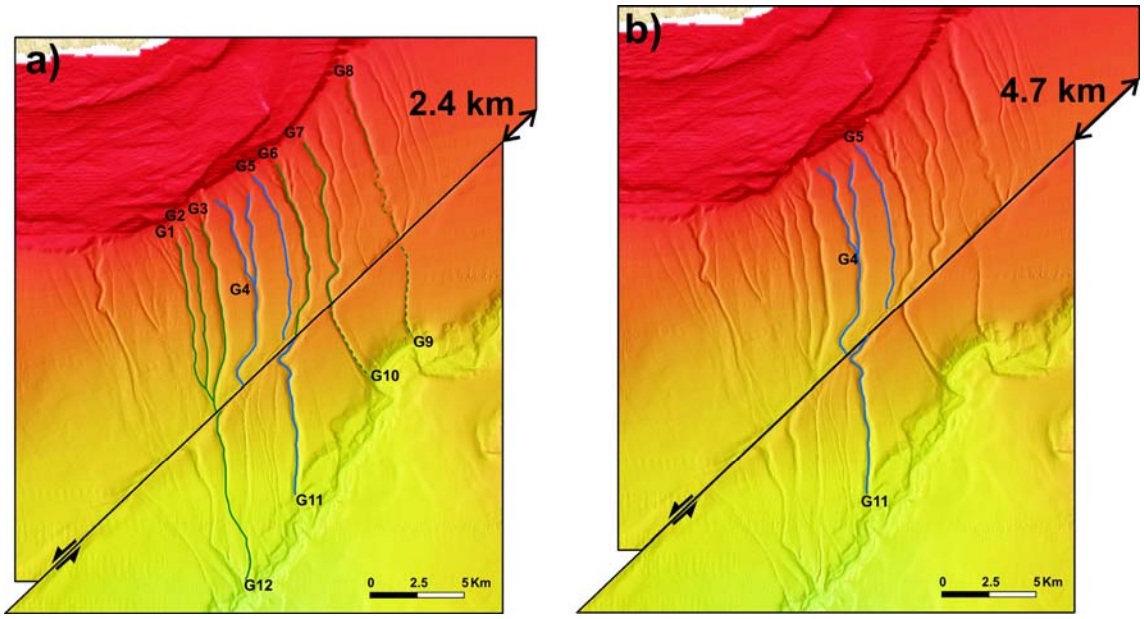

Figure 7.10. a) Reconstruction of the gullies during the Early Quaternary according to the offset of the second generation of gullies (<1.8 Ma old). b) Reconstruction of the gullies during the Late Pliocene according to the offset of the first generation of gullies (3.6-2.6 Ma old).

Figure 7.10a shows the situation of the gullies during the Early Quaternary, soon after 1.8 Ma BP, when the second generation of gullies, together with those of the first generation, were active. In this <1.8 Ma situation, the only gully that does not match with a correlative from the SE block is G4, which was interpreted as a first generation gully (2.6-3.6 Ma). A fault offset of 4.7 km is required to link this gully with the only contemporary gully of the SE block (Fig. 7.10b). Two gullies from the first generation

(G4 and G5) are found in the NW block, and only one (G11) in the SE block, which suggests that these gullies probably converged on the fault zone during their early stages of activity. In line with this hypothesis, the CFZ is interpreted to have been elevated, deflecting the drainage towards the SW. As a result the 4.7 km offset can be considered as a minimum offset. From this minimum offset and the age attributed to the first gully generation (2.6-3.6 Ma), a minimum long-term strike-slip of 1.3 mm/yr is inferred for this segment of the CFZ.

7.3.2. Dip-slip rate analysis from seismostratigraphic offset evidence

The Quaternary tectonic activity of the CFZ was demonstrated on the basis of vertically offset reflectors identified on the HR-MCS and TOPAS profiles (Figs. 6.11-6.15 and 6.17-6.20). By taking into account the age of the seismic horizons we estimated the dip-slip rates along the CFZ. Examples along each segment (i.e. North Carboneras Fault (NCF) and South Carboneras Fault (SCF)) (Fig. 7.11) are presented here from north to south.

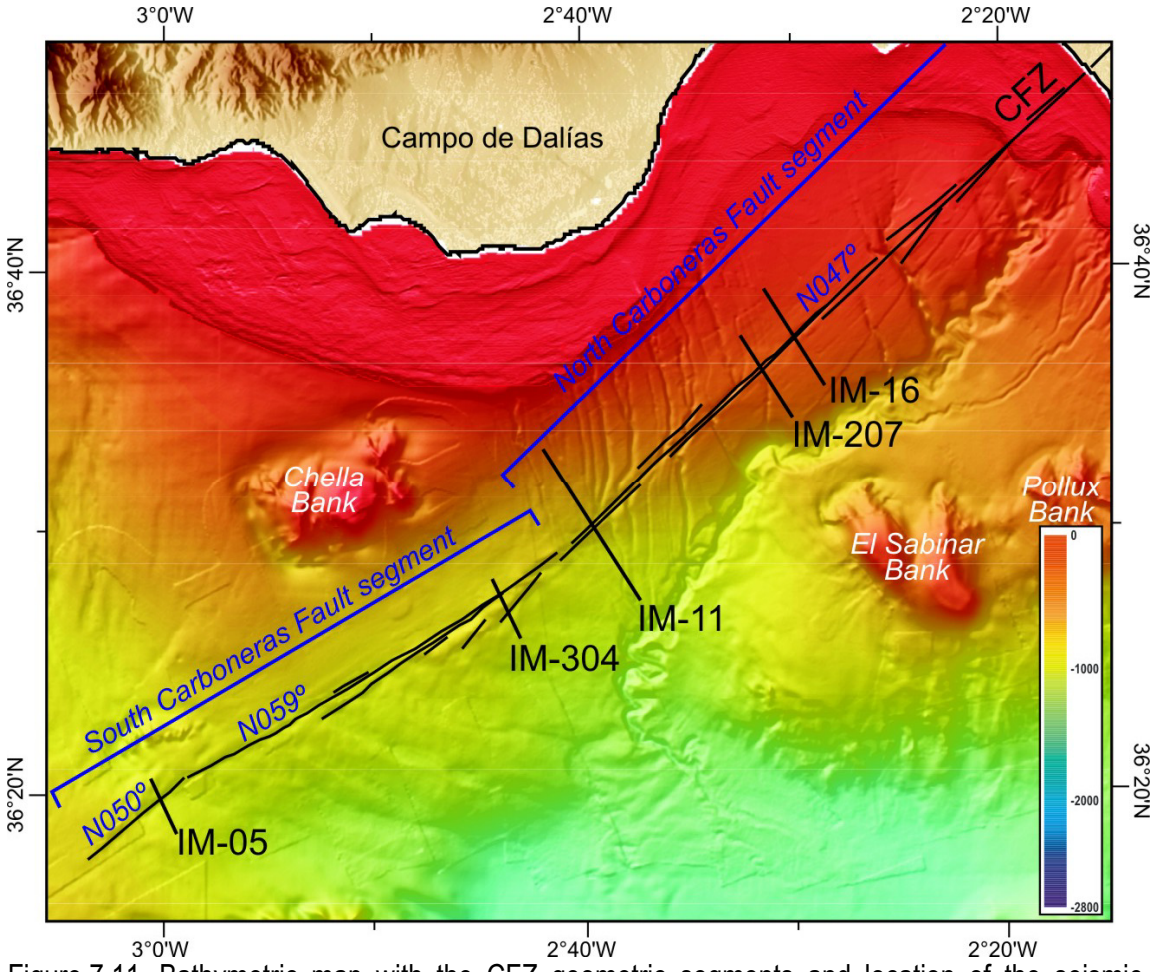

Figure 7.11. Bathymetric map with the CFZ geometric segments and location of the seismic profiles shown in figures 7.12-7.16.

However, before estimating dip-slip rates offshore, the following sources of uncertainty need to be taken into account:

1) Vertical offsets are calculated in time (TWTT s) and then transformed into depth (m) by assuming a propagation velocity of seismic waves through lithological units. For the HR-MCS profiles, an average velocity of 1800 m/s was used on the basis of the velocity analysis from commercial seismic surveys for the Plio-Quaternary units. For the TOPAS profiles, a velocity of 1600 m/s was used for the upper Quaternary units.

2) The ages of the horizons are estimated ages. In the HR-MCS profiles, the ages of the seismic horizons are estimated from few wells and local erosive processes cannot be ruled out. Thus, the real age of the HR-MCS horizon may vary locally. Ages of the TOPAS horizons were estimated by extrapolation of sediment core ages and correlation with MIS. Its inherent error cannot be quantified.

3) According to underwater sedimentation, Quaternary hemipelagites may drape the pre-existing relief mimicking the original topography of submarine features (i.e. landslides and faults scarps), and thus part of the vertical offset observed in the TOPAS profiles could be ascribed to this kind of sedimentation and not to fault movement. Thus, dip-slip observed in TOPAS profiles are considered as maximum values.

Besides these uncertainties, dip-slip rates were calculated along the submarine CFZ because they gave an idea of the distribution of the fault activity rather than a "real" fault velocity. Thus, the results obtained from these analyses are orientative results which have an associated error.

In the NCF segment, the IM-16 HR-MCS profile shows a 400 m narrow vertical fault zone (Fig. 7.12) that turns into a 200 m fault zone in the uppermost sediments as observed in the TOPAS profile. Plio-Quaternary seismic horizons on each side of the fault are extrapolated to the fault zone and the offset is calculated: 174 m for the S4 horizon, 119 m for the S3 horizon and 92 m for the S2 horizon. Taking into account the estimated age of each seismic horizon, S4 is 3.6 Ma BP, S3 is 2.6 Ma BP and S2 is 1.8 Ma BP, the long-term dip-slip rate is calculated. The measured offset of the three Plio-Quaternary horizons (S2, S3 and S4) suggests a 0.05 mm/yr dip-slip rate, which apparently remained constant along this period. In addition, using the TOPAS data, the boundary between unit I and unit II units (130 ka) shows a 17.7 m vertical offset, suggesting a 0.14 mm/yr maximum dip-slip rate.

Located 3.3 km to the SW, the TOPAS profile IM-207 (Fig. 7.11) shows a succession of four mass transport deposits (i.e. landslides) (L1, L2, L3 and L4 in Fig. 7.13) faulted by two active fault traces of the CFZ. The vertical offsets observed on each fault trace were added up to a total vertical offset assuming that these fault traces converge at depth to a single seismic structure. The total vertical offset yields a 6 m for the younger L1 landslide, 10.7 m for the L2 landslide and 19.9 m for the L3 landslide.

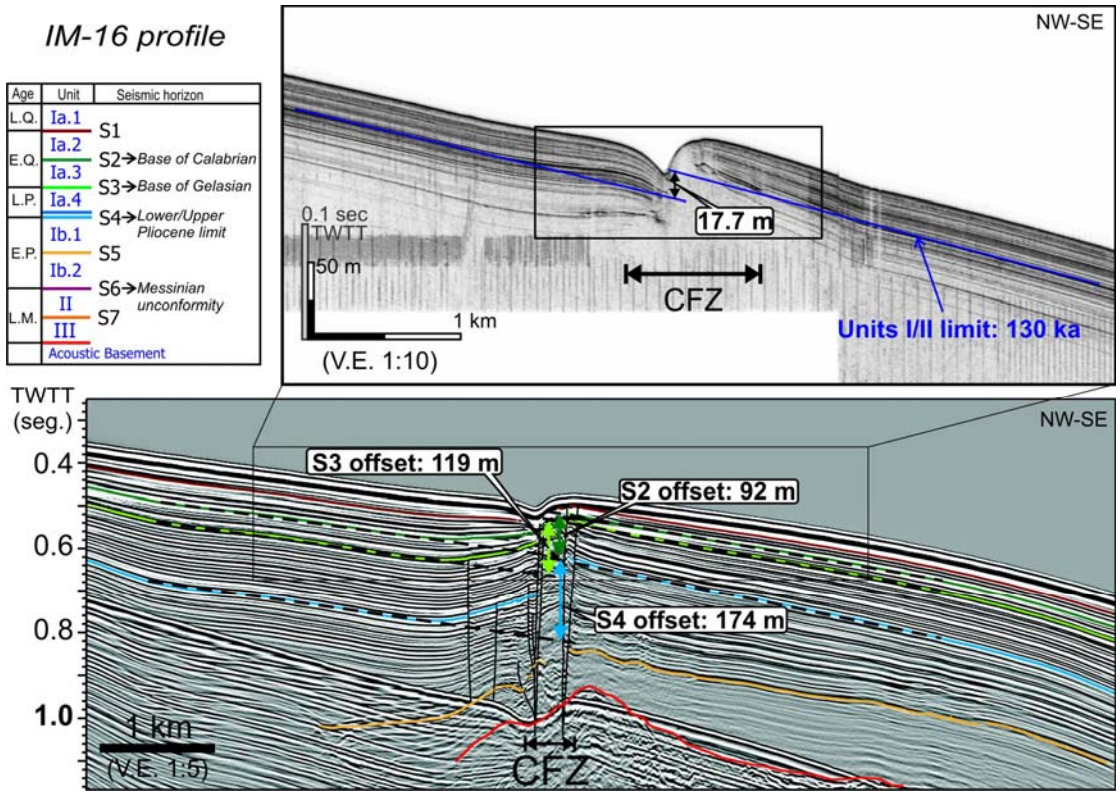

Figure 7.12. TOPAS (above) and HR-MCS (below) profiles IM-16 across the NCF segment with vertical offset of seismic horizons. The offsets were calculated assuming a mean 1800 m/s velocity for the Plio-Quaternary units in the HR-MCS profile, and 1600 m/s velocity for the upper sedimentary layers in the TOPAS profile. These profiles are located in figure 7.11 and extended in figures 6.11 and 6.14.

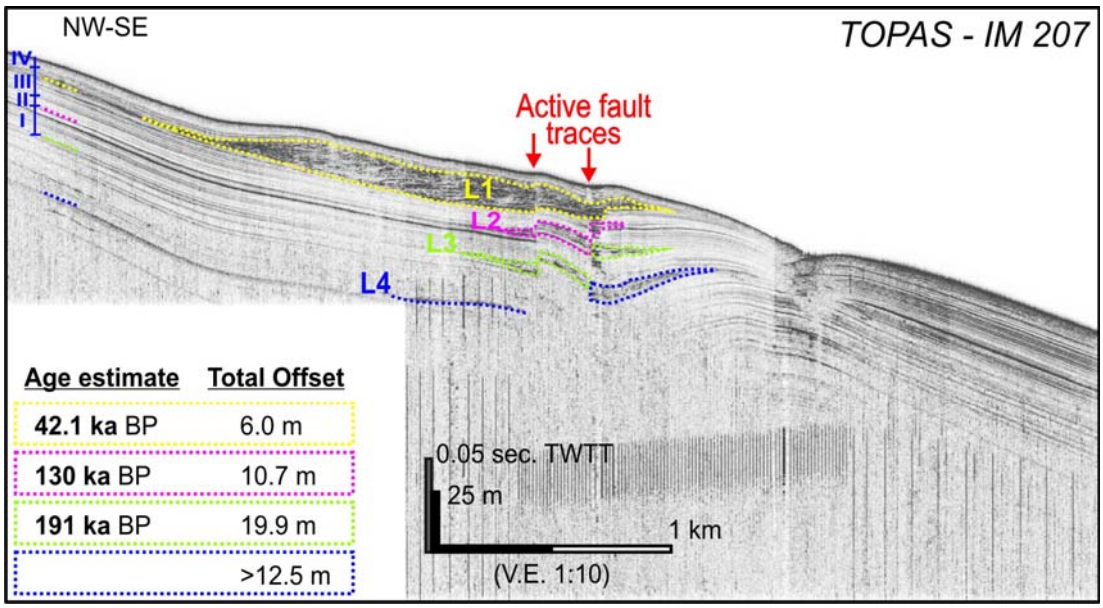

Figure 7.13. TOPAS profile IM-207 across the NCF segment showing a succession of four faulted landslides. The vertical offsets were calculated assuming a 1600 m/s velocity for the upper sedimentary layers. Location in figure 7.11. V.E. Vertical exaggeration.

The oldest L4 landslide is observed on each side of the fault zone but not between the fault traces owing to a decrease in the resolution of the system. Thus, the total offset cannot be calculated, and a minimum 12.5 m of vertical offset was inferred. Landslide L3 is located at the base of unit I, and its estimated age is 191 ka. The base of the L2 landslide is located at the boundary between units I/II and its estimated age is 130 ka.The L1 landslide is located inside unit III and its age is assumed to be 42.1 ka according to average sedimentation rates in this unit (Fig. 7.13). According to these data, dip-slip rates are calculated: 0.14 mm/yr for the L1 landslide, 0.08 mm/yr for the L2 landslide and 0.10 mm/yr for the L3 landslide. A mean 0.1 mm/yr dip-slip rate has been inferred from these results since the Late Pleistocene.

In the southern part of the NCF segment (Fig. 7.11), the HR-MCS profile IM-11 (Fig. 7.14) shows a 500 m wide fault zone vertically displacing the Quaternary reflectors. A total vertical offset of 102 m is calculated for the S4 horizon, 34 m for the S3 horizon, and 25 m for the S2 horizon, which suggests a dip-slip rate of 0.03 mm/yr for the last 3.6 Ma and 0.01 mm/yr for the last 1.8-2.6 Ma. Seismic reflectors are faulted up to the Late Quaternary, as observed in the IM-11 TOPAS profile (Fig. 7.14). In this profile, the vertical offset for each fault trace was added, assuming that these fault traces converge at depth to a single seismic structure. The total offset for the base of the unit III is 14 m, suggesting a 0.19 mm/yr dip-slip rate since 71 ka BP, which is the estimated age of the boundary between units III/II. The boundary between units IV/III may also be displaced although the vertical resolution is too close to the offset for each fault trace, and therefore was not been used.

Another example comes from the northern part of the N059º SCF segment (SCF-4 sub-segment) characterized by a pressure ridge formed within the fault zones (Fig. 7.11) and controlling a sag pond feature to the NW (profile IM-304 in Fig. 7.15). In a zoom detail, two vertical fault traces can be distinguished in the active fault zone at the NW boundary of the sag-pond. The boundaries of the TOPAS seismic units are well recognized. A 9.5 m vertical offset for the base of unit II and a 7.8 m offset for the base of unit III were calculated. According to the estimated ages for these units, maximum dip-slip rates of 0.07 mm/yr since 130 ka BP (the age of the boundary between I/II units) and 0.11 mm/yr since 71 ka BP (the age of the boundary between III/II units) are inferred.

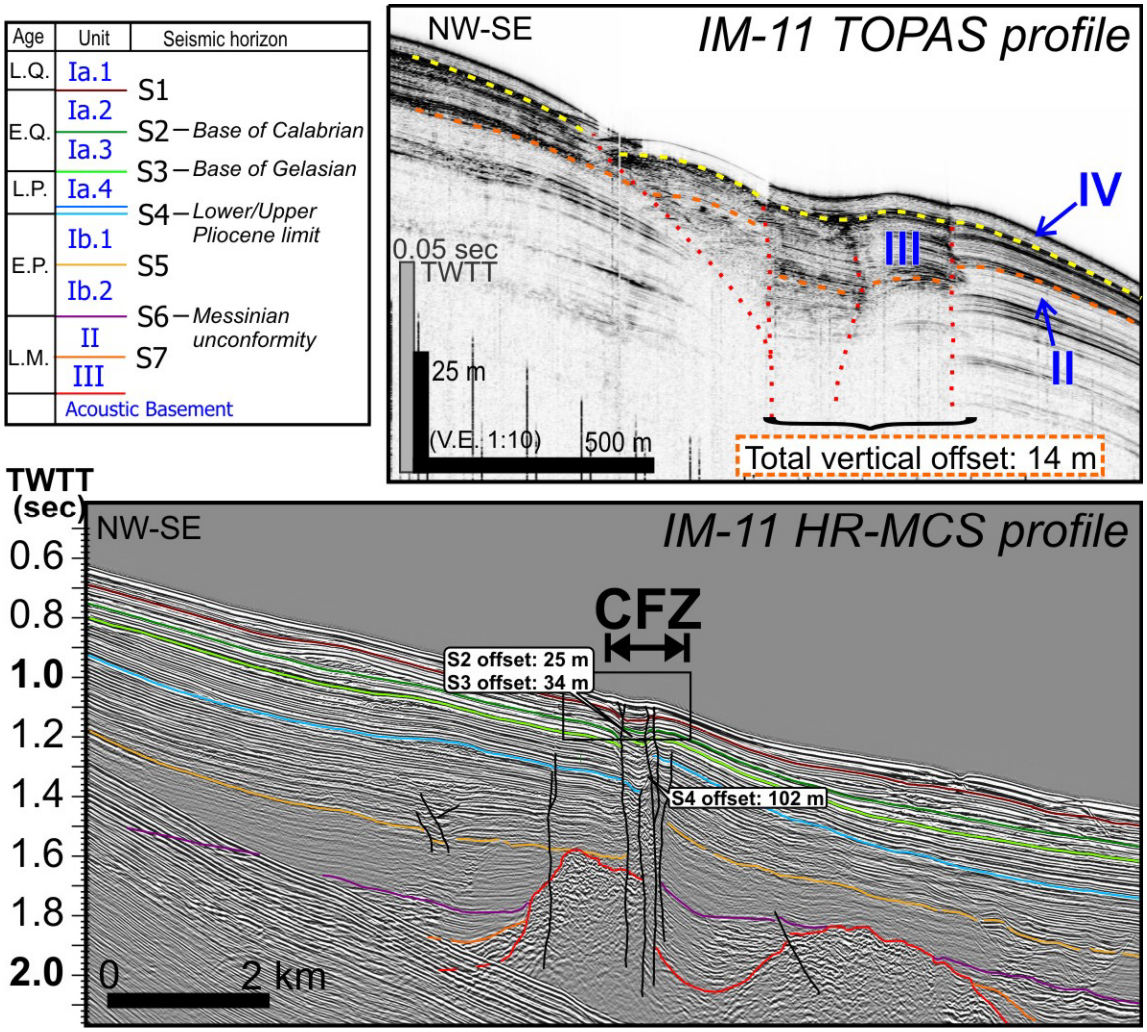

Figure 7.14. TOPAS (above) and HR-MCS (below) profiles IM-11 across the NCF segment and vertical offset of seismic horizons. The offsets were calculated assuming a mean 1800 m/s velocity for the Plio-Quaternary units in the HR-MCS profile, and a 1600 m/s velocity for the uppermost layers in the TOPAS profile. These profiles are located in figure 7.11 and extended in figures 6.12 and 6.15.

In the southern part of the SCF segment (SCF-6 sub-segment), the orientation of the fault trace changes to N050º (Fig. 7.11). On surface, the vertical offset is observed as a 45 m high scarp. At depth, the HR-MCS profile IM-05 (Fig. 7.16) shows a 153 m offset for horizon S4, a 86 m offset for horizon S3 and a 71 m offset for horizon S2. According to the ages given to these horizons, the dip-slip rates obtained are 0.04 mm/yr for the last 3.6 Ma, 0.03 mm/yr for the last 2.6 Ma and 0.04 mm/yr for the last 1.8 Ma. Taking into account the uppermost sedimentary units as observed in the TOPAS profile IM-05 (Fig. 7.16), the base of unit II has a 42 m vertical offset, suggesting a maximum dip-slip rate of 0.3 mm/yr since 130 ka BP.

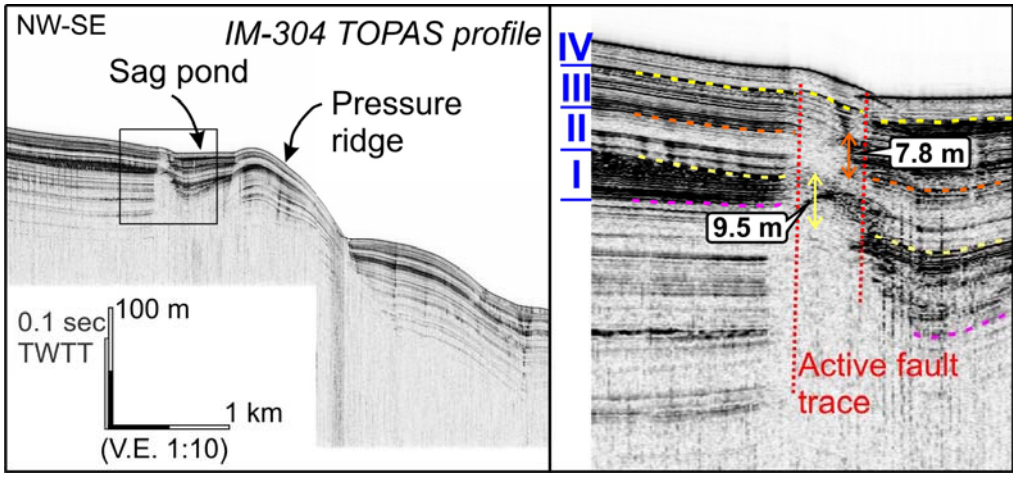

Figure 7.15. TOPAS profile IM-304 and zoom across the SCF segment showing a pressure ridge and a sag-pond in the fault zone. The vertical offsets for the active fault traces were calculated assuming a 1600 m/s velocity for the uppermost sedimentary layers. V.E. Vertical exaggeration. This profile is located in figure 7.11 and extended in figure 6.17.

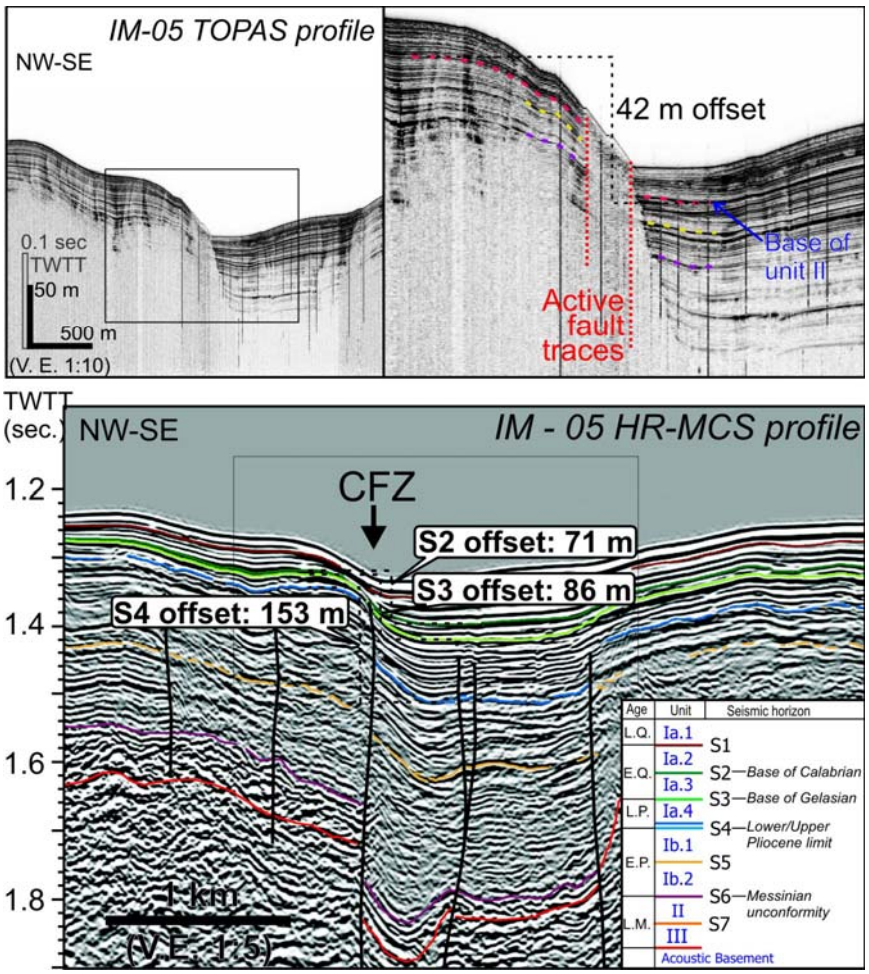

Figure 7.16. TOPAS (above) and HR-MCS (below) profile IM-05 across the N050º SCF segment and horizons vertically offset. The offsets were calculated assuming a mean 1800 m/s velocity for the Plio-Quaternary sedimentary units in the HR-MCS profile, and a 1600 m/s velocity for the uppermost layers in the TOPAS profile. V.E. Vertical Exaggeration. These profiles are located in figure 7.11 and extended in figures 6.17 and 6.20.

Table 7.4 shows a summary of the dip-slip rates obtained for the HR-MCS and TOPAS profiles analysed along the CFZ. The long-term dip-slip rates calculated from the horizons S2, S3 and S4 vary between 0.01 mm/yr and 0.05 mm/yr, whereas the short-term maximum dip-slip rates calculated from the Late Pleistocene TOPAS reflectors range from 0.1 mm/yr to 0.3 mm/yr. This variability may be associated with the uncertainties discussed at the beginning of this section. In addition, the higher values obtained from the Late Pleistocene faulted units are in agreement with the concept that hemipelagic sediments may drape the uppermost layers, and thus the resulting rates should be considered as maximum values.

Table 7.4: Summary of the dip-slip results obtained along the offshore NCF and SCF segments. The long-term dip-slip rates are calculated from vertical offsets of HR-MCS horizons (S2, S3 and S4), and the short-term dip-slip rates are calculated from the vertical offsets of Late Pleistocene TOPAS reflectors.

Offshore Fault segment	**Profile #**	**Long-term dip-slip rates (mm/yr) since Late Pliocene (HR-MCS seismics)**			**Max. short-term dip-slip rates (mm/yr) since Late Pleistocene (TOPAS profiles)**
		Horizon S4	**Horizon S3**	**Horizon S2**	
North Carboneras Fault segment	IM-16	0.05	0.05	0.05	0.14
	IM-207				0.10
	IM-11	0.01	0.01	0.03	0.19
South Carboneras Fault segment	IM-304				0.11
	IM-05	0.04	0.03	0.04	0.3

Slip rate discrepancies can also be attributed to the conceptual significance of estimating dip-slip rates in a dominantly strike-slip fault. When the dip-slip component is relatively low, the pre-existing topography may considerably affect the apparent vertical offset. Offshore, the topography is in general smoother than onshore because erosion rates are lower and there is a continuous vertical flux of sediments covering the seafloor. In addition, a pure lateral displacement of a flat dipping surface involves an apparent vertical displacement. In the case of a south-dipping surface (i.e. the slope of the Almería Margin) and a left-lateral displacement along a NE-SW trending fault (i.e. the CFZ), the NW block would "apparently" be uplifted with respect to the SE block. However, the situation of CFZ is more complex since the fault has a vertical component and there is a block rotation behaviour of the NE block ("scissor-like"), as suggested in Chapter 6. The block rotation model implies an along fault variation in the apparent dip-slip component depending on which point of the rotating block the analysis is considered. From this point of view, further systematic analyses of the dip-slip rates variations along the CFZ may provide evidence of the boundaries of the rotating blocks.

Despite the large uncertainties of the dip-slip rate calculations, the values are one to two orders of magnitude lower than the strike-slip rates calculated from the left-laterally offset gullies in accordance with the prominent strike-slip nature of the CFZ.

7.3.3. Does the turbidite paleoseismology concept work in the CFZ? Implications for recurrence intervals

Turbidite paleoseismology is based on the correlation between synchronous turbidites simultaneously triggered by an earthquake (e.g. Goldfinger et al., 2003). The criterion for synchronicity, as defined by Adams (1990) and Goldfinger et al. (2003; 2007) in the Cascadia Margin, is based on the "confluence channel test", i.e. the same number of turbidite events should be found upstream and downstream from the confluences between tributaries, slope channels and deep-sea channels. Coeval turbidites are then correlated with instrumental and historical earthquake records, such as land paleoseismic data and tsunami deposits, if available (e.g. Garcia-Orellana et al., 2006; Gràcia et al., 2010). In some areas, such as the Gulf of Cadiz, the synchronicity test is based on the existence of coeval deposits located in widely separated depositional areas (slope basins and abyssal plains) since the particular physiography of this margin is unsuitable for applying the channel confluence test as first defined. Turbidite paleoseismology was successfully tested in the low-convergence SW Iberia margin. A total of 7 widely distributed turbidites deposited in the Holocene (during which the sea level was relatively stable) have been identified and correlated with past seismic and tsunami events. Thus, a regional recurrence interval of great magnitude earthquakes (Mw > 8.0) of 1800 years has been obtained (Gràcia et al., 2010).

In the case of the Alboran Sea, a study devoted to turbidite paleoseismology was not carried out. However, a recent sedimentological study based on 7 cores located in the area of the Almería Canyon (Bozzano et al., 2009) can be re-interpreted in the light of turbidite paleoseismology. These authors correlated 5 turbidites identified in the cores and ascribed some of these turbidite events to sea level variations (T2, T4 and T5 in Fig. 7.17). They also identified a Holocene turbidite (T1) deposit (< 1.3 Cal ka BP). Taking into account the historical seismicity of the region, they considered an earthquake as a possible triggering mechanism for the T1 event. This recent turbidite event suggests that the last earthquake occurred soon after 1.3 ka BP which, surprisingly, is consistent with the results obtained onshore (section 5.2.8). Downcore, Bozzano et al. (2009) describe a lower turbidite (T3) younger than 14.9 Cal ka BP of uncertain origin. Assuming that this turbidite had also a seismic origin, the time elapsed between turbidites T1 and T3 would be about 13 ka, which coincides with the recurrence period obtained onshore at the El Hacho Site (section 5.2.8). Nevertheless, this hypothesis is not supported by solid evidence as the seismic origin of the turbidites is uncertain. A more an extensive analysis is required.

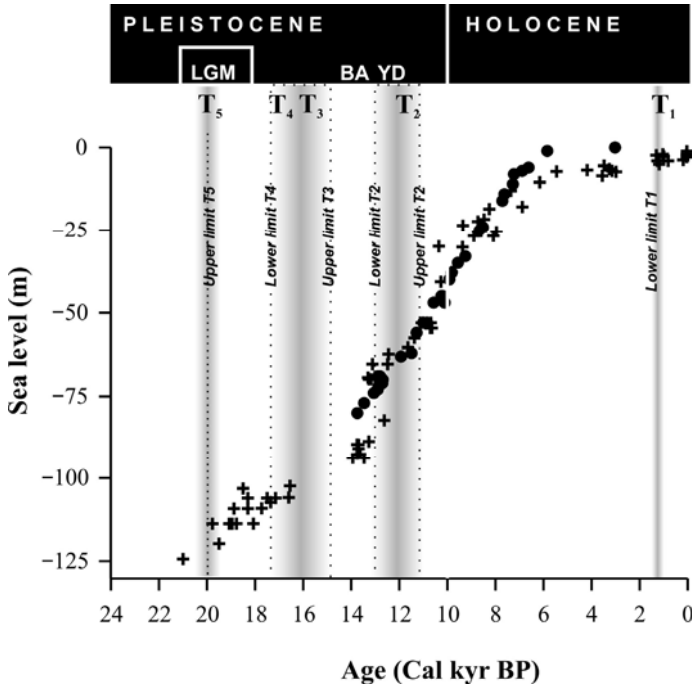

Figure 7.17. Postglacial sea-level position (Fairbanks, 1990; Bard et al., 1990) and turbidite emplacement in the Almeria Channel overbank area. T1–T5 labels refer to the nomenclature given to the turbidite layers. Shaded bands show uncertainties of the turbidite age assignment. At the top panel, LGM: Last Glacial Maximum; BA: Bølling-Allerød climate event; YD: Younger Dryas climate event (Bozzano et al., 2009).

7.4. Conclusions

The analysis of marine sediment dating allowed us to establish a relationship between the alternation of well-stratified and transparent TOPAS facies and the Marine Isotopic Stages (MIS). Well-stratified unit I is estimated to have been deposited during the cold MIS 6, its base being at 191 ka BP. Semi-transparent unit II is estimated to have been deposited during the warm MIS 5, its base being at 130 ka BP. Well-stratified unit III is estimated to have been deposited during cold stages MIS 2-4, its base being at 71 ka BP. The base of the uppermost unit IV was dated by ^{14}C as 31.1 Cal ka BP.

According to the sedimentary features observed in the HR-MCS profiles, three generations of gullies were identified in the Dalías Tributary Valley System (DTVS). The first generation started during the Late Pliocene (3.6-2.6 Ma), the second generation soon after the Calabrian stage (<1.8 Ma) and the third generation during the Late Quaternary.

The deflected gullies of the DTVS across the Northern Carboneras Fault segment show a 2.4 km left-lateral offset since the Early Quaternary (<1.8 Ma) suggesting a minimum strike-slip rate of 1.3 mm/yr since this period. A minimum offset of 4.7 km has also been inferred since the Late Pliocene (3.6-2.6 Ma), yielding a minimum strike-slip rate of 1.3 mm/yr since this period.

Vertically offset seismic reflectors from HR-MCS and TOPAS profiles show offsets that, together with the dating analysis, enabled us to calculate a 0.01-0.05 mm/yr minimum dip-slip rate since the Late Pliocene and a maximum dip-slip rate of 0.1-0.3 mm/yr since the Late Pleistocene. Despite the fact that the estimation of dip-slip rates along a dominantly strike-slip fault entails many inherent errors, the results obtained suggest that the vertical component of the CFZ is one to two orders of magnitude lower than the strike-slip rate calculated from the offset gullies in agreement with the prominent strike-slip nature of the CFZ.

A thorough turbidite paleoseismology analysis has not been carried out in the Alboran Sea. However, a first approach was made using the sedimentological results and turbidite ages obtained from a published study of the Almería Turbidite system (Bozzano et al., 2009). Although the conclusions are very speculative, in the absence of evidence that earthquakes are the triggering mechanisms of these turbidites, a maximum elapsed time since the last turbidite of 1.3 ka and a maximum interval between the two possible seismic turbidites of about 13 ka were obtained. These results are surprisingly coincident with the minimum elapsed time since the last earthquake and the mean recurrence period values found onshore.